GAS-CHARGED SEDIMENTS:

PHENOMENA AND CHARACTERIZATION

A Thesis
Presented to
The Academic Faculty

by

Junbong Jang

In Partial Fulfillment
of the Requirements for the Degree
Doctor of Philosophy in the
School of Civil and Environmental Engineering

Georgia Institute of Technology
December 2014

GAS-CHARGED SEDIMENTS:

PHENOMENA AND CHARACTERIZATION

Approved by:

Dr. J. Carlos Santamarina, Advisor
School of Civil and Environmental Engineering
Georgia Institute of Technology

Dr. Susan E. Burns
School of Civil and Environmental Engineering
Georgia Institute of Technology

Dr. J. David Frost
School of Civil and Environmental Engineering
Georgia Institute of Technology

Dr. Christian Huber
School of Earth and Atmospheric Science
Georgia Institute of Technology

Dr. William F. Waite
Woods Hole Science Center
U.S. Geological Survey

Date Approved: June 26, 2014

To my family

ACKNOWLEDGEMENTS

This thesis has been a collaboration that includes not only my effort but also the contributions of others. First of all, I cannot begin to express my sincere thanks to my advisor, Dr. J. Carlos Santamarina. His passion and knowledge have been the inspiration for the completion of my doctorate, and they will continue to drive me to achieve future dream.

I am also grateful to my thesis committee, Dr. Susan E. Burns, Dr. J. David Frost, and Dr. Christian Huber, for their valuable comments about my research. Special thanks to Dr. William Waite for his collaboration and insightful discussion on my research. I would like to acknowledge the faculty in the Geosystems group for sharing their experience.

I acknowledge funding from the Gas Hydrate Joint Industry Project (Chevron and the U.S. Department of Energy) and the Goizueta Foundation.

I would like to thank the members of the Particulate Media Laboratory for their help: Hosung Shin, Jongwon Jung, Jaewon Jang, Nicolas Espinoza, Seunghee Kim, Minsu Cha, Cesar Pasten, Songhun Chong, Shahrzad Roshankhah, Aswathy Sivaram, Liang Lei, Seth Mallett, Junghee Park, Zhonghao Sun, Qi Liu, Adrian Garcia, Xingwei Ren, Alessio Savioli, Stefanos Athanoasopoulos, Eunseok Bang, Changho Lee, Norimasa Yoshimoto, Cuiying Lu, Lucio Cruz, and Andrea Mezencevova. Special thanks to Sheng Dai, Marco Terzariol, and Efthymios Papadopoulos for the wonderful experience I was fortunate to have in Japan. I would like to recognize help from Aditya Bhatt, Fengshou Zhang, Bate Bate, Joan Larrahondo, and colleagues in the Geosystems group. Also, many thanks to Jane Chisholm for corrections in my writing.

I wish to thank Sihyun Kim, Taeseo Ku, Hyunwook Choo, Seokho Jeong, Jongmuk Won, Jonghee Kim, Hyunjoo Jung, Seungdae Oh, Eunhyea Chung, Manwoo Park, Seungho Hong, Dongha Kim, Sujin Kim, Sehoon Lee, Sunghu Kim, Eunjung Cha, Gun Kim, Jongseok Moon, Jaewook Yoo, Seungyeon Lee, and the Korean fellows in the School of Civil and Environmental Engineering for their kind help and encouragement.

Finally, I would like to express my deepest appreciation to my parents, my brother, and my sister for their priceless love and support. Thanks to my family, I have been able to pursue and succeed in my doctoral study.

TABLE OF CONTENTS

LIST OF TABLES

LIST OF FIGURES

SUMMARY

The mass of carbon trapped in methane hydrates exceeds that in conventional fossil fuel reservoirs. While methane in coarse-grained hydrate-bearing sediments is technically recoverable, most methane hydrates are found in fine-grained marine sediments where gas recovery is inherently impeded by very low gas permeability. Using experimental methods and analyses, this thesis advances the understanding of fine-grained sediments in view of gas production from methane hydrates. The research scope includes: a new approach for the classification of fines in terms of electrical sensitivity, the estimation of the sediment volume contraction during hydrate dissociation, a pore-scale study of gas migration in sediments and the self-regulation effect of surfactants, the formation of preferential gas migration pathways at interfaces during gas production, pressure core technology for the characterization of hydrate bearing sediments without causing hydrate dissociation, and the deployment of a bio-sub-sampling chamber in Japan.

CHAPTER 1

INTRODUCTION

1.1 Gas Recovery from Hydrate-Bearing Sediments

The amount of methane in hydrate-bearing sediments overwhelms that of all conventional gas reservoirs combined. If robust recovery processes were to be developed, methane from hydrate-bearing sediments would be an alternative resource to replace gas from conventional hydrocarbon reservoirs [Kvenvolden, 1993; Milkov, 2004; Sloan and Koh, 2008; Boswell and Collett, 2011].

Current methods for gas recovery from conventional hydrocarbon reservoirs are not suitable for gas recovery from hydrate-bearing sediments because gas is trapped in crystals. Instead, gas recovery from hydrate-bearing sediments can involve depressurization, heating, inhibitor injection, or CH_4-CO_2 exchange [Holder et al., 1984; Sloan and Koh, 2008].

Gas production field tests have been conducted at gas hydrate sandy sites in Mallik in Canada [Kurihara et al., 2010], Mount Elbert in the United States [Moridis et al., 2011], and the Nankai Trough in Japan [Yamamoto, 2013]. These tests showed the technical feasibility of gas recovery from coarse-grained sediments albeit at a high cost [Collett, 2002; Boswell and Collett, 2011].

On the other hand, gas recovery from fine-grained hydrate-bearing sediments is not yet technically feasible. [Boswell and Collett, 2011].

1.2. Thesis Organization

This thesis investigates the physical properties of fine-grained hydrate-bearing sediments and the physical phenomena involved in gas production.

Chapter 2 provides a general description of fines. In geotechnical engineering, fines are classified using Casagrande's plasticity chart. However, the chart does not properly characterize fines for hydrate-bearing sediment studies. The characteristics of clays and silts are reviewed, experiments are conducted to clarify their fundamental behavior, and new boundaries between clays and silts are proposed.

Chapter 3 analyzes volume change in hydrate-bearing sandy and silty sediments during gas production. Based on analogical experiments, empirical methods are suggested to evaluate the potential vertical strains that can develop in sediments during hydrate dissociation.

Chapter 4 explores capillarity during hydrate dissociation in sediments. Pore-scale experimental and analytical studies place emphasis on surfactant concentrations and injection flow rates.

Chapter 5 proposes a possible mechanism for gas recovery from fine-grained hydrate-bearing sediments whereby gas-driven fractures facilitate gas production. Analogical experiments provide insight into possible gas migration ways during gas production.

Chapter 6 documents the development of pressure core characterization tools PCCTs used to obtain sediment properties without causing hydrate dissociation. The work

reported in this chapter is the result of a collaboration among the author, Sheng Dai, and Marco Terzariol.

Chapter 7 reports the deployment of PCCTs to characterize pressure cores from the Nankai Trough in Japan. The chapter focuses on biological studies conducted using the bio-subsampling chamber.

Finally, Chapter 8 summarizes salient conclusions from this study.

CHAPTER 2

FINES AND FINE-GRAINED SEDIMENTS

2.1 Introduction

Gas hydrates can be found when temperature and pressure meet hydrate stability conditions, as in the deep seafloor sediments and beneath the permafrost [Kvenvolden, 1988; Sloan and Koh, 2008]. Most hydrate-bearing sediments are found in fine-grained sediments. Therefore, the understanding of fines is important for hydrate production. Fines clog pore throats in coarse sediments during gas production [Kampel et al., 2008; Valdes and Santamarina, 2008; Jung et al., 2012], and high capillarity by fines leads to lens or nodule hydrate topology [Clennell et al., 1999; Dai et al., 2012].

Fine grains are smaller than 75 μm. Fine-grained soils are classified using the plasticity chart [Casagrande, 1948]. However, this chart fails to properly distinguish silts and clays, and its fundamental interpretation is not obvious [Casagrande, 1938; Casagrande, 1948].

This chapter aims to elucidate ambiguious definitions, to gain fundamental understanding of fine-grained soils, and to propose a new approach to enhance the classification of fine-grained sediments.

2.2 Silt or Clay? Previous Studies

Soil classification systems in the United States and other countries center on grain size distribution and Atterberg limits (Table 2.1). Yet, definitions of silt and clay remain unclear and even contradictory.

2.2.1 Index Tests

Simple identification tests for soils that pass sieve No. 40 (0.4mm) assess the soil dilatancy, dry strength, and toughness [Casagrande, 1948; Holtz and Kovacs, 1981; ASTM-D2488, 2009]. In general, the plasticity of clays is pore-fluid chemistry dependent (pH and ionic concentrations [Santamarina et al., 2002; Palomino and Santamarina, 2005]). On the other hand, silts dilate when squeezed or shaken at low confining stress, exhibit low dry strength after air or oven drying, and fail to form 3 mm diameter rolls but crumble instead. These methods are simple but ill-defined. Moreover, the interpretation of test results is often subjective and adds further confusion to the distinction between silts and clays.

2.2.2 Various Definitions of Clays and Clay Minerals

The term, clay, is interchangeably used to refer to:

- Particle size less than 2 μm which corresponds to approximately 1 m^2/g specific surface. Particles of this size show Brownian movement in water [Atterberg, 1912 from Baver et al., 1972].

- Particles that experience electrical interactions in aqueous suspensions as a function of pore fluid pH, ionic concentration, and permittivity.
- Pastes that harden during firing and gain strength (e.g., china dishes)
- Minerals made of phyllosilicates such as kaolinite and smectite group. Yet not all phyllosilicates are clay minerals (e.g., mica) [Nesse, 2000; Mitchell and Soga, 2005].

2.2.3 Soil Classification – Atterberg Limits

Soil classification methods are compared in Table 2.1 to highlight: (a) the relevance of fines and (b) the use of liquid limit to assess overall plasticity, as noted by Casagrande (1938). Because of uncertainty in the standard method used for the liquid limit, the Casagrande cup [Wintermayer, 1926; Casagrande, 1958; Sherwood and Ryley, 1970], the fall cone test was proposed as alternative standard method, whereby the liquid limit is the water content at which the undrained shear strength of the soil paste is nearly 2.66 kPa [Hansbo, 1957; BS1377, 1990; Koumoto and Houlsby, 2001]. The liquid limit is strongly correlated to the specific surface area [Warkentin, 1972; Wetzel, 1990; Cerato and Lutenegger, 2002; Santamarina et al., 2002].

The USCS uses the plasticity index PI=LL–PL and the liquid limit LL to distinguish between clays and silts. In addition, this plasticity chart discerns silt-like materials with high liquid limits yet low plasticity such as diatoms from sediments with high liquid limit and high plasticity such as bentonite. However, the plasticity chart fails to provide consistent boundaries. For example, clay minerals often plot below the A-line (Figure 2.1);

furthermore, mixtures with non-plastic materials distort soil classification with this chart (Figure 2.2).

2.3 Experimental Study

The electrical sensitivity of soil particles is explored herein to develop a more robust classification of fine soils. The experimental study includes specific surface, liquid limit, sedimentation, and insertion tests conducted using different pore fluids to alter electrical interactions.

2.3.1 Materials

Tested soil samples selected for their unique characteristics included: bentonite, ground illite, kaolinite, silica flour, diatom, fly ash and Ottawa 20-30 sand. These dry soils were mixed with fluids of different polarity and ionic concentration which affect electrical interactions. The selected fluids are: deionized water, NaCl solution (1 M for sedimentation and insertion tests and 2 M for liquid limit tests), a sodium-hexametaphosphate $(NaPO_3)_6$ solution (0.065 mol/L) and kerosene. The properties of tested soils and fluids are summarized in Table 2.2.

2.3.2 Test Procedures

Specific Surface. The specific surface was measured using the methylene blue test because water separates particles that could otherwise remain face-to-face aggregated in dry tests [Santamarina et al., 2002]. The concentration of the methylene blue was 5 g/L.

The methylene blue solution was gradually added to the soil suspension until a drop from the suspension showed a halo on a P5 filter paper (details in Santamarina et al., 2002).

Liquid Limit. The fall cone test was used for this study. The 80 g 30-degree apex cone was allowed to penetrate the paste for 5 seconds. The liquid limit is the water content of the paste when penetration is 20 mm.

Sedimentation. Oven-dried specimens were mixed with the selected fluids, vacuumed, and stirred twice in 16 hours. Sedimentation tests were conducted in 200 mm tall acrylic cylinders 25.4 mm in diameter (details in Palomino and Santamarina, 2005).

Insertion Test. After sedimentation, the cylinder was tapped on a table to force densification of the sediment. 12 hours later, a 31 g, 3.2 mm diameter, 380 mm long stainless steel rod with a 12.7 mm diameter ball at its tip was slowly placed on the surface of the soil and released. The penetration depth was measured from the initial sediment surface.

Comment. The sedimentation test causes inherent segregation and its interpretation is less clear when sediments are heterogeneous. Segregation affects the insertion test conducted after sedimentation. Additional tests were conducted on silica flour and diatom without < 7 μm fines (separated by sedimentation).

2.3.3 Results

The liquid limit and specific surface data in Table 2.2b confirm that the liquid limit of a soil is proportional to its specific surface.

The ratios between the liquid limits determined with deionized water (LL_{DW}), NaCl solution (LL_{NaCl}), and kerosene ($LL_{kerosene}$) are analyzed to assess fluid effects on interparticle forces. First, values are corrected for salt precipitation and specific gravity:

$$\left.\frac{LL_{DW}}{LL_{NaCl}}\right|_{corrected} = \frac{LL_{DW}}{LL_{NaCl}}\left(1 - c_{NaCl} LL_{NaCl}\right) \quad [2.1]$$

$$\left.\frac{LL_{DW}}{LL_{kerosene}}\right|_{corrected} = \frac{LL_{DW}}{LL_{kerosene}} G_{s,kerosene} \quad [2.2]$$

where $G_{s,kerosene}$ is the specific gravity of kerosene, c_{NaCl} [g/g] the concentration of NaCl in water. Corrections reflect differences in water-kerosene unit weight and the precipitation of salts during oven-drying when the NaCl solution is used. These ratios are presented in Figure 2.3. Empty circles show the ratio as defined above and solid circles are its inverse when the ratio is less than 1.0. Ottawa 20-30 sand, fly ash, silica flour and diatom showed low or no sensitivity to pore fluids, but kaolinite and bentonite exhibited significant pore-fluid effects.

The t_{50} is referred to as the sedimentation time when the water-suspension interface is nearly at an elevation H/2 of the initial suspension height H during sedimentation tests. Figure 2.4 shows the ratios between sedimentation time in deionized water, kerosene and $(NaPO_3)_6$ solution respectively to that in NaCl solution versus specific surface. Ottawa 20-30 sand and fly ash are not affected by pore fluids. Ions of NaCl solution affect electrical interactions of particles and sedimentation time. Only kaolinite experiences shorter sedimentation time in deionized water than in NaCl solution: The sedimentation time for other soils in deionized water is longer than that in NaCl solution. The sedimentation time for soils in kerosene is shorter than that in NaCl solution. While fines in silica flour in $(NaPO_3)_6$ solution do sediment, the suspension interface of illite, diatom and bentonite in

$(NaPO_3)_6$ solution does not settle down in one day. Unfortunately, a clean interface is not always recognizable.

The penetration ratio is defined as the ball rod penetration depth through the sediment interface to the sediment height. Penetration ratios measured for all sediments and fluids are plotted in Figure 2.5 versus specific surface. Ottawa 20-30 sand sustained the ball rod in all cases. All other soils show pore fluid effects on penetration, in particular:

- The penetration depth in Ottawa 20-30 sand, coarse silica flour, fly ash and coarse diatom in deionized water is small: The penetration ratios are close to zero. On the other hand, the penetration ratio for kaolinite, ground illite and bentonite in deionized water are nearly one.
- Most soils that sedimented in kerosene experienced more penetration than those sedimented in other fluids: The ball rod did not fully penetrate either bentonite or illite in kerosene.
- Kaolinite experienced full invasion in all cases.

2.4 Analyses

2.4.1 Dilation in Soils

Natural non-plastic soils are likely to be dilative near surfaces of soil sediments because of low confining stress [Been and Jefferies, 1985; Santamarina and Shin, 2010]. Similarly, the shaking test shows dilative silt behavior. Dilation in plastic clays is limited by sliding friction along shear bands [Lupini et al., 1981], low friction angles [Kenney, 1967], and open fabrics that result from electrical interactions. Dilational shear resistance

was tested in insertion tests. Results show the potential of this method, however, sediment segregation during sedimentation hinders the systematic implementation of this approach.

2.4.2 Electrical Interactions

All soil particles have unbalanced surface charges. Based on surface charge, particles size and pore fluid, electrical DLVO interactions can govern particle behavior. The van der Waals attraction force develops between polar or polarized molecules [Santamarina et al., 2001; Israelachvili, 2011]:

$$F_{Att} = \frac{1}{24}\frac{A_h}{t^3}d^2 \qquad [2.3]$$

where the A_h [J] is the Hamaker constant, t [m] the distance between two platy particles, d [m] the diameter of the particles. The double-layer repulsion is caused by mineral surface charges [Santamarina et al., 2002]:

for large t, $$F_{DL} = 16\pi RTc_0 d^2 e^{-\frac{t}{\vartheta}} \qquad [2.4]$$

for small t, $$F_{DL} = \frac{1}{2}\pi RTc_0 d^2\left(\frac{2\pi^2\vartheta^2}{t^2} - 1\right) \qquad [2.5]$$

where R is the gas constant, 8.314 J/(K·mol), T the absolute temperature, c_0 [mol/L] the bulk fluid concentration, and the double-layer thickness ϑ [m] is:

$$\vartheta = \left(\frac{\varepsilon' kT}{2c_0 e_0^2 z^2 N_{av}}\right)^{\frac{1}{2}} = \left(\frac{\varepsilon' RT}{2c_0 z^2 F^2}\right)^{\frac{1}{2}} \qquad [2.6]$$

where ε' [farad/m] is the real permittivity of the solution; k Boltzmann's constant, 1.38×10^{-23} J/K; e_0 the elementary charge, 1.602×10^{-19} C; N_{av} Avogadro's number,

6.022×10^{23} 1/mol; z the valence of the prevailing cation; and F Faraday's constant, 96485.3 C/mol.

Electrical interaction explains the sensitivity of the liquid limit to grain size, fluid polarity and ionic concentration (Figure 2.3). The ratio between the liquid limit obtained with deionized water and that obtained with the NaCl solution reflects sensitivity to double-layer repulsion. The ratio of the liquid limit obtained with kerosene to that obtained with the NaCl solution illustrates the sediment electrical sensitivity to both van der Waals and double-layer effects.

2.4.3 Fall Cone Test

The trend for penetration depths versus water content for the fall cone test (BS 1377) becomes steeper when the liquid limit approaches 30%, which corresponds to the water content when coarse grains pack in a loose, simple cubic packing fabric. Electrically sensitive grains with high liquid limits have gentle slopes when mixed with deionized water, but slopes become steeper when mixed with the NaCl solution and with kerosene. These observations suggest a causal link between the slope of penetration versus water content and sediment-fluid electrical interaction.

2.5 Discussion – Recommendations

The compilation and analysis of experimental data have led to multiple correlations between soil classification and soil properties such as hydraulic conductivity [Göktepe and Sezer, 2010], compressibility [Sridharan and Nagaraj, 2000], and shear strength [Oda,

1972; Lupini et al., 1981; Jamiolkowski et al., 1985; Mitchell and Soga, 2005; Mayne, 2006].

A new approach to fine grain classification is proposed to extend the understanding of soil behavior to physical-chemical processes, by including electrical interactions with high salt concentration and non-polar hydrocarbons. Electrical sensitivity is assessed using the fall cone test to avoid particle size segregation (e.g. sedimentation tests). The selected fluids (deionized water, 2-M NaCl solution and kerosene) are readily available and capture electrical sensitivity of soils to van der Waals and double-layer effects. Results show that double-layer effects dominate in bentonite, but that both double layer and van der Waals attraction affect inter-particle interactions in kaolinite. Fly ash and diatoms exhibit low electrical sensitivity but high liquid limit. Hence, the proposed methodology distinguishes among intra-porous materials and plastic clays.

The electrical sensitivity of the sediments shown in Figure 2.3 combines van der Waals and double-layer effects using a Pythagorean distance:

$$S_E = \sqrt{\left(\frac{LL_{DW}}{LL_{NaCl}} - 1\right)^2 + \left(\frac{LL_{kerosene}}{LL_{NaCl}} - 1\right)^2} \qquad [2.7]$$

where S_E is the distance from the origin at $LL_{kerosene}/LL_{NaCl}=1.0$ and $LL_{DW}/LL_{NaCl}=1.0$ to the data point. The reciprocal of these ratios is used if they are less than 1.0.

The new chart shown in Figure 2.6 classifies soils based on the electrical sensitivity S_E and the liquid limit obtained with NaCl solution. Two boundaries drawn in Figures 2.3 and 2.6 divide soils into low electrical sensitivity (silica flour, fly ash and diatom), intermediate electrical sensitivity (kaolinite and illite), and high electrical sensitivity (bentonite). Intra-porous materials (e.g., diatoms and organic soils) show high liquid limits

with low electrical sensitivity. The use of liquid limit (in this case obtained with NaCl solution) can be preserved from earlier classifications to assess the extent of plastic behavior because it is a proxy parameter for specific surface.

Finally, the recommended procedure for fines classification follows:

1. Use the fraction that passes sieve No. 200.
2. Conduct liquid limit tests (BS 1377) with three different pore-fluids: deionized water, kerosene and 2-M NaCl solution.
3. Calculate electrical sensitivity S_E (Figure 2.2 and Equation 2.7).
4. Identify soil types using Figure 2.6.

2.6 Conclusions

Current soil classification systems define ambiguous boundaries between clays and silts, and multiple semantics for the same term "clay". Experimental studies in this chapter suggest new boundaries and parameters for the classification of fine-grained soils. It places emphasis on electrical sensitivity. Salient conclusions follow:

- The liquid limit, the plastic limit, and the specific surface of soils are highly correlated. The plasticity index helps distinguish plastic sediments with intra-pore grains (e.g., diatoms and organic materials) from high plastic clays.
- A critical aspect of sediment behavior is its response to changes in pore fluid chemistry, i.e., its electrical sensitivity.
- The fall cone test with different fluids can be used to classify fine grains into electrically sensitive soils and electrically non-sensitive soils. Electrically

sensitive soils are susceptible to either van der Waals force or double-layer repulsion.

- Electrical sensitivity includes underlying physical concepts in current soil classifications, such as mineral type, grain size, soil structure and shear resistance.
- Other index tests can provide valuable complementary information. The sedimentation test adds information related to pore fluid chemistry, but grains segregate while they are settling and interface is not always clear. Insertion tests identify the structure of fine grains: electrical force-dominated fabric or grain packing.

Table 2.1 Soil classification systems and fine grains: (a) fines contents and (b) liquid limits [%]

(a)

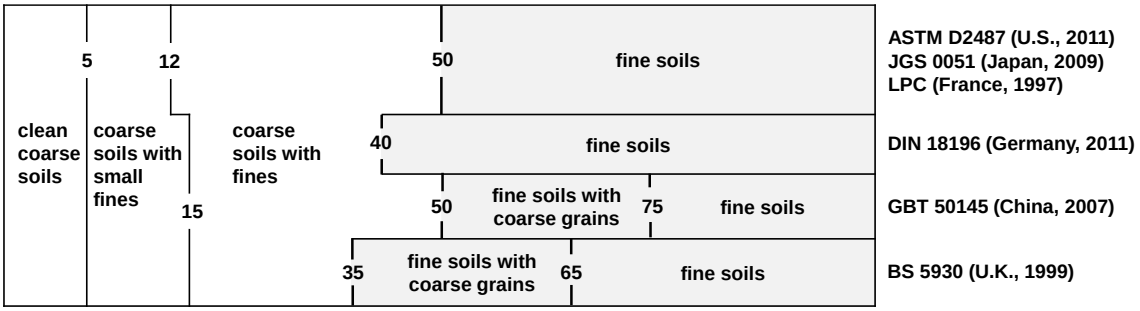

- Fine grain size: U.S., Japan and China < 75μm; France < 80μm; Germany and U.K. < 60μm
- The A-line on a plasticity chart divides silts and clays

(b)

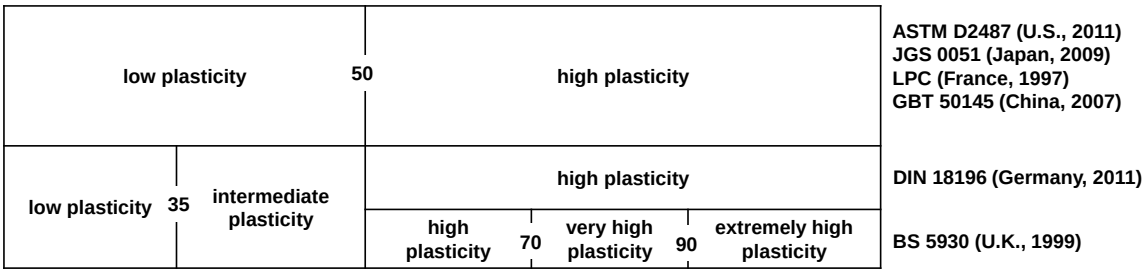

Table 2.2 Material properties: (a) pore fluids and (b) soils

(a)

	Water	K-1 Kerosene	Dispersant Solution	NaCl Solution
Molecular Formula	H_2O	N/A	$(NaPO_3)_6$ 40 g/L[(a)]	NaCl 1-2 mol/L
Relativity Permittivity at 20°C	80.4	1.8-2.0		1 mol/L: 65[(b)] 2 mol/L: 55[(b)]

[(a)] ASTM D422
[(b)] Santamarina et al. [2001]

(b)

	Ca-Bentonite	Diatom	Ground Illite	Kaolinite	Silica Flour	Fly Ash	Ottawa Sand 20/30
D_{50} [μm]	0.073*	10**	--	0.36*	20*	20*	720*
Liquid Limit, LL [%]	276	121	67	67	31	50	22
Specific Surface, S_s [m^2/g]	661	104	128	46	0.6	2.4	0.003***
Specific Gravity, G_s	2.5**	2.2**	2.2*	2.6*	2.65**	2.3*	2.65*
Weight [g]	5	5	5	5	20	20	40

*Literature
**Specification
***Calculation: LL=19+0.56S_s [Farrar and Coleman, 1967; Santamarina et al., 2001]

$$S_{s,sphere} = \frac{6}{d_{50}\rho}$$, ρ [kg/m^3] density

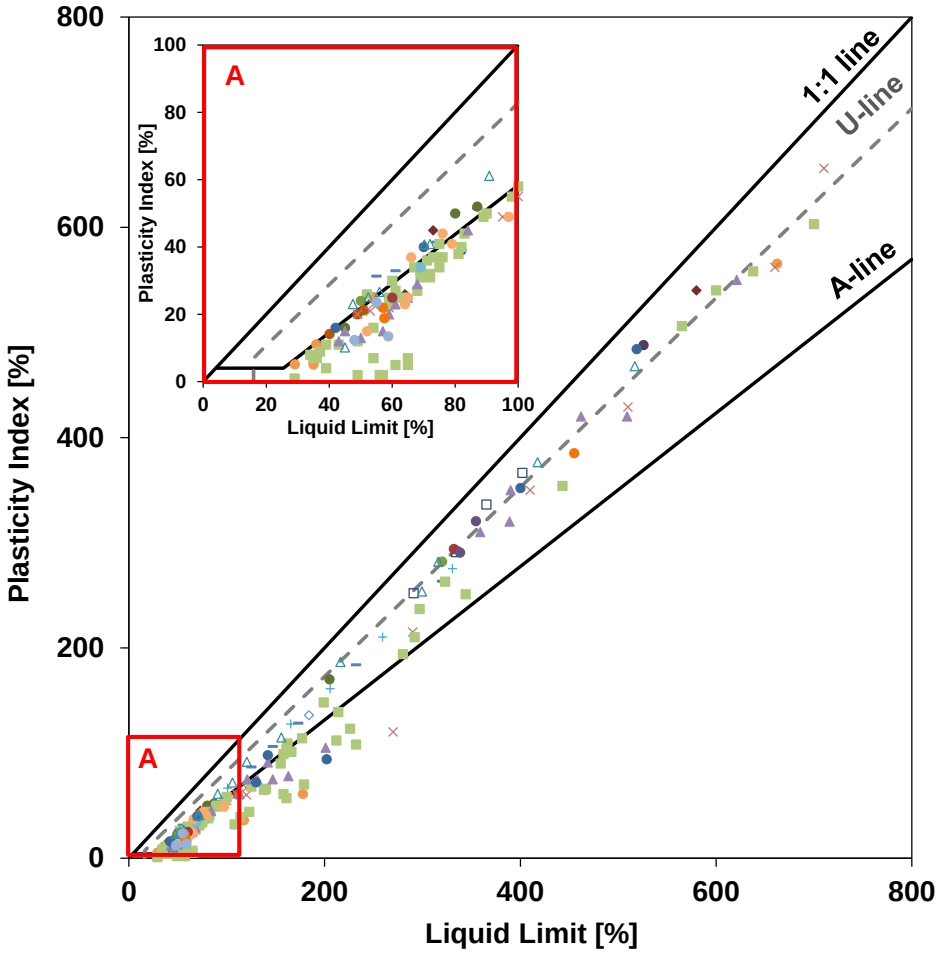

Figure 2.1 Clay minerals on the plasticity chart [White, 1949; Skempton and Northey, 1953; Grim, 1962; Seed et al., 1964; Lambe and Whitman, 1969; Lupini et al., 1981; Wood, 1982; Fukue et al., 1986; Mesri and Cepeda-Diaz, 1986; Wasti and Bezirci, 1986; Di Maio and Fenelli, 1994; Sridharan and Nagaraj, 1999; Donohew et al., 2000; Feng, 2000; Koumoto and Houlsby, 2001; Cerato and Lutenegger, 2002; Polidori, 2003; Tanaka et al., 2003; Sridharan and Nagaraj, 2004; Dolinar and Trauner, 2005; Spagnoli et al., 2012].

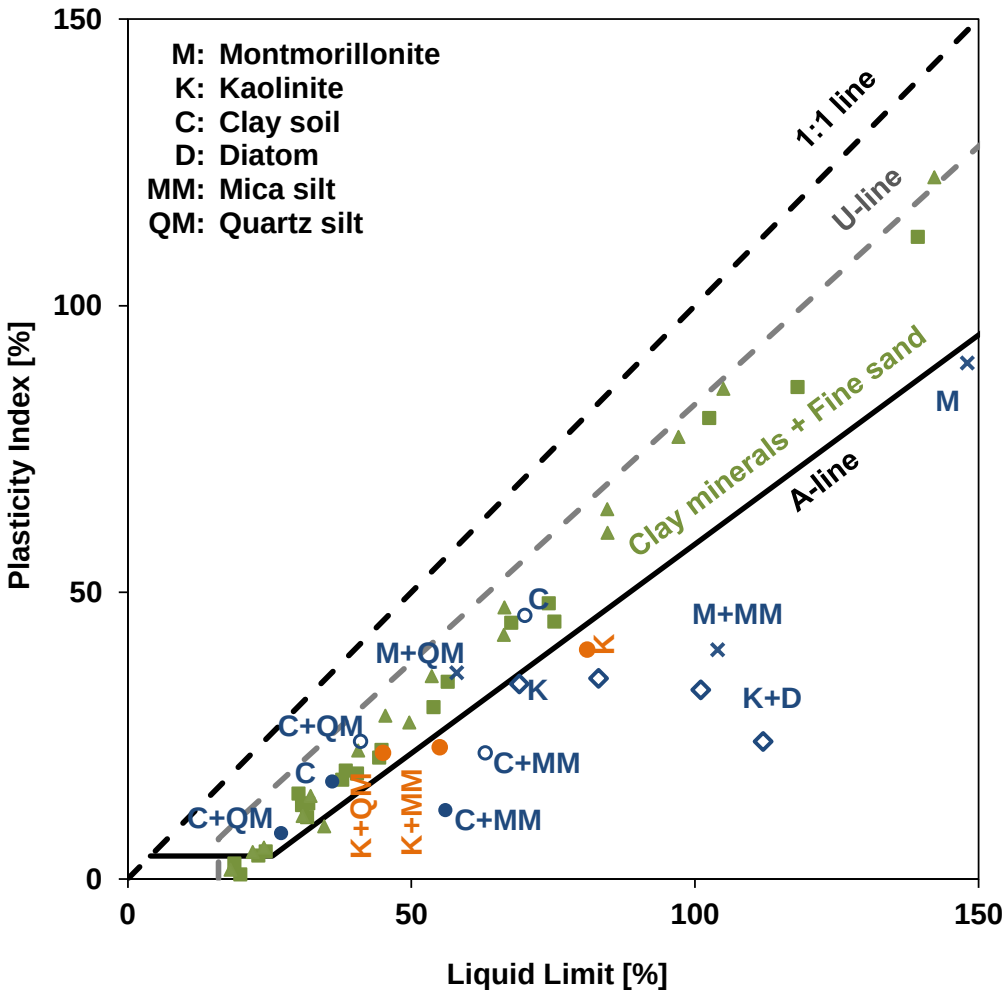

Figure 2.2 Mixtures of clays and non-plastic fines on the plasticity chart [Seed et al, 1964; Dumbleton and West, 1966; Tanaka et al., 2003].

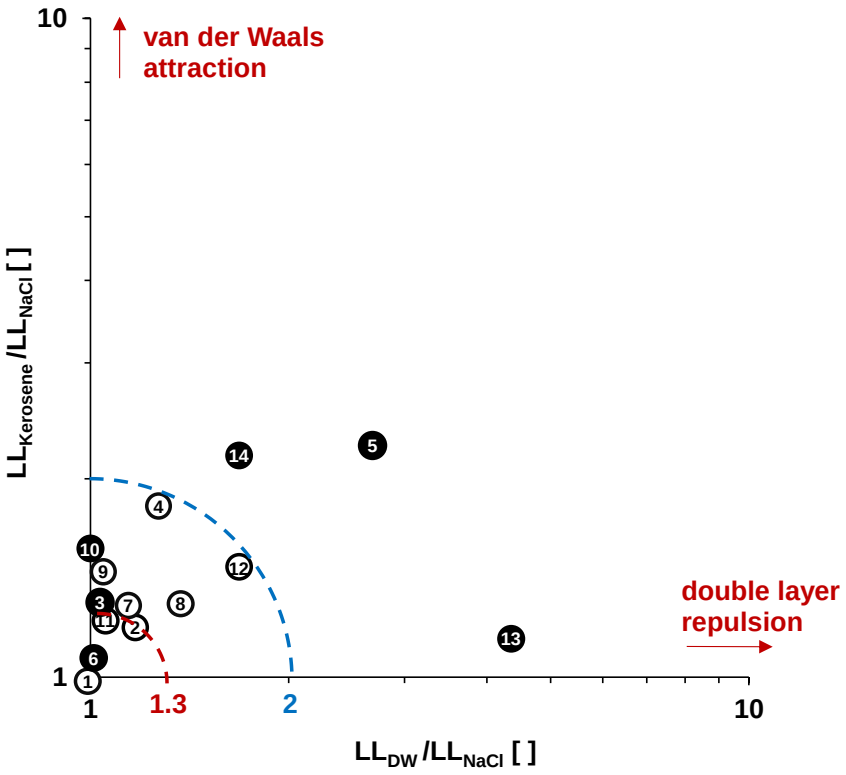

		LL [%]	PL [%]	S_s [m^2/g]	Passing No. 200 sieve [%]	Remarks
1	Ottawa 20-30 sand	22	N/A	--	--	at fluid saturation
2	silica flour	31	26	0.6	--	
3	diatom	121	113	104	--	
4	kaolinite	67	31	46	--	
5	Ca-bentonite	276	44	661	--	
6	fly ash	50	47	2.4	--	
7	Piedmont GA-1	53	34	23	100	
8	Clay Adairsville GA-1	65	37	--	97	PL from the material data sheet
9	silt Matanuska Glacier	33	--	--	100	
10	ground illite	67	29	128	--	
11	Piedmont GA-2	63	--	--	100	
12	Clay Adairsville GA-2	91	34	--	97	PL from the material data sheet
13	Ponza bentonite	390	--	--	88	Calvello et al., 2005
14	Bissacci clay	110	--	--	83	Calvello et al., 2005

Figure 2.3 Electrical sensitivity of soils.

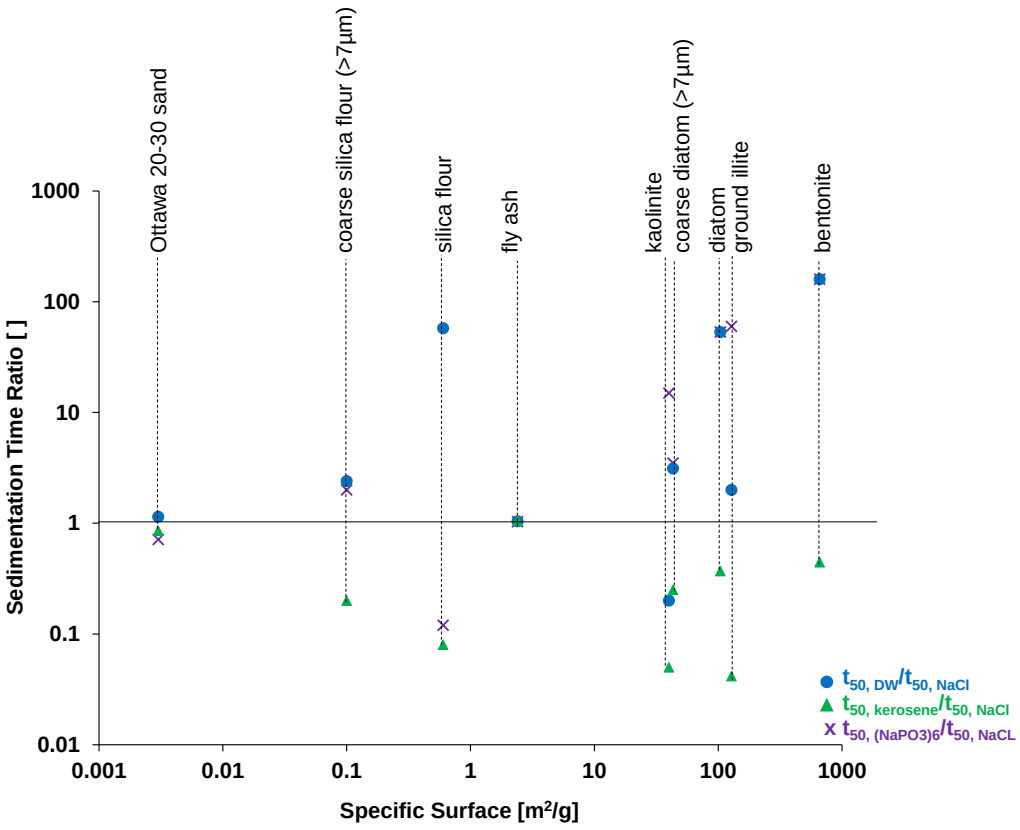

Figure 2.4 Sedimentation times: deionized water, kerosene and $(NaPO_3)_6$ to NaCl solution respectively.

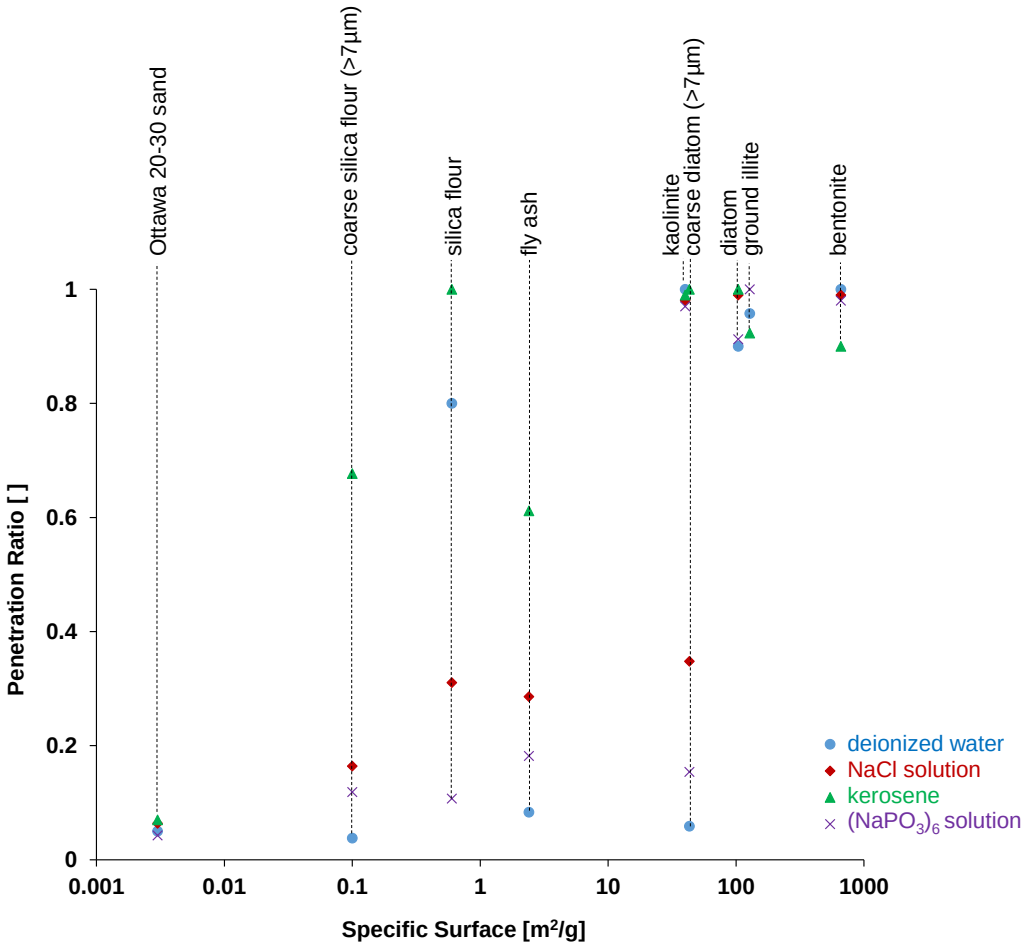

Figure 2.5 Penetration ratios by ball insertion tests.

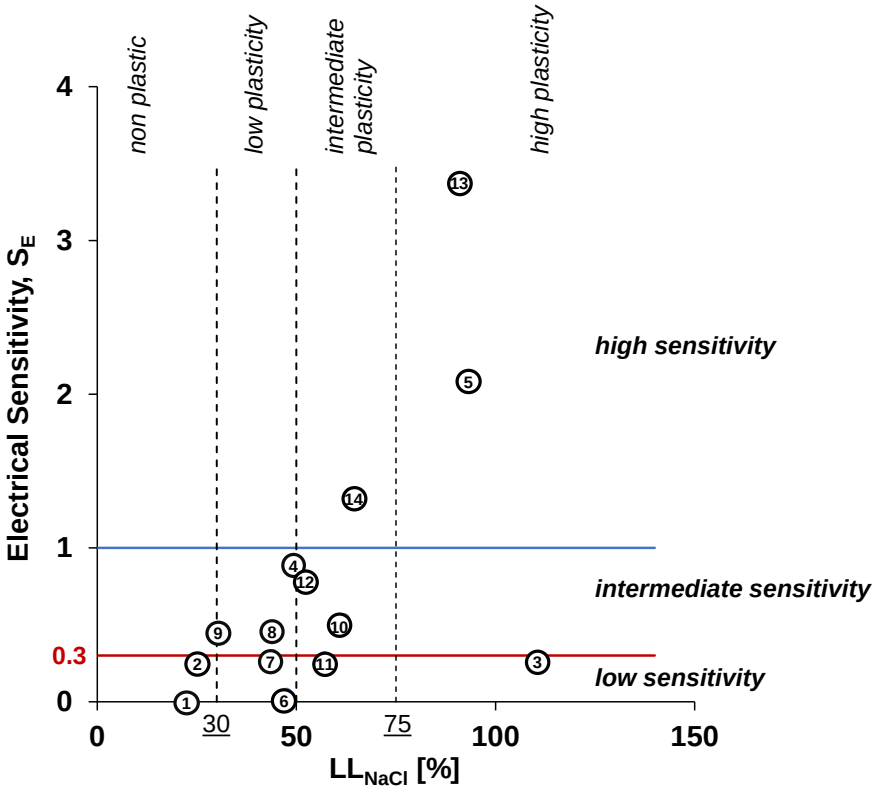

		LL [%]	PL [%]	S_s [m^2/g]	Passing No. 200 sieve [%]	Remarks
1	Ottawa 20-30 sand	22	N/A	--	--	at fluid saturation
2	silica flour	31	26	0.6	--	
3	diatom	121	113	104	--	
4	kaolinite	67	31	46	--	
5	Ca-bentonite	276	44	661	--	
6	fly ash	50	47	2.4	--	
7	Piedmont GA-1	53	34	23	100	
8	Clay Adairsville GA-1	65	37	--	97	PL from the material data sheet
9	silt Matanuska Glacier	33	--	--	100	
10	ground illite	67	29	128	--	
11	Piedmont GA-2	63	--	--	100	
12	Clay Adairsville GA-2	91	34	--	97	PL from the material data sheet
13	Ponza bentonite	390	--	--	88	Calvello et al., 2005
14	Bissacci clay	110	--	--	83	Calvello et al., 2005

Figure 2.6 New chart for fine-grained soil classification based on electrical sensitivity.

CHAPTER 3

VOLUME CONTRACTION DURING HYDRATE DISSOCIATION IN SANDY AND SILTY SEDIMENTS

3.1 Introduction

Methane hydrates dissociate when pressure and temperature (P-T) conditions fall outside the hydrate stability zone. Hydrate dissociation produces gas and water, is accompanied by large volume expansion, and can generate high pore pressure in sediments. The state of stress, the sediment type and density, and the hydraulic and mechanical properties will control slope stability [Sultan et al., 2004; Nixon and Grozic, 2007], the reservoir deformation during gas production [Rutqvist et al., 2009; Uchida et al., 2011] and well stability [Rutqvist and Moridis, 2007].

The experimental study of the mechanical behavior of hydrate-bearing sediments during hydrate formation and dissociation is challenging due to difficulties in generating methane hydrates. Alternatively, specimens can be prepared using analogues: tetrahydrofuran (THF)-hydrate has been used to study volume contraction in sediments during hydrate dissociation under zero-lateral strain conditions [Lee et al., 2010; Dai et al., 2011].

Similar to hydrate dissociation, ice melting in frozen ground causes surface subsidence [Watson et al., 1973; Nixon, 1991]. In fact, the mechanical properties of ice, methane-hydrates and THF-hydrates are very similar [Lee et al., 2007; Sloan and Koh, 2008; Jung and Santamarina, 2011]. The mechanical properties of hydrate- and ice-bearing

sediments depend on sediment conditions and either hydrate or ice content. The tensile and adhesive strengths of hydrates on mineral surfaces determine the hydrate contribution to the shear strength of a hydrate-bearing sediment [Jung and Santamarina, 2011], and its pore habit affects stiffness [Yun et al., 2007; Lee et al., 2010; Dai et al., 2011; Jung et al., 2012]. Likewise, ice saturation increases the strength and the volumetric strains during shear of frozen ground and it also changes the failure mode [Andersland et al., 1978; Lange and Ahrens, 1983; Nickling and Bennett, 1984; Arenson and Springman, 2005]. This chapter investigates volumetric changes in frozen unsaturated sediments during melting. The main goal is to determine upper bound asymptotic trends (using very loose sediments) of anticipated volumetric strain in hydrate-bearing silts during dissociation.

3.2 Thaw Consolidation

Heterogeneous nucleation triggers hydrate or ice formation at interfaces, such as mineral-water or water-gas; after nucleation, hydrate or ice grows into the pores [Taber, 1929; Liu, 2000; Waite et al., 2004; Dai et al., 2012; Jung and Santamarina, 2012]. Hydrate or ice growth in coarse-grained soils at high stress takes place by gradual invasion from one pore to the next. Consequently, coarse-grained soils inherently show little volume change during dissociation or thawing when fluids propagate through pores [Nixon and Ladanyi, 1978; Lee et al., 2010]. By contrast, fine-grained soils develop hydrate or ice lenses [Konrad and Morgenstern, 1980; Penner, 1986; Konrad and Duquennoi, 1993; Rempel, 2007; Dai et al., 2012]. Frost-susceptible soils such as silty clays exhibit high compressibility during dissociation or thawing resulting from the phase change of the

segregated hydrate or ice, and changes in the soil fabric [Chamberlain and Gow, 1979; Anderson et al, 1978; Lee et al., 2010]. The ratio between thaw and consolidation times R determines whether soils generate excess pore-water pressure, i.e., a comparison of the rates of heat and pressure diffusion:

$$R = \sqrt{\frac{D_T}{c_v}} \qquad [3.1]$$

where D_T [m^2/s] is the thermal diffusivity and c_v [m^2/s] is the coefficient of consolidation [Morgenstern and Nixon, 1971].

3.3 Experimental Study

3.3.1 Device

This study employed a zero-lateral strain oedometer cell (Figure 3.1). The specimen diameter is D=63.5 mm, and the diameter to height ratio is approximately D/H~3. Water can be injected from the bottom of the specimen.

3.3.2 Materials

Silica flour (Sil-Co-Sil 106) is selected for this study (mean diameter d_{50}=20 μm, specific gravity G_s=2.65, maximum void ratio e_{max}=1.51, minimum void ratio e_{min}=0.67 and specific surface S_s=0.6 m^2/g). The behavior of this sediment simulates deep marine hydrate-bearing sediments from the Nankai Trough (d_{50}=10 to 100 μm and a void ratio of 0.891 [JOGMEC, 2012]) and permafrost hydrate-bearing sediments at Mt. Elbert (d_{50}=100 to 200 μm and a void ratio of 0.72 [Winters et al., 2011]).

Figure 3.2a shows the compressibility of this silt when packed at different relative densities, as measured in the oedometer equipment shown in Figure 3.1. The compression index C_c is computed:

$$C_c = \frac{e_{1,000kPa} - e_{35kPa}}{\log \frac{1{,}000kPa}{35kPa}} \approx \frac{e_{1,000kPa} - e_{35kPa}}{1.5} \qquad [3.2]$$

The standard definition for relative density is adopted:

$$D_r = \frac{e_{\max} - e}{e_{\max} - e_{\min}} \qquad [3.3]$$

Note that high compression indices are observed for sediments with high initial void ratios (Figure 3.2b).

3.3.3 Procedure

Silica flour and water mixtures were packed to form density-controlled specimens inside the oedometer cell. The prepared specimens were placed in a freezer together with the loading caps. Frozen specimens were then mounted in the loading frame, subjected to loading, allowed to thaw under stress and finally water-saturated to assess any capillary-related stability. An LVDT tracked the specimen settlement during loading, thawing and subsequent saturation. Tests were repeated for specimens mixed at two water contents (ω_0=0.12 and ω_0=0.22) to control initial ice saturation, three initial densities (dense, intermediate, and loose) and for different vertical stress during thawing (σ'_0=50, 100, 200, 500 and 1,000 kPa) for a total of 30 tests.

Ice formed preferentially at contacts between particles due to capillary effects and water in pendular conditions at low water content. With this pore habit, ice exerts

maximum effect on soil stiffness and strength; the same is true in hydrate-bearing sediments [Yun et al., 2007].

3.3.4 Results

A typical change in void ratio versus time is schematically illustrated in Figure 3.3. Specimens responded rapidly to vertical load, and the associated settlement depended on the ice saturation, initial density, and applied stress σ'_0. Additional settlement took place during thawing and during final saturation because of capillarity loss.

Figure 3.4 shows the void ratio evolution from the initial condition, after loading, thawing, and saturation for all specimens. Capillarity supports the soil structure. Hence, the initial void ratio for all specimens with initial water content ω_0=0.12 and some of specimens with ω_0=0.22 reached higher than the maximum void ratio for silica flour e_{max}=1.51. The wide range in initial void ratios gradually narrowed from one step to the next. Specimens with initial water content ω_0=0.12 experienced more settlement during loading in the frozen condition than specimens with ω_0=0.22. After thawing, void ratios converged to values between e_{max} and e_{min}. The final void ratios after saturation were closer to e_{min} for specimens with initial water content ω_0=0.22 than for those specimens with ω_0=0.12, suggesting that memory of the initial fabric remains after loading, thawing and saturation.

3.4 Analyses and Implications

3.4.1 Volume Change

Volumetric strain ε_v is defined as the change in void ratio with respect to the initial void ratio at the beginning of each process:

loading $$\varepsilon_{v,l} = \frac{e_0 - e_i}{1 + e_0} \quad [3.4]$$

thawing $$\varepsilon_{v,th} = \frac{e_i - e_{th}}{1 + e_i} \quad [3.5]$$

saturation $$\varepsilon_{v,sat} = \frac{e_{th} - e_{sat}}{1 + e_{th}} \quad [3.6]$$

Results for all test are summarized in Figure 3.5. It can be observed that:

- High ice saturation leads to low strain during loading.
- The volume contraction during thawing is proportional to the initial void ratio (e_i, and e_{th}), the applied vertical load, and ice or water saturation.
- Low water contents induce high strains during saturation, similar to wetting collapse.

3.4.2 Volumetric Strains During Thawing in Sediments

Data in Figure 3.5 (ω_0=0.12 and 0.22) are combined with published results in Figure 3.6. Data correspond to two geological histories: hydrate formation after sediment loading from published data and sediment loading after hydrate formation from this chapter. The volumetric strain proportional to the initial void ratio e_i (after loading). Data for sediments with internal porosity deviate from the main trend.

The void ratio of packings made of mono-sized spheres varies from e_{max}=0.908 for simple cubic packing to e_{min}=0.351 for tetrahedral packing [Graton and Fraser, 1935; Deresiewicz, 1958]. In general, the e_{max} and e_{min} values depend on the coefficient of uniformity C_u and particle shape [Cho et al., 2006; Youd 1973]. Relative density is used in an attempt to generalize results obtained with a single sediment to other sediments. Figure 3.7 shows the relative density at the end of saturation D_r^{sat} plotted against the relative density before thawing D_r^i. Because of capillarity, initial void ratios are often greater than the maximum void ratio, so their relative densities are negative. Although the normalized input relative densities range from D_r=−1.5 to D_r=0.9, the final relative densities fall within D_r^{sat}~0.65±0.1 when the initial water content was ω_0=0.12, and within D_r^{sat}~0.75±0.1 when ω_0=0.22. The empirical equation derived for the trend is:

$$D_r^{sat} = a_w \tanh\left(b_w\left(D_r^i - 1\right)\right) + 1 \qquad [3.7]$$

where a_w and b_w depend on initial water content: a_w=0.37, b_w=2 for ω_0=0.12 and a_w=0.25, b_w=2 for ω_0=0.22.

The accumulated vertical strain during thawing and saturation for specimens tested at the same void ratio is plotted versus the applied vertical stress (Figure 3.8). Peak volumetric strains occurred around the vertical stress σ_z'=100 kPa when initial water content was ω_0=0.12 and σ_z'=500 kPa when ω_0=0.22; where the loading strain radically changes due to the failure of ice-particle contacts.

Estimated Vertical Strain. A method for estimating potential volumetric strains in silts during thawing (or hydrate dissociation) is suggested based on trends observed above.

Schematic trends in Figure 3.9 are based on experimental results in Figures 3.2 and 3.7. Calculation steps follow:

1) Identify the in-situ void ratio e_i and vertical effective stress σ'.

2) Measure e_{max} and e_{min} (i.e., remolded specimens), and determine the sediment compressibility for loosely and densely packed specimens as in Figure 3.2.

3) Compute the initial relative density at the in-situ state of stress.

$$D_r^i\Big|_\sigma = \left.\frac{e_{\max} - e_i}{e_{\max} - e_{\min}}\right|_\sigma \qquad [3.8]$$

$$\text{where } e_{\max}\Big|_\sigma = \left(e_{1kPa} - C_c \log\frac{\sigma}{1kPa}\right)_{D_r=0} \text{ and}$$

$$e_{\min}\Big|_\sigma = \left(e_{1kPa} - C_c \log\frac{\sigma}{1kPa}\right)_{D_r=100}$$

where the vertical bar with subscript σ implies that the parameter is evaluated at the in-situ vertical stress.

4) Estimate the post dissociation relative density D_r^t from D_r^i using the empirical relationship Equation 3.7 (Figure 3.7).

$$D_r^t\Big|_\sigma = f\left(D_r^i\right) \qquad [3.9]$$

5) Compute the void ratio after thawing (or dissociation)

$$e^v\Big|_\sigma = e_{\max}\Big|_\sigma - D_r^t\Big|_\sigma\left(e_{\max} - e_{\min}\right)\Big|_\sigma \qquad [3.10]$$

6) Compute the volumetric strain

$$\varepsilon_{diss}\Big|_\sigma = \left.\frac{e_i - e^v}{1 + e_i}\right|_\sigma \qquad [3.11]$$

3.6 Conclusions

Thaw-consolidation tests showed the extent of potential volume change that can be expected in hydrate-bearing sediments during dissociation. Salient conclusions follow:

- Initial void ratio and vertical effective stress determine the volumetric strain during thaw consolidation.
- Void ratios gradually converge between e_{min} and e_{max} during thawing and saturation. Final void ratios correlate with initial void ratios because the sediment retains memory of its initial fabric.
- Vertical strains resulting from hydrate dissociation can be estimated using the relationship between compression index and relative densities, and between input and output relative densities.

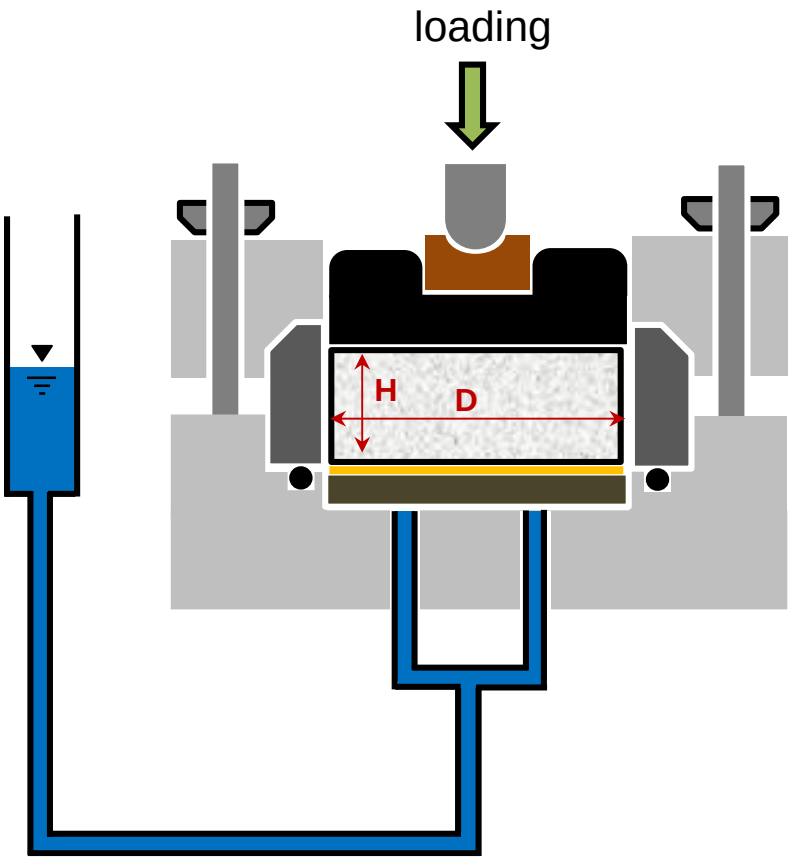

Figure 3.1 Experimental configuration used for thaw-consolidation tests.

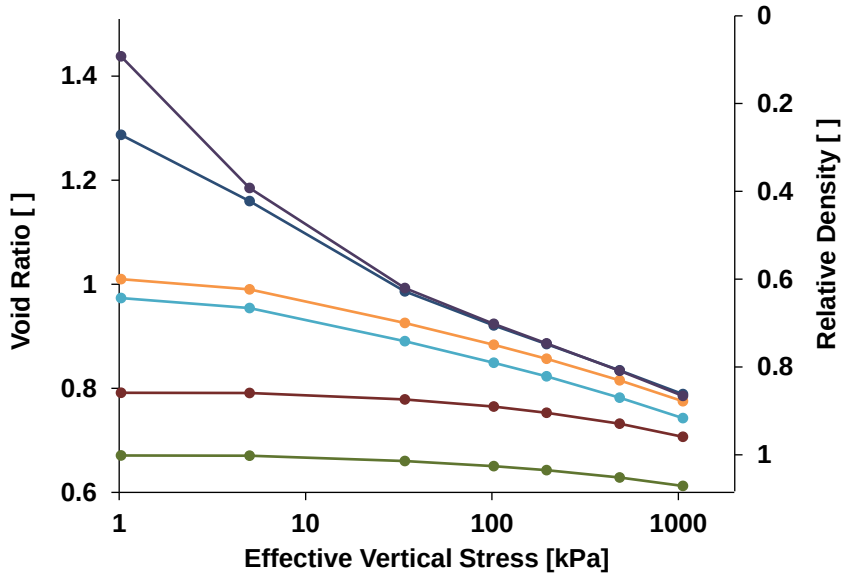

(a)

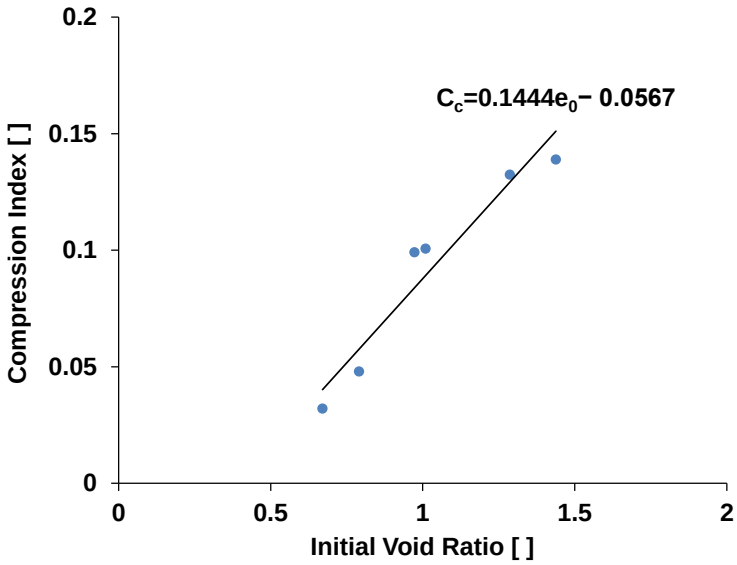

(b)

Figure 3.2 Silt compressibility: (a) test results at different relative densities (dry conditions) and (b) compression index between 35 kPa and 1,000 kPa as a function of initial void ratio.

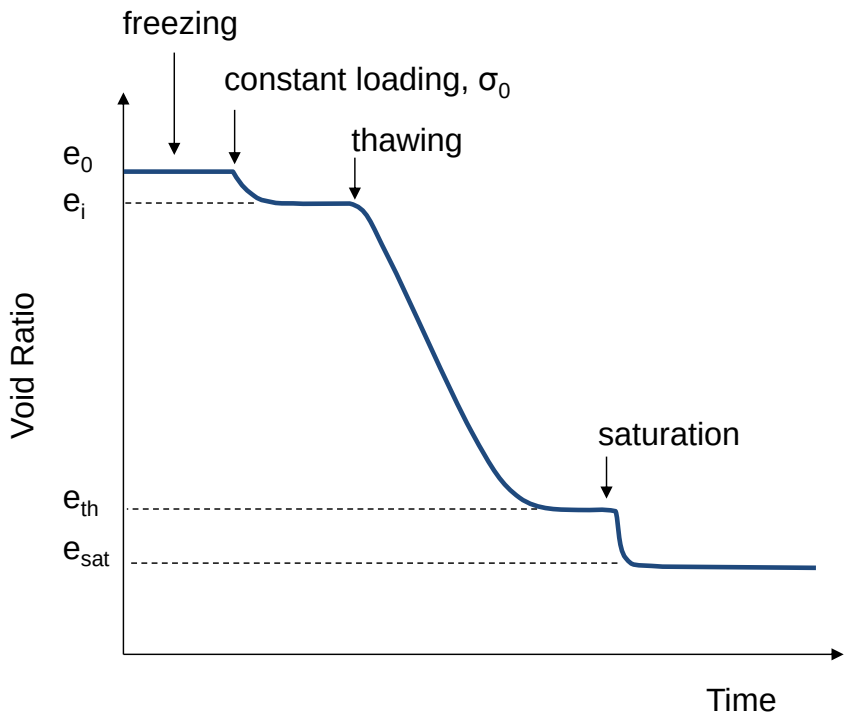

Figure 3.3 Schematic displacement-time trend. The test sequence includes: loading, thawing and saturation.

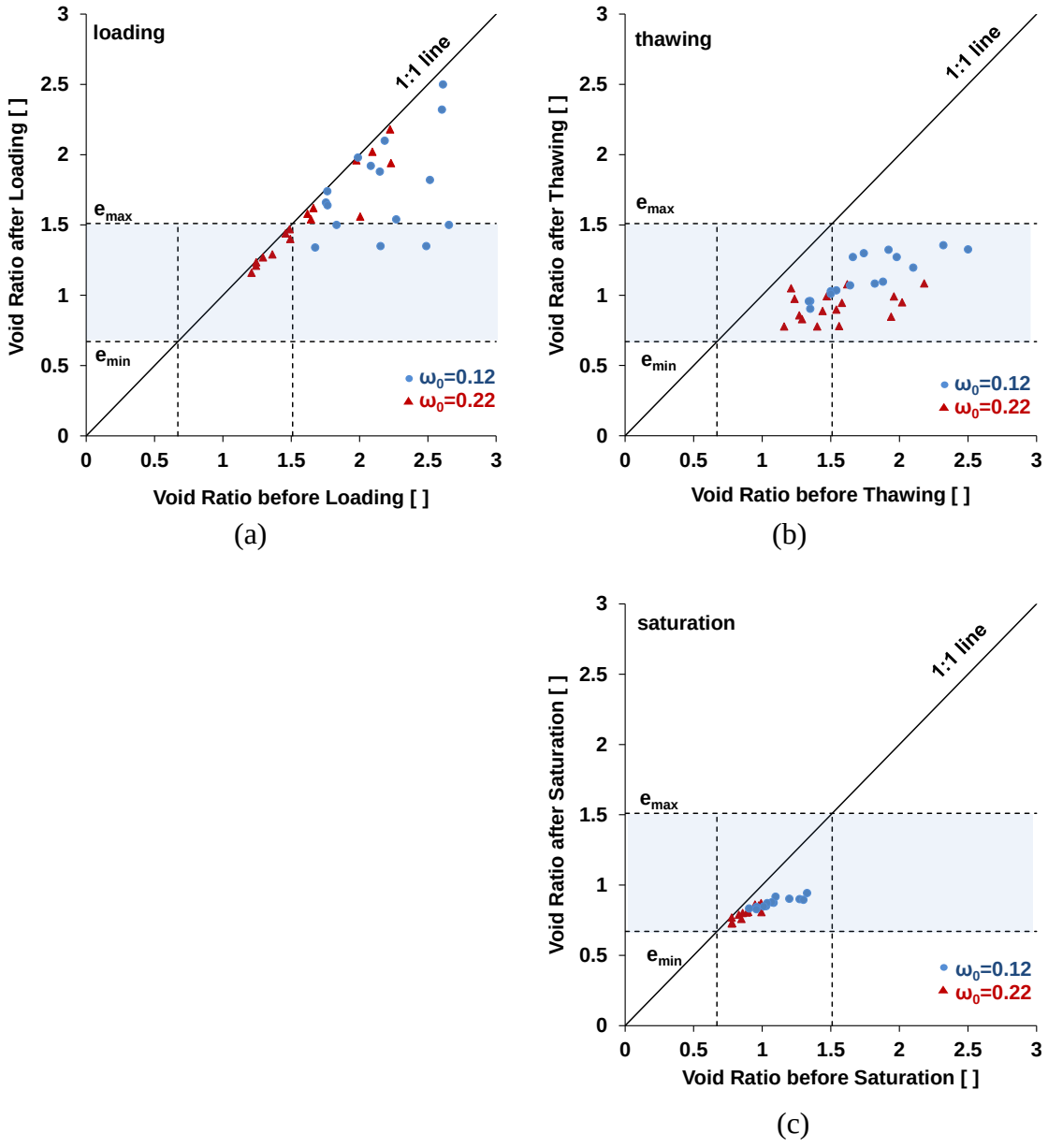

Figure 3.4 Void ratio change after freezing due to (a) loading, (b) thawing and (c) saturation.

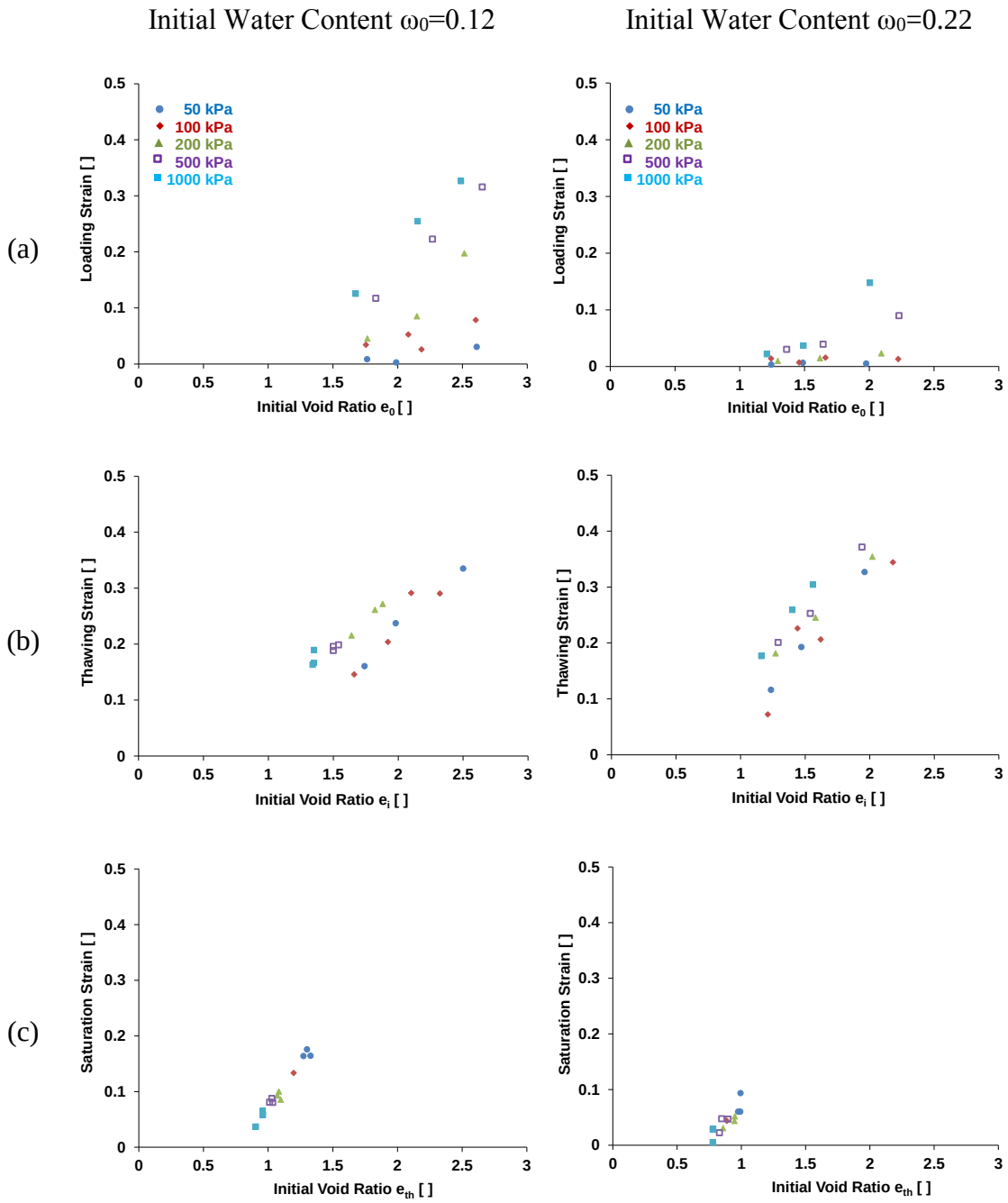

Figure 3.5 Compressive strain versus initial void ratio: (a) loading, (b) thawing and (c) saturation.

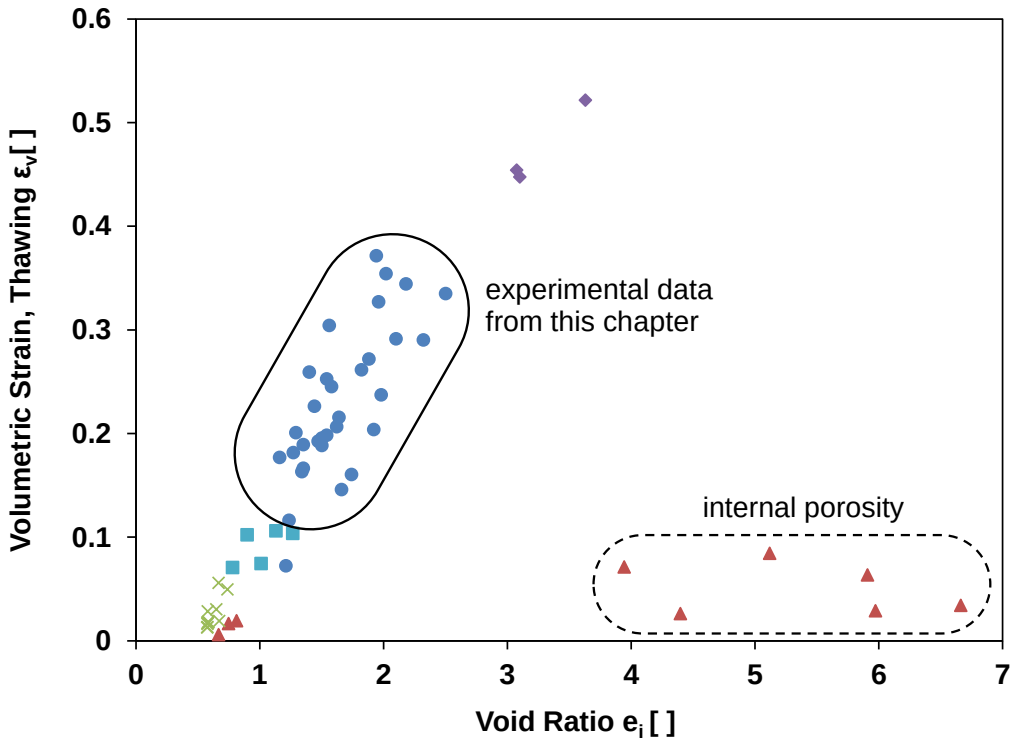

	Material	Vertical stress [kPa]	Reference
▲	Remolded silts & THF hydrate	10/100/510	Lee et al., 2010
×	Kaolinite-silt mixture & Ice	70/130/157/185	Konrad and Samson, 2000
◆	Permafrost core samples (clay)	380/600	Watson et al., 1973
■	Remolded clayey soils & Ice	18/36/150/218	Morgenstern and Smith, 1973

Figure 3.6 Volumetric strain during thawing as a function of the void ratio after the end of loading.

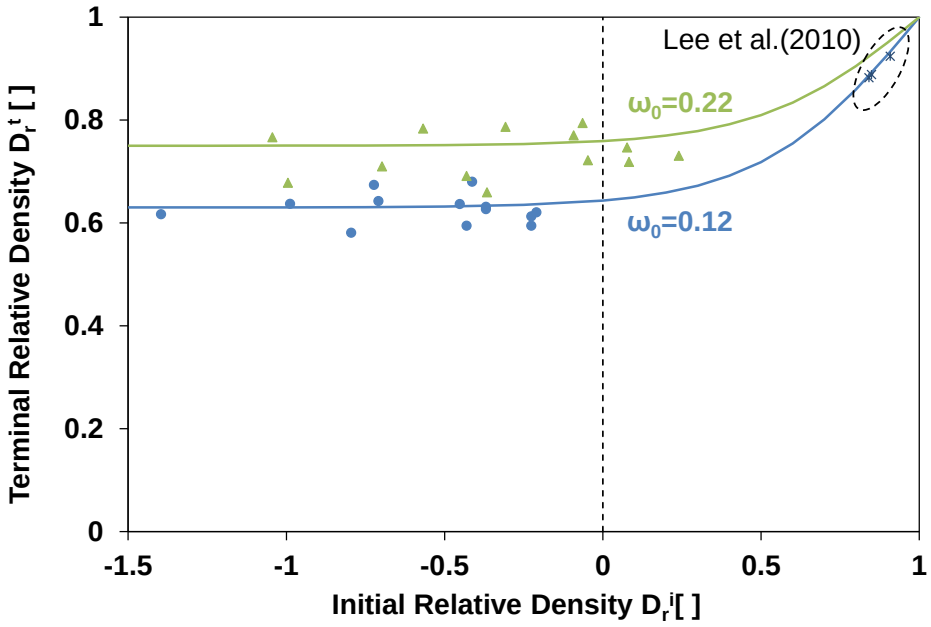

Figure 3.7 Relative density at the end of thawing and saturation, terminal relative density, D_r^t versus relative density before thawing, initial relative density, D_r^i.

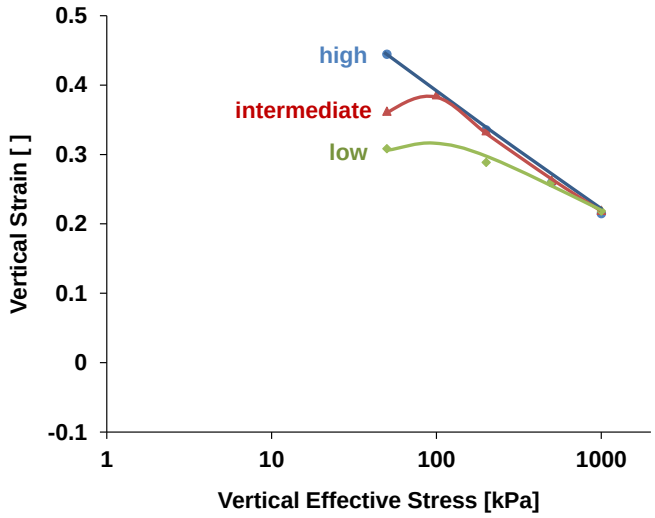

(a)

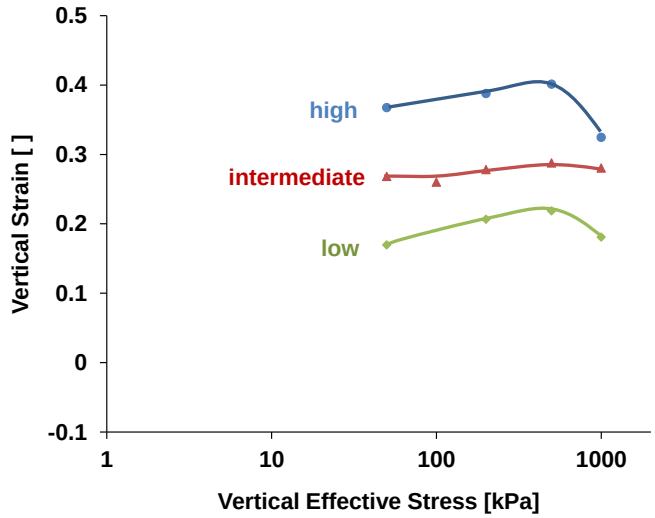

(b)

Figure 3.8 Combined vertical strain during thawing and saturation versus applied stress σ_0' for specimens prepared at different initial void ratios (high, intermediate, and low relative densities) and initial water content (a) ω=0.12 and (b) ω=0.22.

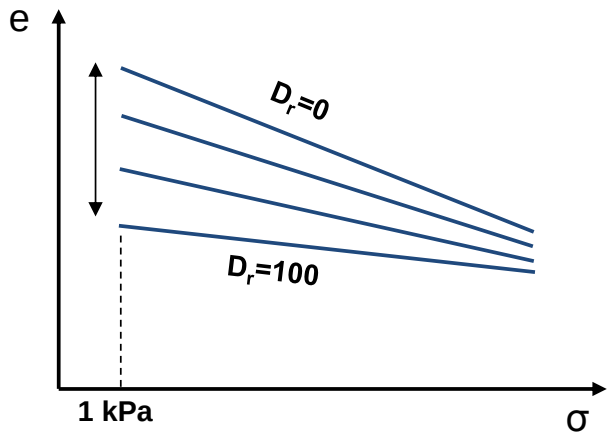

(a)

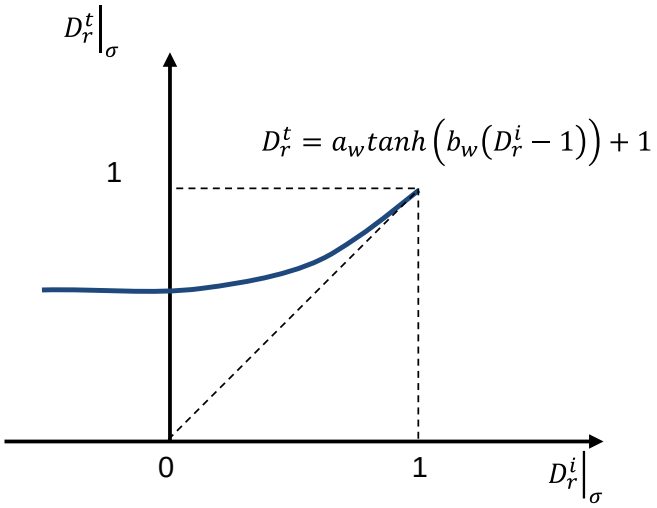

(b)

Figure 3.9 Method for the estimation of vertical strains due to hydrate dissociation in hydrate-bearing sediments: (a) compressibility at different relative densities – refer to Figure 3.2 and (b) normalized relationship between input and output relative densities – refer to Figure 3.7.

CHAPTER 4

THE EFFECT OF SURFACTANT SELF-REGULATION ON MIXED-FLUID FLOW – A PORE SCALE STUDY

4.1 Introduction

Hydrate-water interfacial tension in hydrate-bearing sediments determines the morphology and the occurrence of hydrates in sediments. Low capillary forces in large pores allow hydrate growth in sand pores [Dai et al., 2012]. High capillarity in fine-grained sediments shifts the phase boundary of the hydrate stability zone, it requires higher pressure and lower temperature to form hydrates [Clennell et al. 1999], and it leads to segregated hydrate formation.

Capillarity also plays a critical factor in multi-phase flow conditions such as during gas production [Jang and Santamarina, 2011; Jung et al., 2012] and CO_2 sequestration [Espinoza and Santamarina, 2012]. Gas production from hydrate-bearing sandy sediments is considered technically feasible because capillarity is low, and it allows gas flow through pore throats [Boswell and Collett, 2010].

Surfactants can be designed to reduce surface tension and help fluid flow through narrow pores in multi-phase systems such as CO_2 injection [Kim and Santamarina, 2014] and enhanced oil recovery EOR [Iglauer et al., 2010; Johannessen and Spildo, 2013]. This chapter documents the study of self-regulation effects that surfactants experience when approaching a pore throat. Fundamental concepts are reviewed first, followed by a unique experimental study at the pore scale.

4.2 Preliminary Concepts

4.2.1 Capillarity

The Laplace equation relates the capillary pressure difference Δp [kPa] between two fluids as a function of the interface geometry and the contact angle θ between the fluid interface and the solid substrate liquid-solid interface [Thomson, 1886; Bear, 1972; Cho and Santamarina, 2001],

$$\Delta p = T_s\left(\frac{1}{r_1}+\frac{1}{r_2}\right)\cos\theta \qquad [4.1]$$

where T_s [mN/m] the surface tension, r_1 and r_2 [m] are the two principal radii at the curved fluid interface. Young's equation relates three interfacial tensions T between the two fluids and the solid to the contact angle [Young, 1804],

$$\cos\theta = \frac{T_{sg}-T_{sl}}{T_{\mathrm{lg}}} \qquad [4.2]$$

where sub-indices correspond to s: solid, l: liquid, and g: gas.

Surface tension and the contact angle are not constant but change based on the interface conditions such as the roughness, wettability, velocity of the fluid in the tube, impurities, and pressure [de Gennes, 1985; Sharma and Ross, 1991; Kwok and Neumann, 2000; Miwa et al., 2000; Siebold et al., 2000; Espinoza and Santamarina, 2010]. The dynamic contact angle θ_D in advancing and receding conditions depends on the capillary number Ca [Rose and Heins, 1962; Hoffman, 1975; Tanner, 1979; Kalliadasis and Chang, 1994]:

$$\theta_D \propto C_a^{\frac{1}{3}} \qquad [4.3]$$

where the capillary number is defined as a ratio between viscous drag and capillary force:

$$Ca = \frac{\mu v}{T_s} \qquad [4.4]$$

where μ [Pa·s] is the fluid viscosity and v [m/s] the fluid velocity.

4.2.2 Surfactants

Surfactants are surface-active agents that can be designed or selected to reduce interfacial tension. They are endowed with a tendency to adsorb on interfaces and form micelles because of their amphipathic structure with hydrophobic and hydrophilic ends; the hydrophobic end moves away from water [Holmberg et al., 2003; Rosen, 2004]. According to electric properties of the hydrophilic group, surfactants are classified into anionic, cationic, zwitterionic, and nonionic [Rosen, 2004].

Surfactant Concentration and Micelles. Surface tension varies with surfactant concentration in the solution and the surfactant adsorption rate onto the interface [Defay and Prigogine, 1949; Miller et al., 1994]. Surfactants are adsorbed onto interfaces below their critical micelle concentration CMC, and surfactant concentrations on interfaces remain constant thereafter as excess surfactants in the bulk solution form micelles [Holmberg et al., 2003; Rosen, 2004]. Micelles are spherical, cylindrical, flat, and vesicular depending on the structure of the surfactant [Rosen, 2004; Israelachvili, 2011].

Surfactant Adsorption. Surfactant adsorption onto interfaces affects their efficiency and effectiveness. Surfactant efficiency relates the concentration required to attain a target surface tension. Surfactant effectiveness indicates the surfactant

concentration that produces the lowest surface tension [Rosen, 2004]. When the surfactant concentration is unbalanced along the interface, the surfactant density rapidly equilibrates driven by the surface tension gradient created by the unbalanced concentration, i.e., the Marangoni effect [Holmberg et al., 2003].

Surfactants in solution adsorb onto solid surfaces based on the bulk surfactant concentration. As the surfactant concentration increases, the adsorption onto solid surfaces reflects multiple interactions between solid surfaces and surfactants: electrostatic interactions between solid surface charges and surfactant head charges, lateral interactions among hydrophobic chains on solid surfaces, and lastly interactions between micelles and hydrophobic chains on solid surfaces when net electrical charges on solid surfaces become neutral as well as the bulk surfactant concentration reaches CMC [Zhang and Somasundaran, 2006]. The number of moles of an adsorbed surfactant on the adsorbent n_a^s [mol/g] is a function of the change in the mole number of surfactant in the solution Δn_s [mol] and the mass of the adsorbent m [g] [Rosen, 2004].

$$n_a^s = \frac{\Delta n_s}{m} = \frac{\Delta C V}{m} \qquad [4.5]$$

where ΔC [mol/L] is the molar concentration change in the surfactant from the beginning to the end of the adsorption, and V [L] the volume of the liquid phase.

Surfactant adsorption on a liquid-gas interface follows the Gibbs adsorption equation for a monolayer [Eastoe and Dalton, 2000; Rosen, 2004]:

$$dT_s = -\sum_i \Gamma_i d\mu_i \qquad [4.6]$$

where dT_s [N/m] is the change in the interfacial tension of the solvent, Γ_i [mol/m^2] the surface excess concentration of any component of the system, and $d\mu_i$ [J/mol] the change

in the chemical potential of any component of the system. Other isothermal equations such as the Henry, Langmuir, Frumkin, and Szyszkowski isotherms can be applied to liquid-gas interfaces as well [Eastoe and Dalton, 2000; Rosen, 2004]

4.2.3 Self-regulation: the Biological Analogy of the Respiratory System

The capillary effects of surfactants in multi-phase systems gain special relevance in the lungs. Pulmonary surfactants reduce the liquid-air surface tension T_{eq}=10 mN/m or less [Pattle, 1955; Schurch et al., 1976; Schurch et al., 1992]. The lipid dipalmitoylphosphatidylcholine DPPC reduces the surface tension of the alveolar film, and proteins SP-B and SP-C enhance the adsorption rate of the surfactant onto the alveolar surface [Hawgood and Clements, 1990; Creuwels et al., 1997; Goerke, 1998; Veldhuizen et al., 1998].

Alveolar expansion and contraction alter the surfactant concentration and adsorption during breathing [Clements et al., 1958; Ghadiali and Gaver, 2000; Ghadiali and Gaver, 2008]: the concentration of the surfactant is lower and the surface tension is higher in the expanded alveolus than that in the contracted alveolus. This self-regulating mechanism helps exhale, inhale, and prevents the abnormal expansion or shrinkage of neighboring alveolar sacs.

4.3 Experimental Study

The purpose of this study is to investigate the effect of surfactant self-regulation at pore throats during mixed fluid flow. Tests were conducted using deionized water DW,

alcohol and detergent. Table 4.1 lists the main compositions of the detergent. Ethanol is a co-surfactant [Liu et al., 2003] and amine oxide is a cationic surfactant or foam stabilizer [Rosen, 2004]. These additives decrease surface tension and increase the solubility of surfactant, i.e., the synergistic effect [Holmberg et al., 2003; Rosen, 2004]. Without additives, the critical micelle concentration of the sodium dodecyl sulfate is 0.0082 mol/L [Folmer and Kronberg, 2000; Holmberg et al., 2003]; the required detergent to reach this concentration is approximately 0.01 g/g when the molar mass of sodium dodecyl sulfate is 288 g/mol.

4.3.1 Surface Tension

A ring tensiometer is used to measure surface tension of fluids used in this project. The tensiometer consists of a torsion wire and a platinum-iridium ring with a mean circumference of 59.35 mm; the ratio of the ring major radius to the wire radius is 53.2.

Figure 4.1 shows the air-liquid surface tension of deionized water, alcohol, detergent, and aqueous detergent solutions at different concentrations (Table 4.2a). The surface tension of aqueous detergent solution is near the minimum value, which corresponds to the critical micelle concentration, for all tested concentration.

4.3.2 Pore-Scale Tests – Experimental Procedure

The 74 mm long glass capillary tube used for this study has outside diameter of 1.4 mm and inside diameter of 0.88 mm. A constriction is formed by localized heating. The constricted capillary tube was connected to the injection syringe through stainless steel tubing and saturated by the test liquid to minimize volume changes due to pressure changes.

The general configuration is sketched in Figure 4.2. The micro-control syringe pump (volume: 5 mL; inside diameter: 9.3 mm) maintained constant flow rates during either advancing or receding tests. Imposed flow rates are summarized in Table 4.2b: propagation velocity along the cylindrical capillary tube, Reynolds number Re and the capillary number Ca are included in the table. The advancing test at 20 μL/hr flow rate was conducted on the dry tube surfaces: all other tests were conducted on pre-wet surfaces.

4.3.3 Results

Test results are summarized in Figure 4.3 in terms of pressure-position p-x signatures when liquid-gas interfaces transit across the constricted region, for all fluids and injection rates (Note: pressure-position signatures are computed from the recorded pressure-time data using the imposed injection rate; as the system was not absolutely rigid, the results do not necessarily capture proper x-position information such as signature width). The measured pressure combines a hydrostatic component, drag, and capillary pressure. The peak pressure during advancing and receding tests occurred at the constriction, and decreased as the surfactant concentration increased. The pressure signatures for 0.05 g/g surfactant concentration solution were similar to those for alcohol. The shape of signatures gathered during advancing tests changed with surfactant concentration.

During advancing tests the pressure decreased as the interface moved towards the necking, increased when the interface was at its narrowest point, and then dropped just after the interface passed the narrowest point (Figure 4.3).

During the receding flow, the water pressure decreased as the interface moved toward the necking, then suddenly snapped to the steady state value. Surfactant solutions above the 0.1 g/g concentration and alcohol formed films that blocked the airway at the necking. This film broke and regenerated several times producing the oscillatory pressures cycles seen in the signature.

4.4 Analyses and Discussion

The hydrostatic pressure is constant. The drag resistance increases as the air-liquid interface advances, but it decreases when the interface recedes Note that the drag component is not recognizable in the zoomed-in signatures plotted in Figure 4.3. Then, the capillary pressure is the controlling component in the pressure variation seen in p-x signature.

Capillary pressure p_c [Pa] depends on surface tension T_s [N/m], the contact angle θ, the geometry of the flow channel, the angle α_x between the tube surface and the tube direction, and the tube radius r [m] (Figure 4.4)

$$p_{c,x} = \frac{2T_{s,x}\cos(\alpha_x - \theta_x)}{r_x} \qquad [4.7]$$

where the sub-index x indicates local value at position x. The air-liquid interface can snap from concave to convex for certain α and combination as shown in Figure 4.5.

The capillary pressure signature is analytically computed and plotted in Figures 4.6. Trends illustrate the capillary pressure signature when the surface tension remains constant, $T_{s,x}$=constant. Figures 4.6 illustrates effects of surface tension on capillary pressure: as experimentally observed, the amplitude of pressure signatures decreases when surface

tension decreases. In particular, the peak amplitudes predicted for T_s=0.072 N/m are three times greater than for T_s=0.025 N/m as pressure scales linearly with surface tension when the surface tension $T_{s,x}$=constant. Most importantly, p-x signatures change dramatically with contact angle (Figure 4.6).

If the surfactant effectiveness and adsorption rate oscillate as the fluid traverses the constriction, similarly to breathing, then measured p-x signatures should deviate from linear T_s-proportionality. Figure 4.7 explores the effects of surfactant self-regulation by plotting pressure ratios at key signature values (Figure 4.7a) versus surfactant concentration. The measured pressure at the constriction continuously changed (Figures 4.7 and 4.8) while the surface tension remained nearly constant as surfactant concentrations increased. While the air-liquid interface passes through the narrow region, surfactant molecules at the air-liquid interface repel each other, i.e., surfactant desorption in Figure 4.9a and decreases the surface tension as neighboring surfactants come closer together according to Equation 4.6 (Figure 4.9b); surfactants behind the interface prevent desorption of surfactants on the surface. The deviation of pressure signatures also reflects the synergic interaction between the surfactant mixture and the solid surface [Huang et al., 1989; Schulz and Warr, 2002; Zhang and Somasundaran, 2006]. We infer that while the charge of main surfactant head and the solid surface are negative, other components such as zwitterion surfactants and hydrocarbon additives can neutralize the solid surface charges and drive other surfactant interactions for the surfactant adsorption on solid surfaces. As seen in Figure 4.7, the capillary pressure is nearly constant above the surfactant concentration of 0.001 g/g, when the solution attains the maximum effectiveness.

Contact angles determine the shape of the interface. When the interface advances, contact angles increase in proportion to the capillary number (Equation 4.3). Indeed, as soon as an interface began receding, the measured pressure dropped because of the transition from a static to dynamic contact angle.

Surface tensions alter the contact angle based on Young's equation (Equation 4.2). Thin residual solution on a pre-wet surface affects the gas-solid interfacial tension, and surfactants also affect the liquid-solid interface. Observed contact angles were greater on the dry surface than on the pre-wet surface, so the pressure amplitude decreases when moving along pre-wet surfaces (Figure 4.7),

4.5 Conclusions

The capillary pressure varies as a mixed fluid interface traverses pore throats. The pressure-position signature results from interfacial tension, contact angle, pore throat geometry. In the presence of surfactants, self-regulation alters interfacial tension and contact angle along the necking. Experimental results and associated analyses support the following conclusions:

- Surfactants modify both surface tension and contact angle: Higher surfactant concentration leads to smaller the surface tension until a plateau related to micelle concentration is reached.
- Surfactant self-regulation results from changes in surfactant concentration at pore throats. Surfactant self-regulation changes the direction of surfactant

adsorption and desorption on the gas-liquid interface according to the flow channel geometry. This process modifies the effectiveness of surfactants.

- Pressure-position signatures during air-liquid interface displacement across throats reflect local changes in surface tension in agreement with self-regulation.
- The surfactant adsorption not only onto the gas-liquid interface but also onto the liquid-solid interface define the capillary pressure during the gas-liquid interface displacement through pore throats.

Table 4.1 Detergent: Chemical composition

Component	Concentration
ethanol	1 - 5 %
sodium laureth sulfate (sodium lauryl ether sulfate, SLES)	10 - 30 % (anionic surfactant)
sodium lauryl sulfate (sodium dodecyl sulfate, SDS)	
alkyl dimethyl amine oxide (amine oxide, C10-16)	3 - 7 % (zwitterionic surfactant)

Table 4.2 Experimental study: (a) solution concentration and (b) flow parameters

(a)

Liquid	Concentration of Detergent in Water [g/g]
aqueous surfactant solution	0.0001 0.00025 0.0005 0.001 0.0025 0.005 0.01 0.025 0.05

(b)

Flow Rate [μL/hr]	Velocity [m/s]	Reynolds Number Re*	Capillary Number Ca
20	9×10^{-6}	8	1.3×10^{-7}
40	18×10^{-6}	16	2.5×10^{-7}
80	37×10^{-6}	32	5×10^{-7}
160	73×10^{-6}	64	10×10^{-7}

* $\mathrm{Re} = \frac{\rho v d}{\mu}$ where ρ [kg/m^3] is the fluid density, v [m/s] the fluid velocity, d [m] the pipe diameter, and μ [Pa·s] the fluid viscosity.

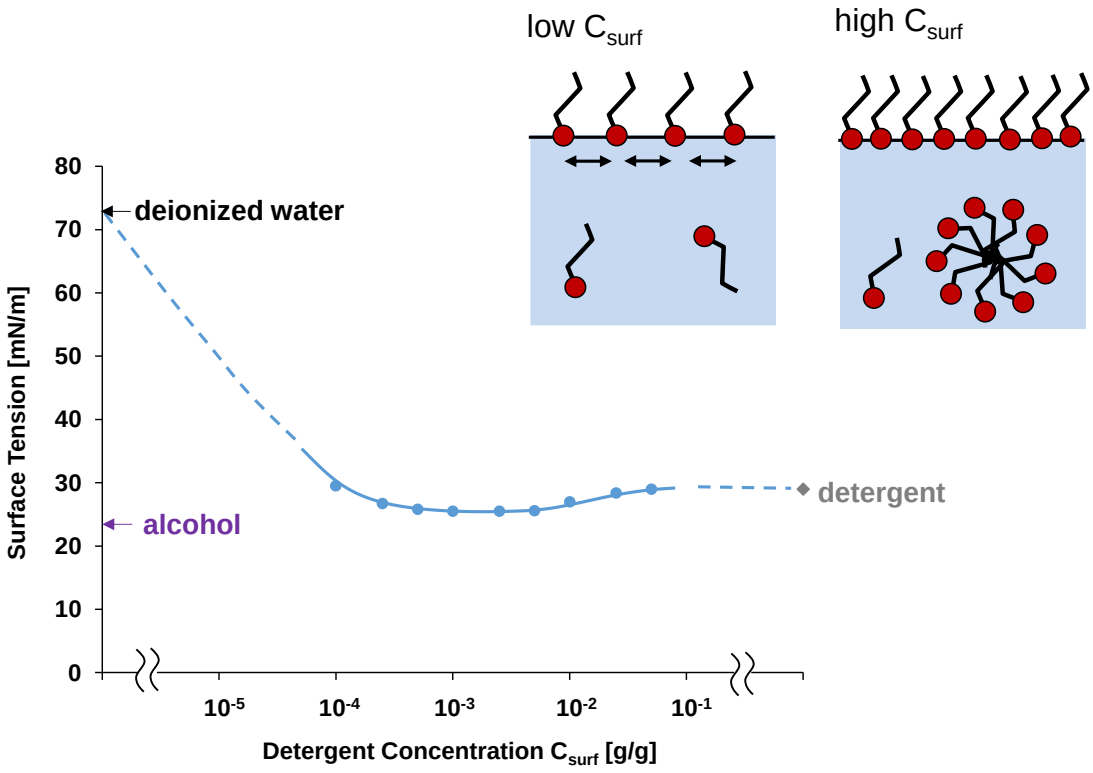

Figure 4.1 Air-liquid surface tension as a function of surfactant concentration.

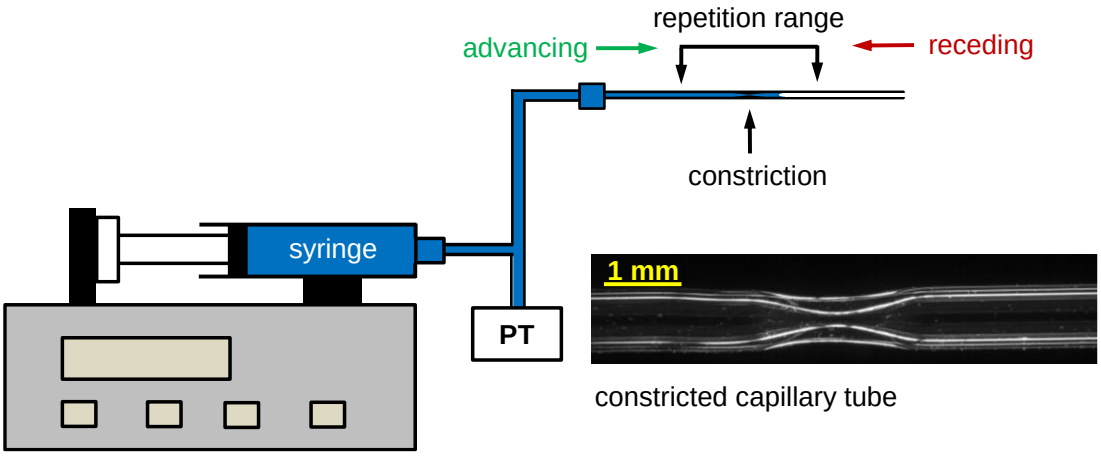

Figure 4.2 Experimental configuration to study capillary effects in a constricted capillary tube.

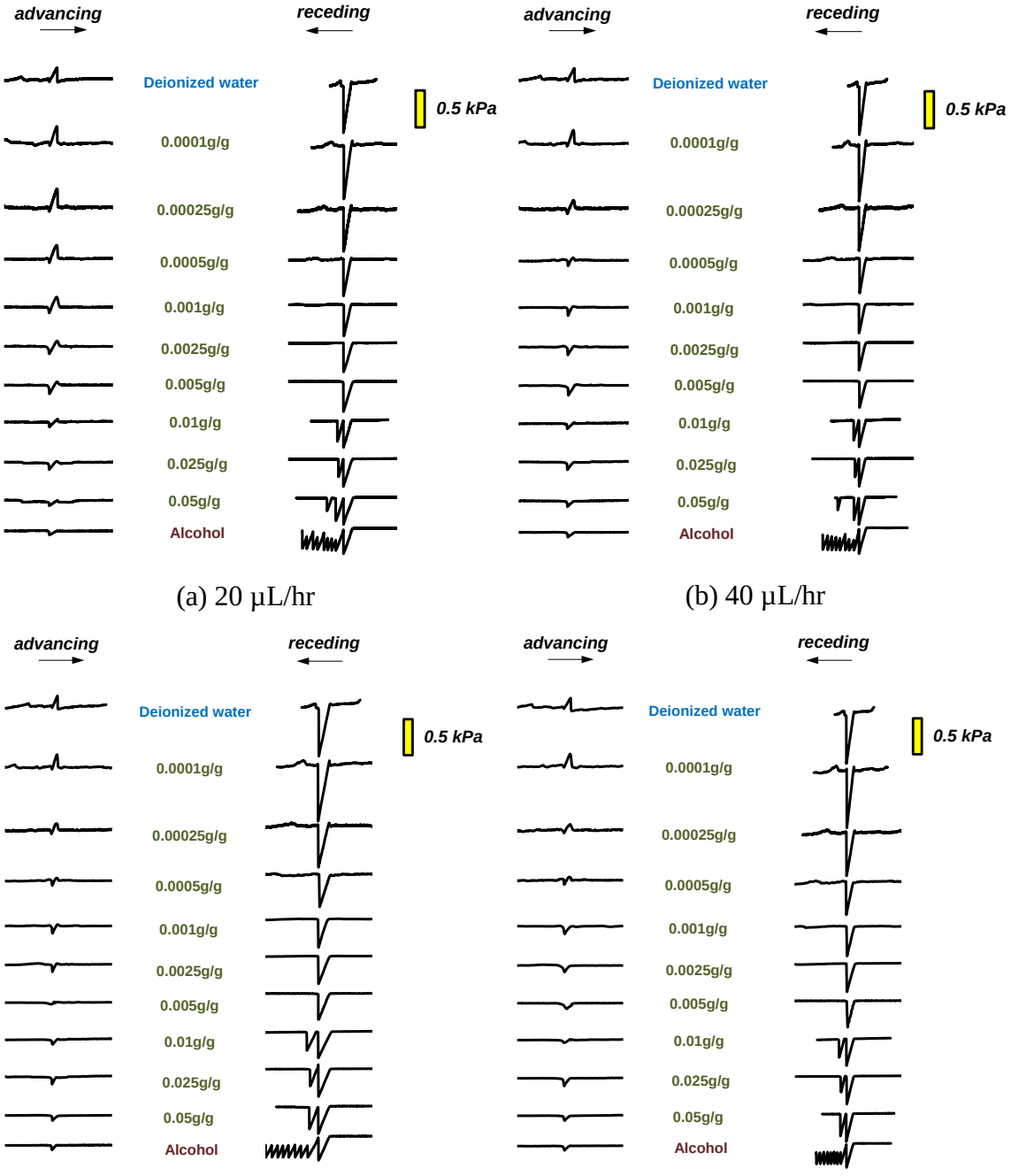

(a) 20 µL/hr (b) 40 µL/hr

(c) 80 µL/hr (d) 160 µL/hr

Figure 4.3 Pressure-position p-x signatures measured for different fluids across a constriction during advancing and receding tests. Flow rates: (a) 20 µL/hr, (b) 40 µL/hr, (c) 80 µL/hr and (d) 120 µL/hr.

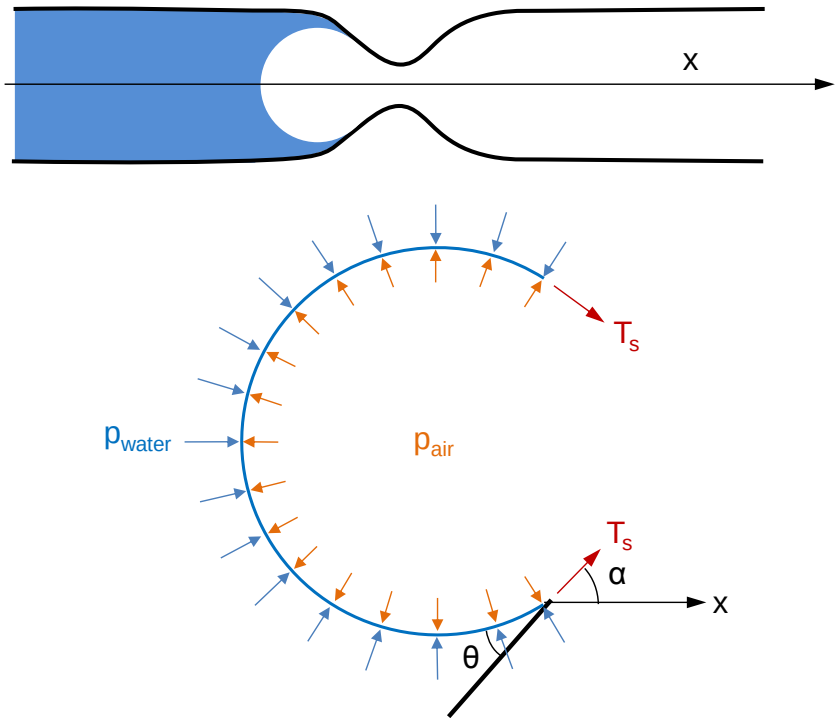

Figure 4.4 Schematic configuration of the air-liquid interface and capillary pressure near the constriction point.

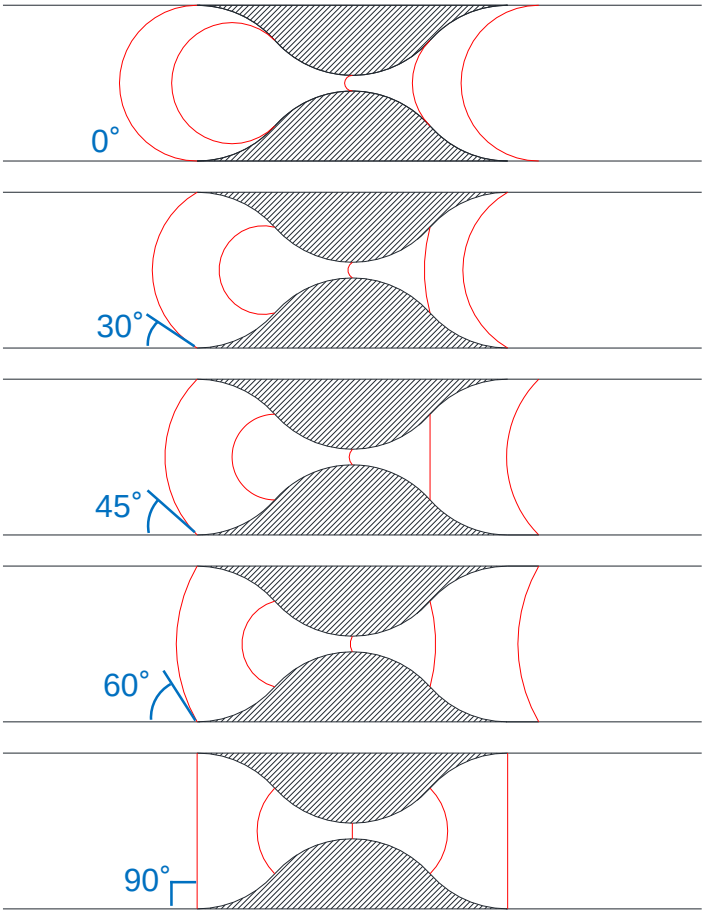

Figure 4.5 Menisci shapes near a constriction in a capillary tube.

(a)

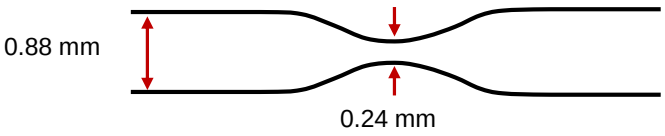

(b)

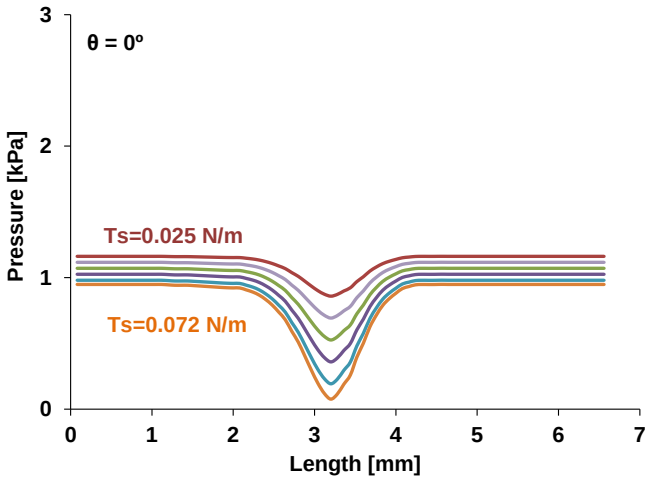

(c)

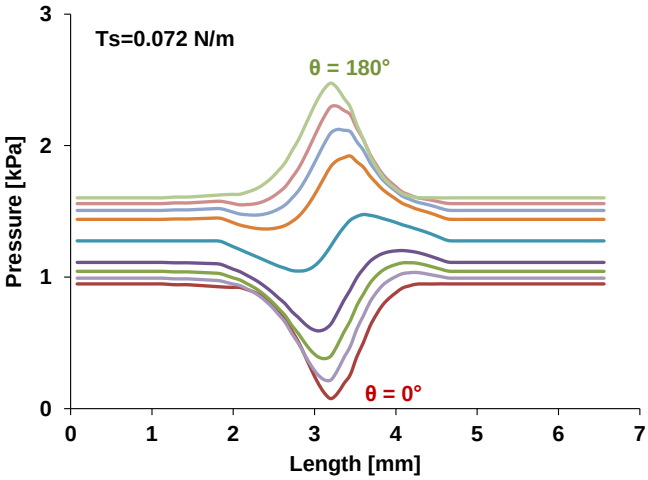

Figure 4.6 Analytically computed capillary pressure-position p-x signatures as a function of contact angle and surface tension (No self-regulation): (a) the assumed tube geometry is a cosine function, (b) constant contact angle with T_s=0.025, 0.035, 0.045, 0.055, 0.065 and 0.072 N/m and (c) constant surface tension with θ=0°, 30°, 45°, 60°, 90°, 120°, 135°, 150° and 180°.

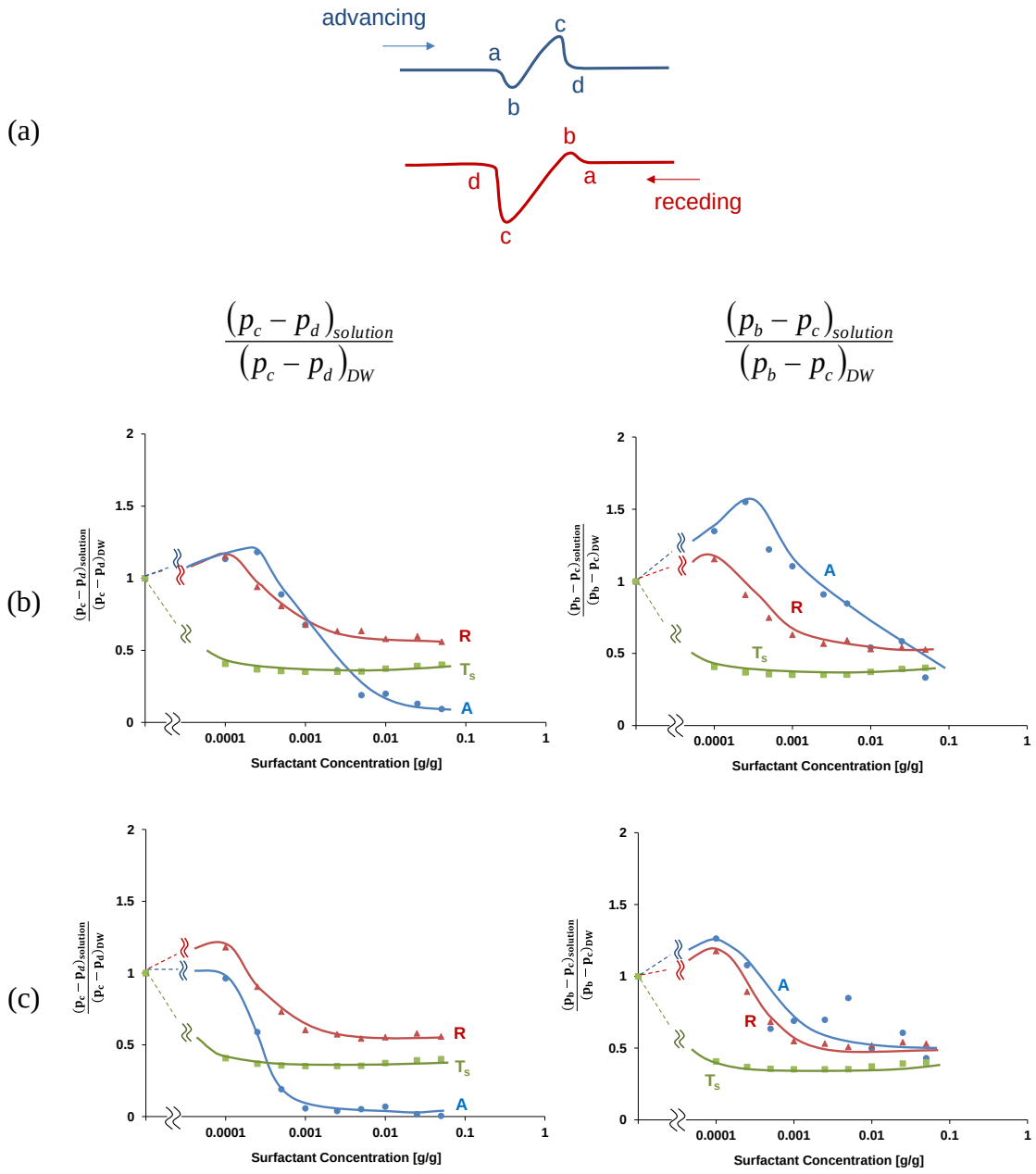

Figure 4.7 Measured pressure changes at the constriction (A: advance, R: recede, and T_s: surface tension): (a) pressure signatures during interface movement; (b) flow rate=20μL/hr; (c) flow rate=40 μL/hr; (d) flow rate=80 μL/hr; (e) flow rate=160 μL/hr.

(d)

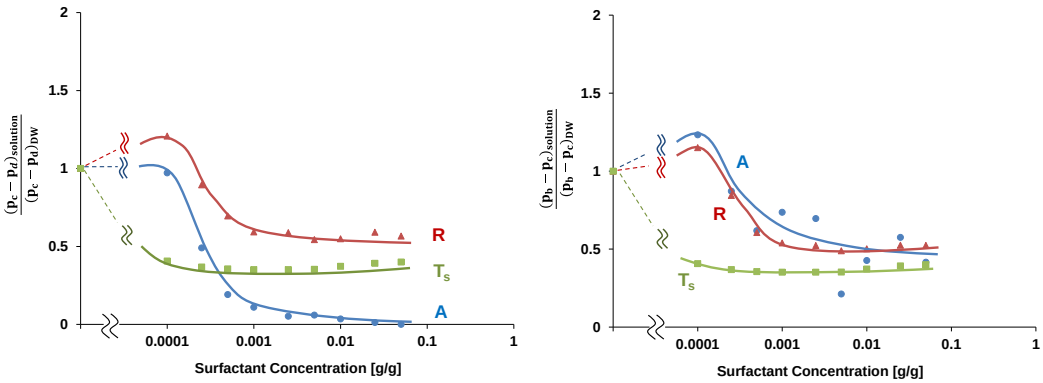

(e)

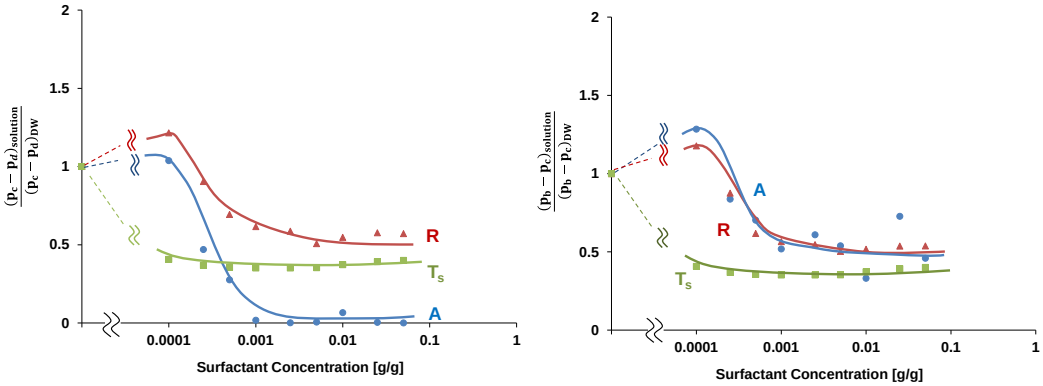

Figure 4.7 continued.

(a)

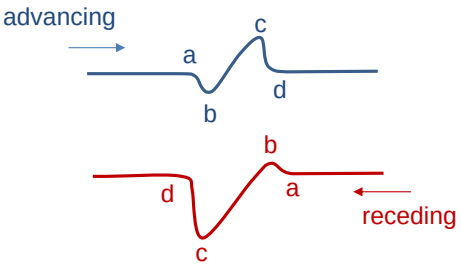

(b)

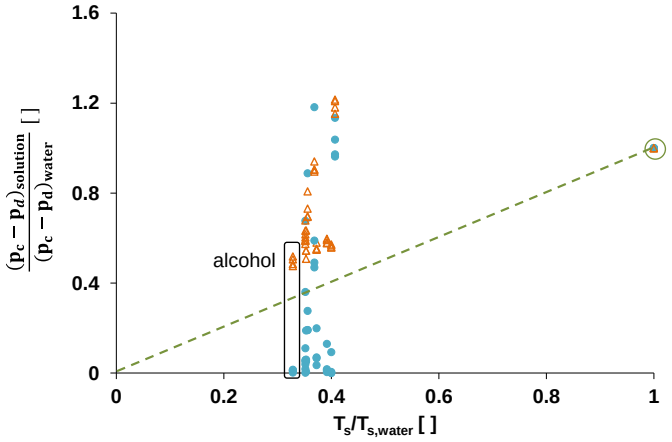

(c)

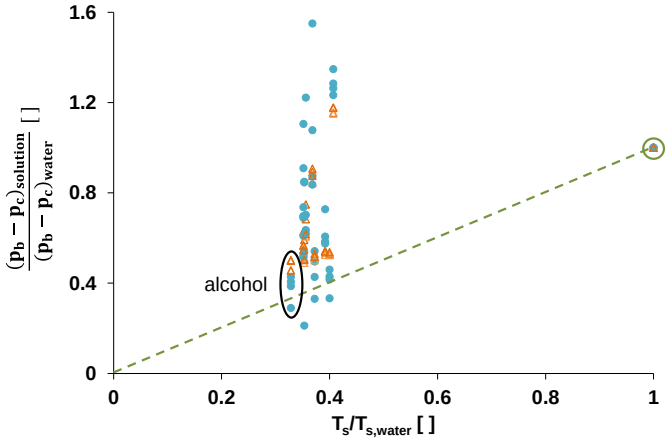

Figure 4.8 Measured pressure changes at the constriction versus $T_s/T_{s,water}$: (a) pressure signatures during interface movement, (b) pressure difference ratios of p_c-p_d with detergent solutions to that with deionized water and (c) pressure difference ratios of p_b-p_c with detergent solutions to that with deionized water.

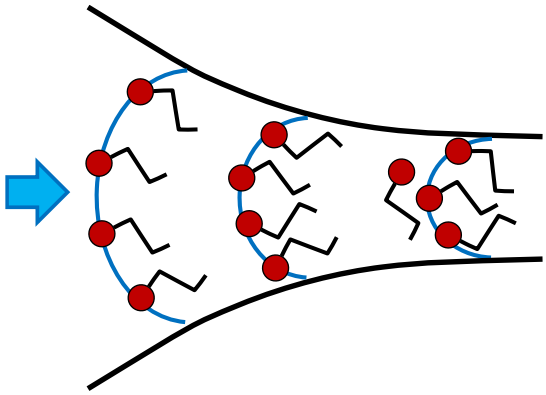

(a)

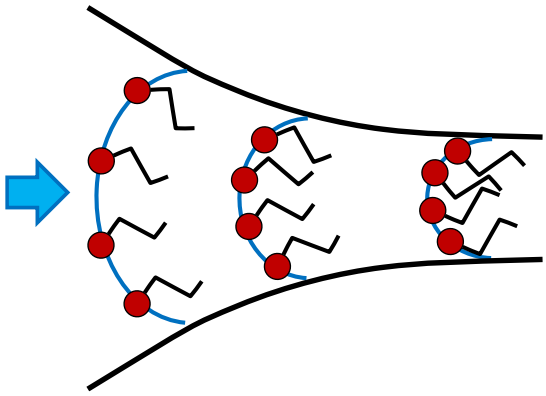

(b)

Figure 4.9 Surfactant self-regulation at the air-liquid interface: (a) desorption preserves surface concentration; (b) surface concentration increases at the constriction.

CHAPTER 5

GAS RECOVERY FROM FINE-GRAINED SEDIMENTS

5.1 Introduction

Hydrate-bearing sediments are found where pressure and temperature are within hydrate stability conditions and guest gas molecules are present. In “Class 1” hydrate-bearing sediment stratigraphy, the hydrate bearing sediment is confined by a cap rock above and a mixed water-gas saturated layer beneath; this stratigraphy is favorable for gas recovery [Moridis et al., 2003; Moridis et al., 2011].

Sandy hydrate bearing sediments are preferred because of potentially high hydrate saturation, high gas permeability, and low volumetric strain upon dissociation. Consequently, field tests for gas production have been conducted at sandy gas-hydrate sites in Mallik in Canada [Kurihara, et al.,2010], Mount Elbert in the United States [Moridis, et al., 2011], and the Nankai Trough in Japan [Yamamoto, 2013].

While clayey hydrate-bearing sediments contain most of the methane trapped in hydrates, gas recovery from clayey sediments is currently considered impractical [Moridis and Sloan, 2007; Boswell and Collett, 2011]. The purpose of this chapter is to explore possible bio-inspired gas production mechanisms in clayey hydrate-bearing sediments.

5.2 Gas Migration in Fine-Grained Soils – Underlying Concepts

5.2.1 Capillary Effects in Soils: Gas Invasion

The fluid pressure in a non-wetting fluid such as gas P_g must exceed the pressure in the wetting host fluid P_w in order to displace it. The threshold capillary pressure difference $P_c=P_g-P_w$ is the non-wetting fluid entry value or air entry value AEV [Brooks and Corey, 1964; Bear, 1972; Aubertin et al., 1998; Cho and Santamarina, 2001]. In general, capillary pressure P_c is a function of the surface tension T_s [N/m] and pore radius r_{throat} [m] (Laplace equation):

$$P_c = P_g - P_w = \frac{2T_s}{r_{throat}} \qquad [5.1]$$

The interfacial tension between carbon dioxide and water radius varies from T_s=0.065 N/m at 1 atm to T_s=0.025 N/m at 20 MPa [Espinoza and Santamrina, 2010; Hildenbrand et al., 2004]. Gas displaces water intermittently, from one pore throat to the next [Haines, 1930; Morrow, 1970]. Invasion momentarily stops until the gas pressure recovers.

5.2.2 Gas-Driven Fractures

The major particle forces under multi-phase fluid conditions are the capillary force F_c, the drag force F_d, and the skeletal force F_s:

$$F_c = \pi d_s T_s \qquad [5.2]$$

$$F_d = 3\pi\mu v d_s \qquad [5.3]$$

$$F_s = \sigma' d_s^2 \qquad [5.4]$$

where d_s [m] is the grain size, μ [Pa·s] the fluid viscosity, v [m/s] the flow velocity, and σ' [Pa] effective stress. Gas driven fractures emerge when the drag force or the capillary force opposes and prevails over the skeletal force [Shin and Santamarina, 2010]. Fractures in soils are highly permeable conduits and preferential gas passages [Horseman et al., 1999; Hildenbrand et al., 2002; Delahaye and Alonso, 2002]. A gas-driven fracture initiates when the breakthrough pressure P_c^* exceeds [Espinoza and Santamarina, 2010]:

$$P_c^* = \Psi \frac{S_s \rho \cos\theta}{e_{1kPa} - C_c \log \frac{p'}{1kPa}} \qquad [5.5]$$

where Ψ is a constant for fabric geometry (particle shape and pore size distribution), S_s [m^2/g] is the specific surface, ρ [kg/m^3] the density, e_{1kPa} the void ratio at σ'=1 kPa, C_c the compressibility, and σ' [Pa] the effective stress.

5.2.3 Analogical Concept: Gastrointestinal GI Tract

Gas in the GI Tract. Gases in the GI tract (N_2, CO_2, H_2, CH_4, and O_2) are generated by inhalation and bacterial fermentation [Levitt and Bond, 1980; Danzl, 1992]. The gas storage volume is limited [Serra et al., 1998]. Excess gas is either consumed (e.g., O_2) or eliminated from the GI tract through exhalation, diffusion and flatulence. A person discharges between 400 and 2,000 ml of gas per day [Levitt and Bond, 1980; Danzl, 1992].

Flatulence in the GI Tract. Peristaltic movement in the GI tract carries solids along the digestive systems [Sherman and Sherman, 1979; Weisbrodt, 1981; Schauf et al., 1990; Tortora and Grabowski, 2000; Germann and Stanfield, 2002; Boron and Boulpaep, 2009]. Non-concurrent gas and solid migration in the GI track suggests an alternative gas passage

independent of peristaltic motion, related to gas-swollen tract and the development of preferential flow paths [Gregersen and Christensen, 2000; Hansen, 2003; Gregersen, 2006; Tremolaterra et al., 2006]. A similar gas propagation strategy can be used to recover gas from clayey hydrate-bearing sediments.

5.3 Experimental Study

5.3.1 Experimental Procedure

Materials. Four soils were tested in this study Ottawa 20-30 sand (d_{50}=0.72 mm), F110 sand test-1 and test-2 (d_{50}=0.12 mm), silica flour (d_{50}=0.02 mm), ground calcium carbonate (d_{50}=0.009 mm), and kaolinite (d_{50}=0.00036 mm). For comparison, feces consists of ~10 μm particles [Stephen and Cummings, 1980]. The air entry value AEV was measured in each case using a rigid cylinder (Figure 5.1). Trends computed with Equation 5.1 are superimposed on the figure for loose and dense mono-size packings. Deviations from these trends (e.g., ground calcium carbonate) reflect the effect of non-uniform, non-spherical grains.

Analogical Experiments of Gas Propagation. Experiments were designed to simulate gas accumulation, pressure increase, tube expansion, and gas propagation in the GI tract. A latex tube (outside diameter OD=22mm; inside diameter ID=19mm) was selected to model an expanding boundary; the measured compliance is 0.5mL/kPa and the measured Young's modulus E is 1,340 kPa (Figure 5.2); for comparison, the rectal wall

compliance is 75 ml/kPa [Prior et al., 1990; Bharucha et al., 2006]. The tube was filled with fully water-saturated soils and impervious solids (plastic spheres or rods).

Tests were conducted by forcing air flow in the horizontal, upward and downward directions and controlling the pressure gradient (Figure 5.3). A pressure transducer PT measured changes in inlet pressure versus time.

5.3.2 Results

Flexible Tube with Impervious and Rigid Fill. Air cannot break through the rigid and solid acrylic fill and must flow between the latex tube wall and the solid fill. Figure 5.4 shows the evolution of inlet pressure [Harrington and Horseman, 1999; Horseman et al., 1999; Hildenbrand et al., 2002; Olivella and Alonso, 2008]:

- Threshold pressure at the beginning of gas invasion
- Breakthrough pressure at the end of the propagation in the sediment
- Steady state leak pressure during constant gas flow
- Shut-off pressure after stopping gas injection

Fluid passages generated between the rod and the tube are preserved under constant inlet flow. Residual water can imbibe into drained pores and cause cycles in the evolution of inlet pressure (Figure 5.4b). The pressure-time signature for the latex tube with spherical solid inclusions shows a pressure drop as the fluid advances past each sphere (Figures 5.4c and 4d): injected air spreads into the expanded gap between solid spheres and the latex tube, and the air pressure drops rapidly.

Flexible Tube Filled with Soil. The inlet pressure P_{in} versus time signatures measured with different sediments and at different orientation are summarized in Figure 5.5. Time is normalized with respect to the breakthrough time in each case.

Horizontal Direction. The signature gathered with Ottawa 20-30 sand shows stable displacement at a pressure similar to the AEV (Figures 5.5a and 5.1a). Hydrostatic pressure is negligible. The drag resistance decreases as the front advances, so the inlet pressure decreases as well. When the fill was either F110 sand or F110 sand with fines, similar pressure-time trends are obtained with the maximum pressure being the corresponding AEV. When the air injection rate increased to 2 ml/s by a peristaltic pump, the drag resistance increased, and high inlet pressure caused the latex tube to swell and soil particles to migrate (Figure 5.6).

Downward Direction. Inlet pressure versus time signatures are presented in Figure 5.4b. The inlet pressure exceeds drag resistance and the AEV (Note: the hydrostatic pressure at the bottom is 9 kPa). Ottawa sand 20-30 experienced stable displacement through the sand along the tube. The breakthrough pressure of F110 sand test-2 was 20 kPa followed by a pressure drop towards the same P_{in}-t signature for F110 sand test-1.

Upward Direction. Figure 5.5c shows the increase in inlet pressure until breakthrough and shutoff. After the collapse of air passages in the three soils, inlet pressure was rebuilt. The latex tube deformed both radially and vertically in response to the invading gas. The inlet pressure gradually increased until the gas passed the sediment. Air trapped between soil fractions formed a gap at the top of the sediment (F110 sand test-1 and F110 sand test-2). Air propagated when the inlet pressure led to the collapse of the upper

segment. Gas propagation between the tube wall and the sediment could have induced the collapse.

5.4 Analyses

Preferential Flow Along the Soil-Boundary Wall. The elastic thin-walled flexible latex tube experiences elastic expansion in the radial and axial directions in the small strain range [Kyriakides and Chang, 1990; Kyriakides and Chang, 1991]. The initial tube diameter D_{tube} can expand under internal pressure to form a gap δ between the tube and the rigid fill. The radial strain is:

$$\varepsilon_r = \frac{2\delta}{D_{tube}} \qquad [5.6]$$

A gap forms when the internal pressure P_{in} exceeds the external pressure P_{ext}. The gap thickness δ will be:

$$\delta = \frac{P_{in} - P_{ext}}{E_0} \frac{D_{tube}}{2} \qquad [5.7]$$

where E_0 is the elastic modulus. In the tests with the latex tube, hoop stress may develop by stretching the latex tube with the fill to cause ε_r rather than by external pressure. In this case, the equivalent external pressure is

$$P_{ext}^{*} = \varepsilon_r E_0 \qquad [5.8]$$

Preferential flow takes place along the gap rather than through the sediment when the gap opening exceeds the pore throat size d_{th} that defines the air entry pressure AEV:

$$d_{th} = \frac{4T_s}{AEV} \qquad [5.9]$$

Therefore, boundary flow occurs when:

$$\frac{\delta}{d_{th}} > 1 = \frac{\frac{P_{in} - P_{ext}}{E_0}\frac{D_{tube}}{2}}{\frac{4T_s}{AEV}} \qquad [5.10]$$

Figure 5.7 predicts gas passage regimes whereby gas can flow through pores or fluid-driven fractures. The effective stress in Figure 5.7 (b) is the $p_{in} - p_{ext}$ when AEV= $p_{in} - p_{ext}$ and $\delta/d_{th}=1$ in Equation 5.10. According to this analysis, gas propagation takes place when gas pressure is greater than either the capillary pressure (AEV) or the effective stress (confining stress). Although the capillary pressure is low, fast air invasion will cause drag resistance, increased inlet pressure and gas may form a gap between the sediment and the tube wall. Air propagation along the fill-wall interface is controlled by the confining stress or elastic boundary expansion, drag and capillary forces and resembles gas-driven fractures [Shin and Santamarina, 2010].

Gas Flow Along the Gap. Inlet pressure during gas propagation can be estimated (Figure 5.5):

$$P = \frac{2T_s}{\delta} + \frac{12\mu_{air}u_{avg}x}{\delta^2} + P_w \qquad [5.11]$$

where u_{avg} [m/s] is the average air velocity, μ_{air} [Pa·s] the viscosity of air, P_w [Pa] hydrostatic pressure, an x [m] the total length of air propagation. The capillary term vanishes after a gas passage is formed.

5.5 Discussion – Paradigm Shift in Gas Recovery

Gas propagation in sediments is affected by the hydrostatic pressure, the drag effect, and the AEV. In general, gas propagation in fine sediments requires high gas pressure to overcome the AEV due to the small pore size. Experiments in this chapter show the possibility of gas propagation along a gap that forms as an opening mode discontinuity along interfaces; in this case, gas pressure during hydrate dissociation increases until it reaches the confining stress when the opening mode discontinuity develops. The proposed mechanism can facilitate gas recovery from fine-grained hydrate bearing sediments.

5.6 Conclusions

Gas recovery from fine-grained hydrate-bearing sediments has received little attention due to inherent gas flow restriction in fine-grained sediments. This study highlights alternatives for gas production through preferential gas passages that form in fine-grained sediments. Experimental results show the following:

- Gas passage depends on flow rate, fill characteristics, and boundary compliance.
- Gas pressure increases until it reaches the AEV and migrates through pores, or the pressure produces gas-driven openings.
- Sediments deformation affects the pressure for gas propagation.
- Pressure cycles including buildup, breakthrough, steady state leak, and shut-off should be expected during production.

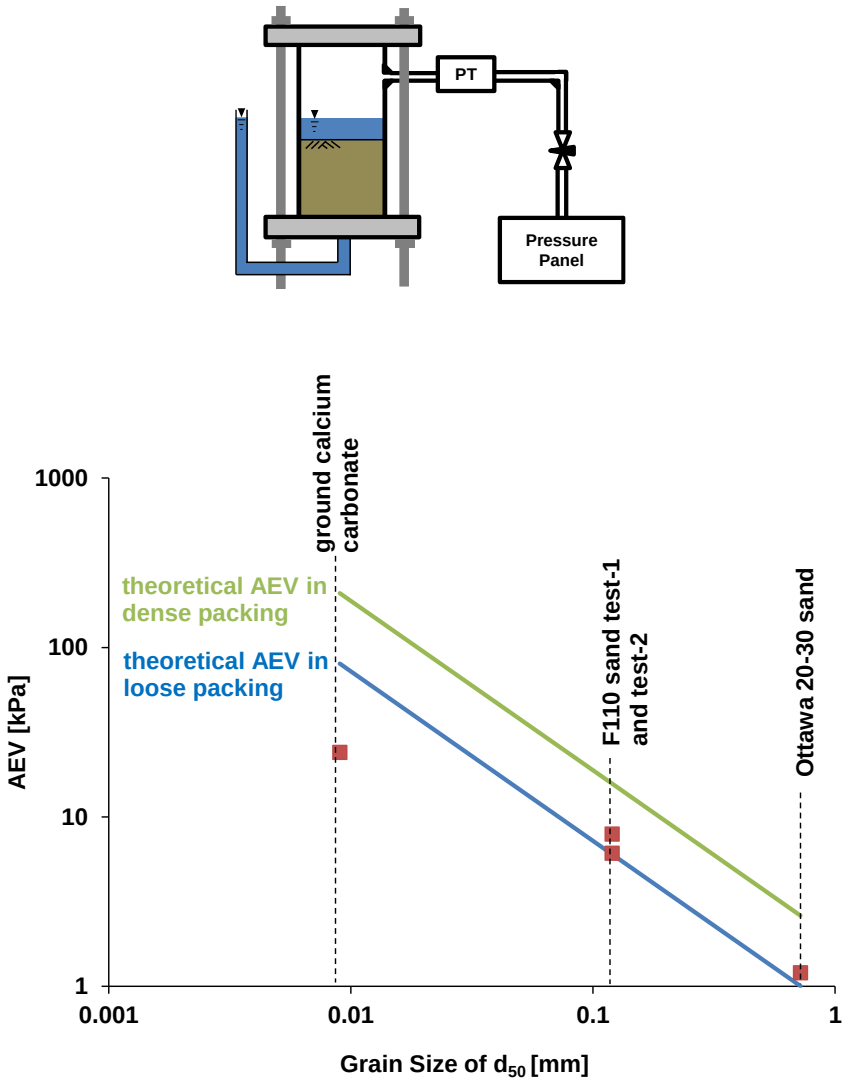

Figure 5.1 Air entry values for the tested sediments.

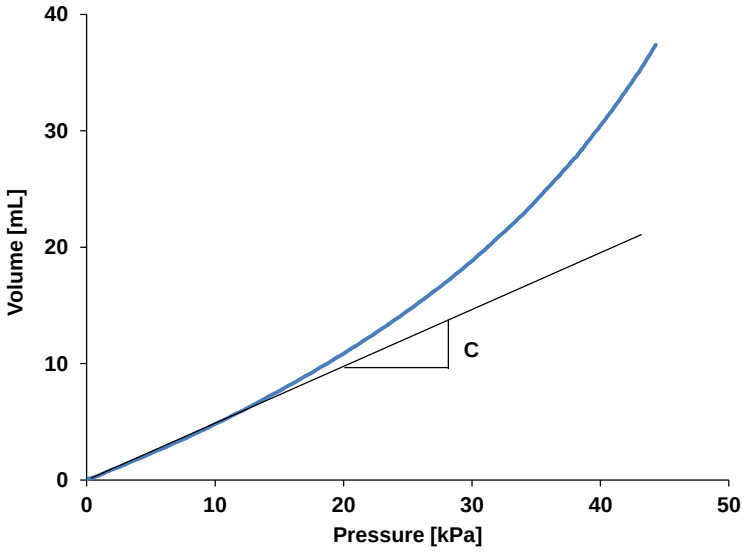

(a)

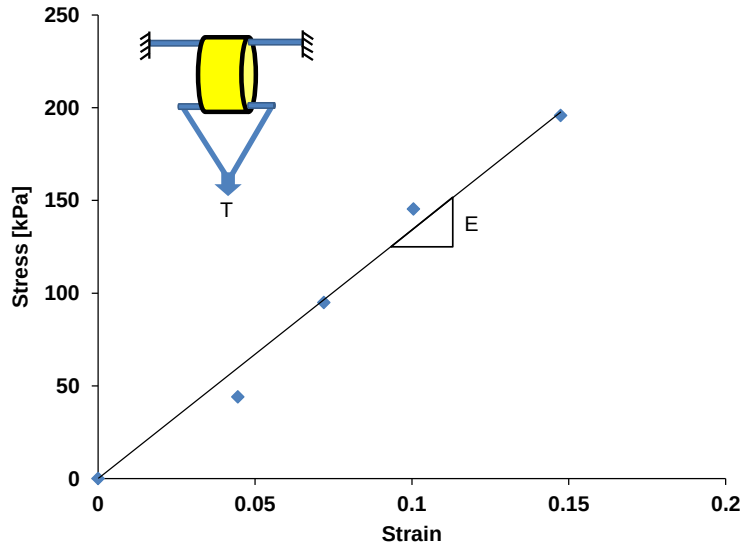

(b)

Figure 5.2 Elastic moduli of the latex tube: (a) compliance and (b) Young's modulus.

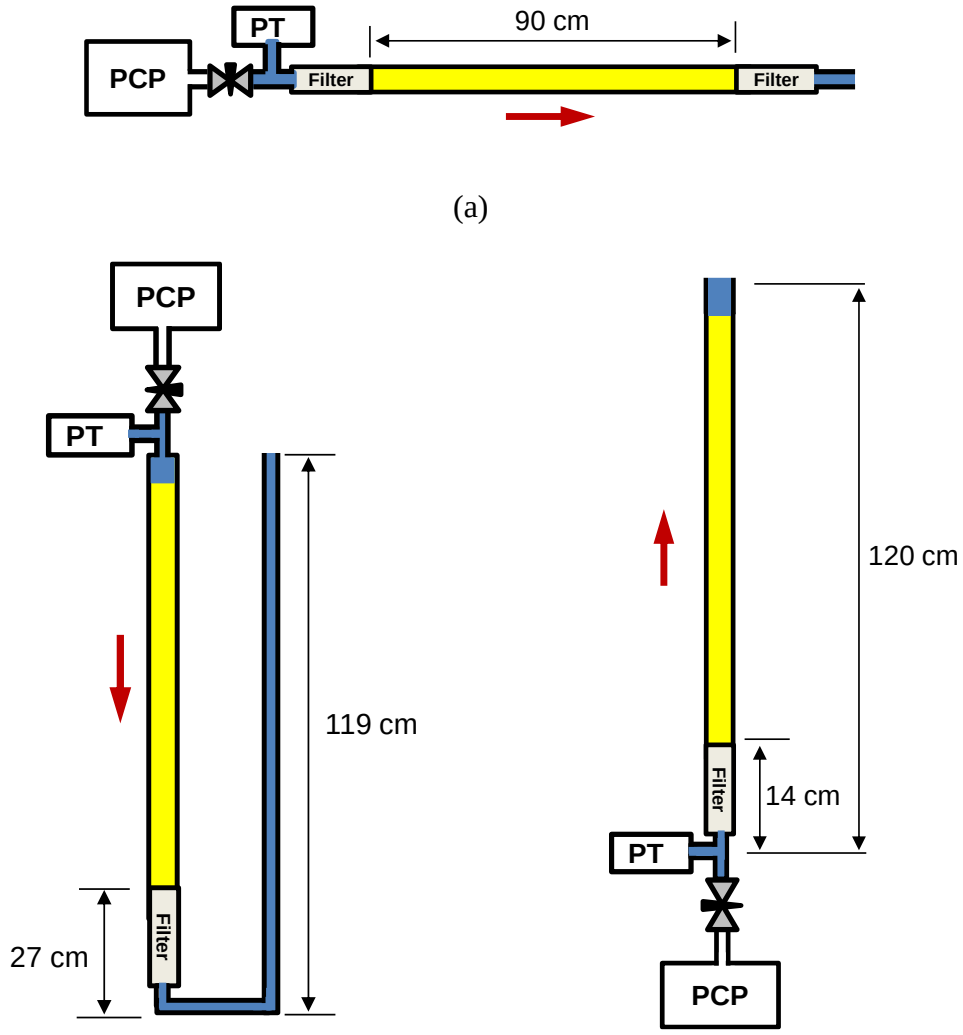

Figure 5.3 Experimental configuration for gas migration tests in latex tubes filled with sediments: (a) horizontal direction, (b) downward direction and (c) vertical upward direction.

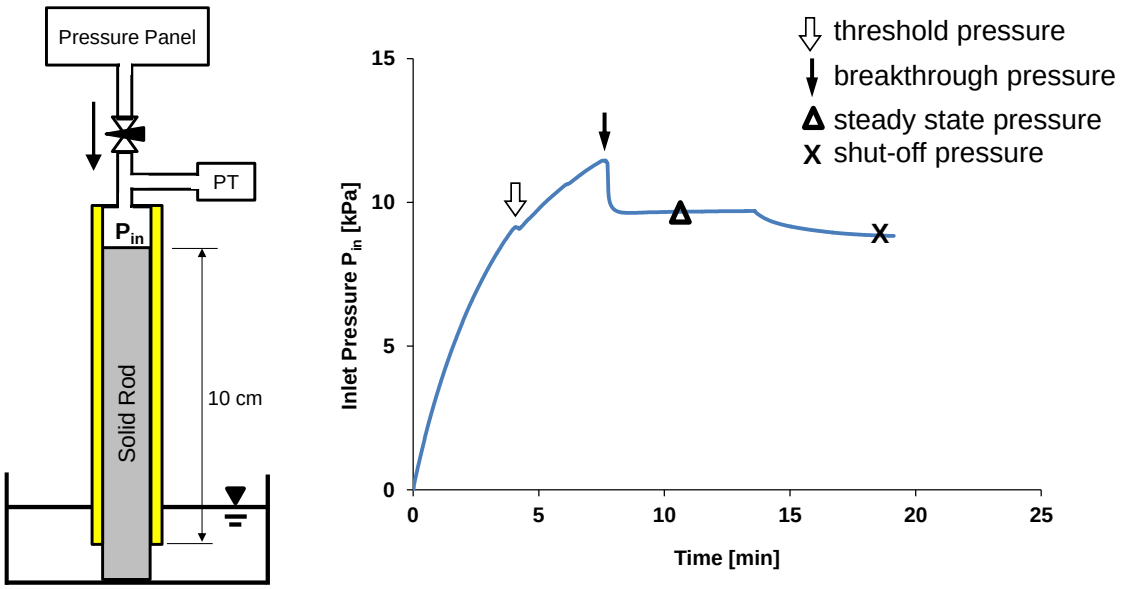

(a)

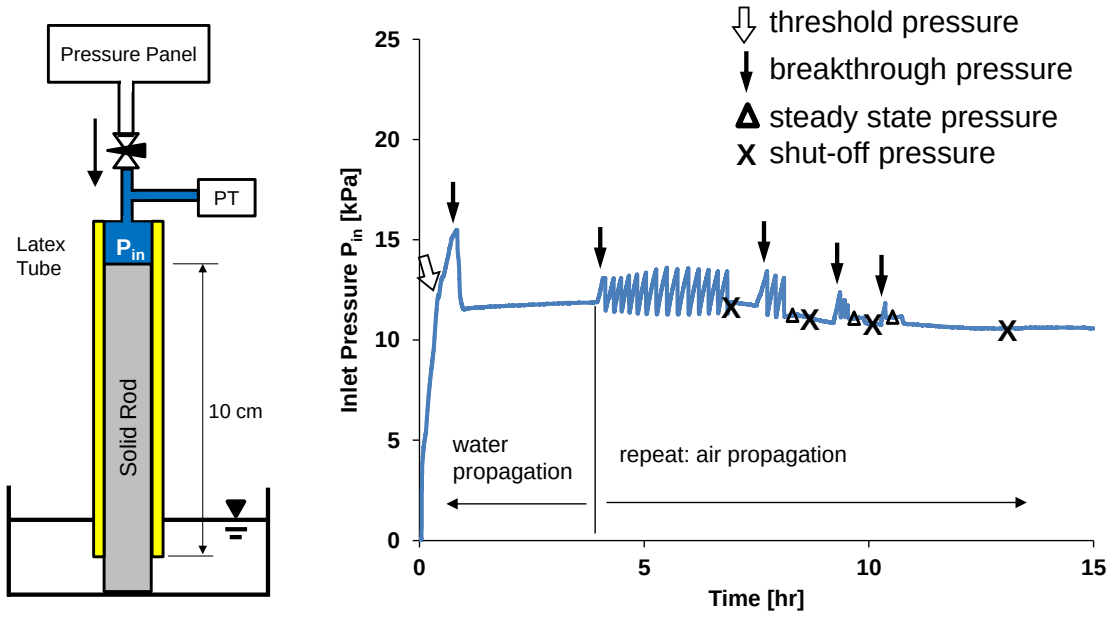

(b)

Figure 5.4 Inlet pressure versus time measured using the latex tube filled with impermeable rigid fill: (a) rod and air, (b) rod and water, (c) spheres and air and (d) spheres and water.

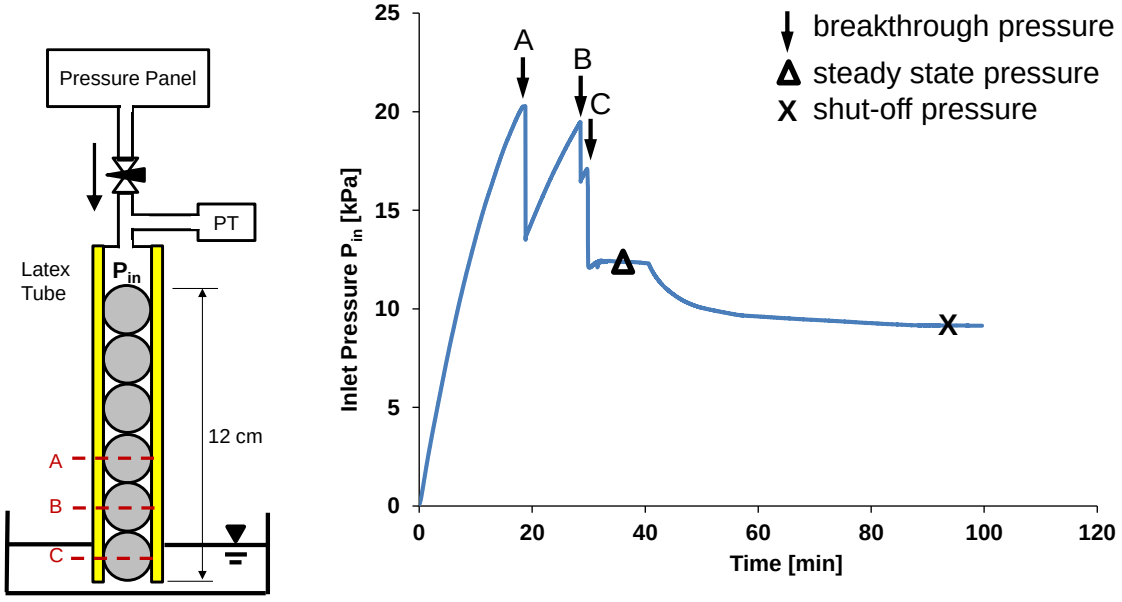

(c)

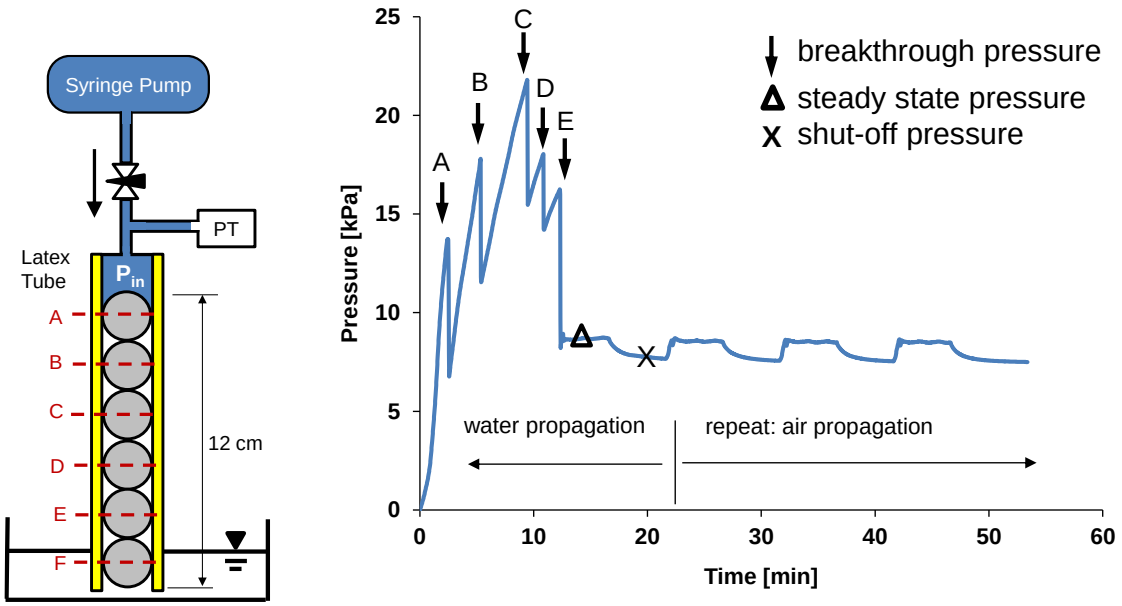

(d)

Figure 5.4 continued

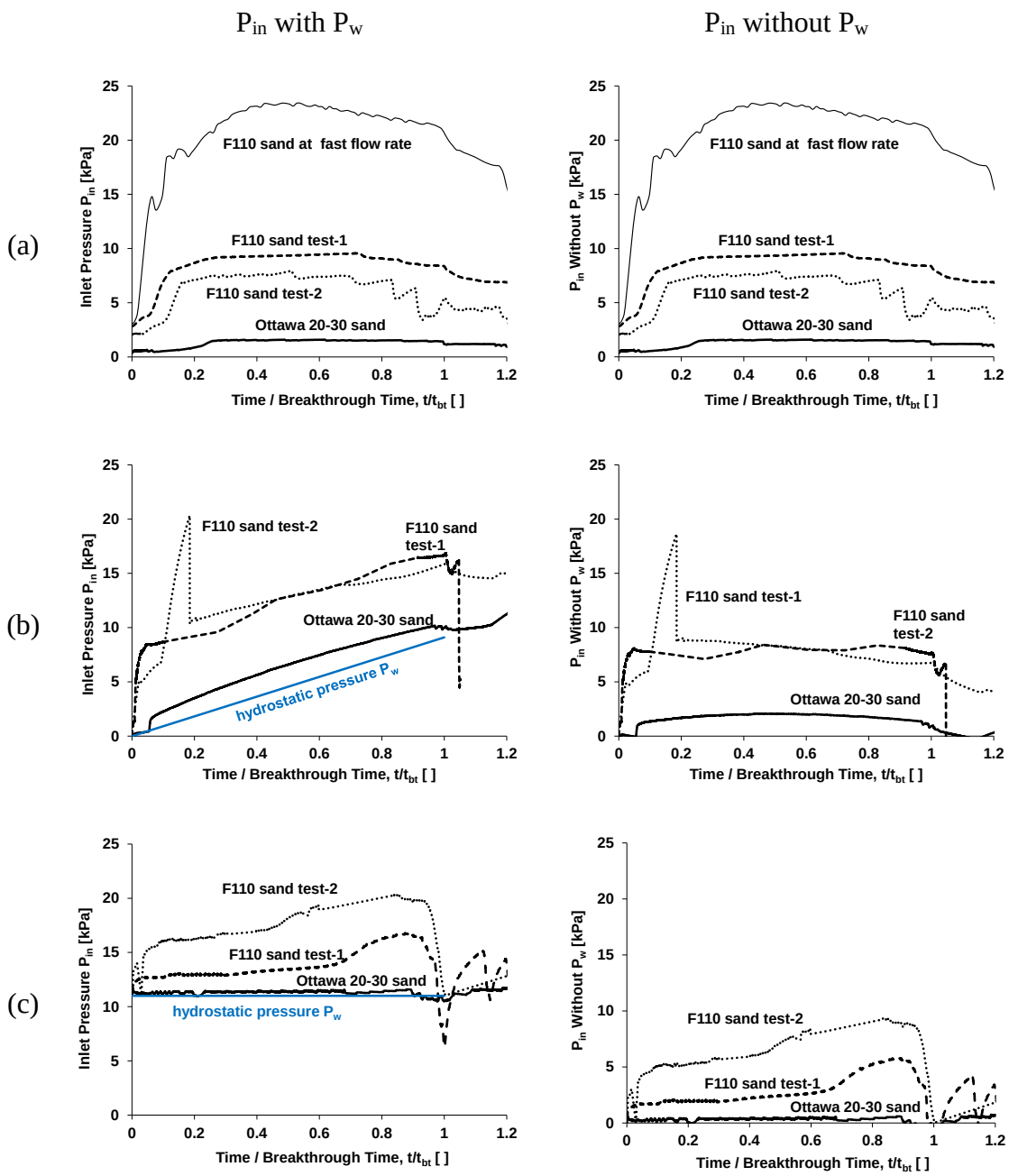

Figure 5.5 Experiment results for air propagation in soil-filled tubes: (a) horizontal direction, (b) downward direction and (c) upward direction.

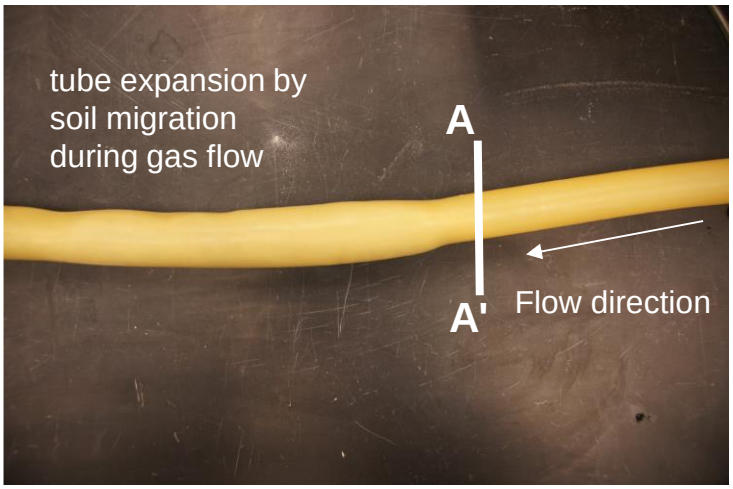

Figure 5.6 Sediment deformation and displacement in the latex tube during gas pressurization. The evolving tube geometry depends on flow directions (horizontal, upwards or downwards) and affects pressure signatures.

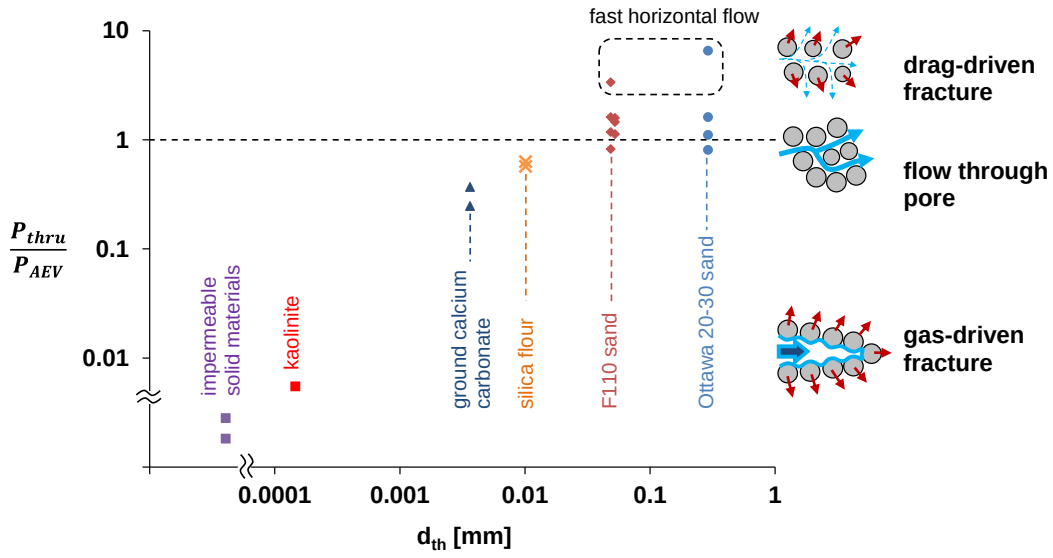

(a)

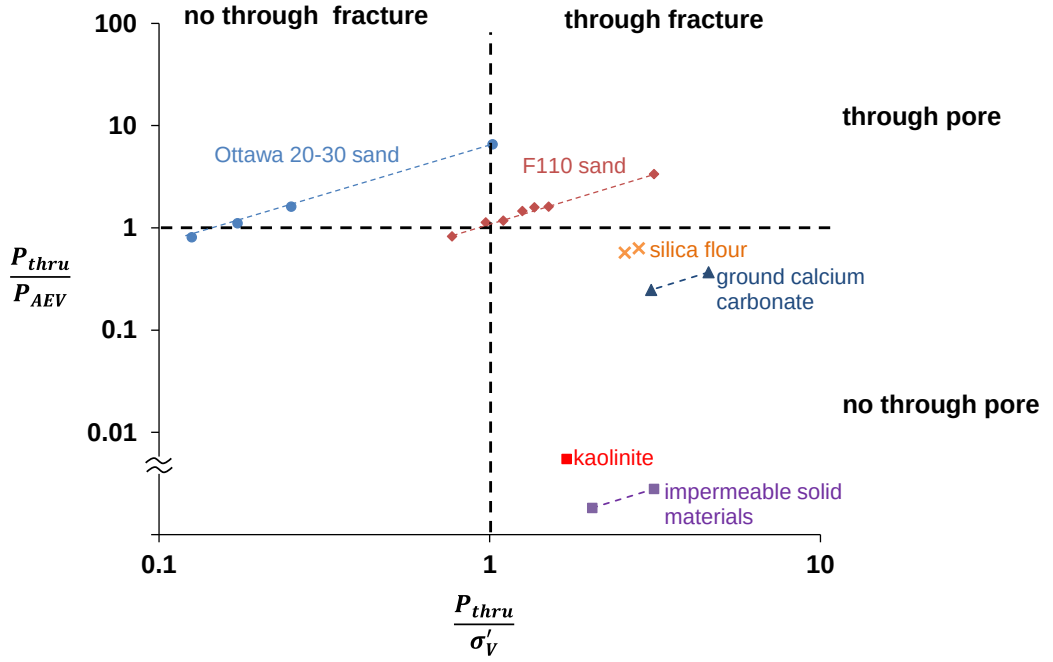

(b)

Figure 5.7 Preferential gas passage – different regimes defined by (a) the ratio of breakthrough pressure to the air entry value versus pore throat sizes and (b) the ratio of breakthrough pressure to the effective vertical stress.

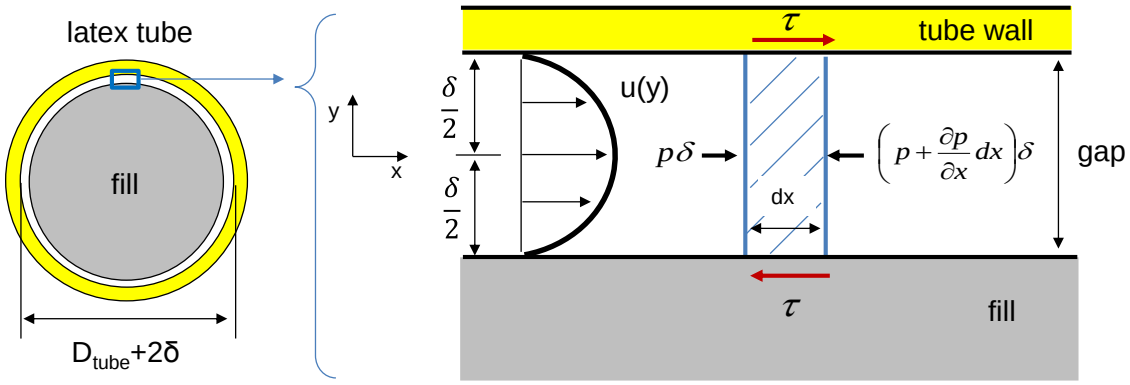

Figure 5.8 Gas flow along the gap between the wall and the solid rod.

CHAPTER 6

PRESSURE CORE CHARACTERIZATION TOOLS FOR HYDRATE-BEARING SEDIMENTS

The author was primarily involved in designing the controlled depressurization chamber and the sub-sampling tool for bio-studies; all tools were developed in collaboration with S. Dai and M. Terzariol. This chapter documents this collective effort, and it published as a shorter version in Santamarina et al., 2012.

6.1 Introduction

Natural gas hydrates form at high fluid pressure and low temperature, where biogenic and/or thermogenic gases are available. These requirements delimit the distribution of hydrate-bearing sediments to sub-permafrost, deep lakes (theoretical water depth greater than ~390 m), or ocean sediments (theoretical water depth greater than ~320m). Typically, hydrates are found in deeper water columns due to thermal fluctuations and diffusion near the sediment surface [Xu and Ruppel, 1999].

The clathrate or cage-like structure formed by water molecules hinders the repulsion between gas molecules and allows for high gas concentration. There is one molecule of methane every 5.75 molecules of water in CH_4-hydrate, compared to the solubility of methane in water which is in the order of 1-in-750. With such a high methane concentration, natural gas hydrates can become an energy resource but they are a potential source for potent green-house gases as well.

Depressurization and/or heating across the phase boundary causes hydrate dissociation. The hydrate volume expands multiple times just to cross the phase boundary. For example, there is a 1.3 times expansion under Blake Ridge pressure-temperature P-T conditions, and a 4 times expansion in the shallower Hydrate Ridge formation. Rapid volume expansion brings the sediment to failure in low permeability formations, triggering wellbore and even large scale seafloor instabilities.

Dissociation, volume expansion, and the ensuing sediment destructuration dramatically affect the ability to characterize hydrate-bearing sediments. Indeed, proper characterization requires coring, recovery, manipulation and testing under P-T conditions within the stability field. Pressure core technology has been advanced to address this need.

6.2 Pressure Core Technology: Overview

6.2.1 Coring and Recovery

The development of pressure coring and recovery tools have involved research teams around the world, including initiatives such as the International Ocean Drilling Program and the European Union's Marine Science and Technology Program [Kvenvolden et al., 1983; Pettigrew, 1992; Amann et al., 1997; Dickens et al., 2003; Qin et al., 2005; Schultheiss et al., 2009]. Push-piston (clay bearing sediments) and rotary coring (sands with high hydrate saturation) methods have been developed to gather several meter long pressure cores. The core slides inside a plastic liner during coring to facilitate its manipulation after recovery. The in situ fluid pressure is maintained by a ball valve that closes the barrel beyond the core-catcher; the ball valve seal is critical to reliable pressure

core recovery. While temperature control is also possible (PTCS - Kawasaki et al., 2006), analytical and field results show that the additional complexity of temperature control is unnecessary as long as the barrel is rapidly cooled once it reaches the surface.

6.2.2 Manipulation

Earlier studies using pressure cores required fast depressurization and stabilization in liquid nitrogen before transferring the core into testing chambers. Such drastic changes in pressure and temperature can be prevented if all operations after recovery are conducted under P-T conditions within the stability field to prevent dissociation. Pressure core manipulation and transfer technology requires a longitudinal positioner/manipulator and ball valves to couple components at equalized pressures (Pressure Core Analysis and Transfer System PCATS - Schultheiss et al., 2006).

6.2.3 Testing and Characterization

Testing and characterization tools were developed in parallel to manipulation capabilities. *Non-contact* characterization tools are based on gamma density, X-rays and water-coupled P-waves (Pressure Multi-Sensor Core Logger -Schultheiss et al., 2006; see also Abegg et al., 2008). *Contact/invasive* tools allow for the assessment of stiffness using P-and S- wave velocities, strength, electrical resistivity profiles and internal core temperature (IPTC - Yun et al., 2006); contact measurements require pre-drilling the plastic liner under pressure at the locations where measurements will be conducted. *Subsampling* capabilities have also been developed for biological studies under in situ P-T conditions (DeepIsoBug - Parkes et al., 2009).

6.2.4 Current Situation

Other characterization needs have gradually surfaced driven by the enhanced understanding of hydrate bearing sediments, the renewed interest in gas production and related engineering tasks, and the increased reliability of pressure core recovery. Pressure core characterization tools developed at the Georgia Institute of Technology are described next.

6.3 GT Pressure Core Characterization Tools (PCCTs)

Our pressure core characterization system includes both core manipulation tools and characterization chambers. Tools have been selected to obtain complementary information relevant to science and engineering needs, with emphasis on the measurement of parameters used in hydro-thermo-mechanical analyses.

All tools are designed following key guidelines and objectives: simple and robust systems, portable components for fast deployment, modular design for maximum flexibility, standard dimensions and parts for economic construction and maintenance, rust-resistance for seawater environment (all devices are made of stainless steel 316), can hold 35 MPa fluid pressure and operate at 21 MPa, capable to impose effective stress when physical parameters are effective stress dependent, and safe for the monitoring of hydrate dissociation and gas production during controlled depressurization, heating or fluid exchange (such as with liquid CO_2). The modular design implies geometrically compatible chambers and components developed with the same design philosophy; in particular, any two tools/chambers can be readily coupled through an identical flange-clamp system.

6.3.1 Manipulator (MAN)

The manipulator is a longitudinal positioning system that is used to grab and move the core along the interconnected chambers and valves as needed, always under the required P-T conditions. Figure 6.1 shows the typical operation sequence used to retrieve a specimen from the storage chamber into the manipulator followed by displacing core into a generic test chamber. The geometric analysis of the operation shown in Figure 6.1 reveals that the length of the manipulator L_{man} (with its "temporary storage chamber") is proportional to the length of the core L_{core} to be manipulated, $L_{man} \approx 3.5 \cdot L_{core}$. If an external positioning system is used, the rod must undertake the force due to the fluid pressure and the force required to displace the core; such a design is typically limited by buckling even when an open ended hollow tube is selected. Our system is designed to handle L_{core} = 1.2 m long cores, uses an internal telescopic screw system (stroke = 2.6m) driven by an external stepper motor, and can position the specimen with sub-milimetric resolution. It is coupled to the 1.3m long temporary storage chamber by means of a dismountable flange-clamp connection. A see-through port is included to confirm the position of the manipulator at any time.

6.3.2 Sub-Sampling (CUT)

The 1.2m long core can be cut into short specimens. Our cutting tool CUT houses either a linear or a ring-shaped saw-blade within a clamp-type chamber. The saw-based cutting ensures clean surfaces and minimizes specimen disturbance. The cutting tool CUT is mounted in series between the manipulator and any other test or storage chamber as needed (Figure 1e).

6.3.3 Instrumented Pressure Testing Chamber (IPTC)

The chamber was developed to measure P&S wave velocities, undrained strength, electrical conductivity, internal core temperature, and to sample fluids (Figure 6.2A - details in Yun et al., 2006). This cylindrically-shaped chamber has two sets of four diametrically opposite port pairs. The first pair drills holes (ID = 8mm) in the plastic liner so that contact probes in successive ports can be pushed into the specimen. In characterization mode, the IPTC is coupled to the manipulator on one side and an extension chamber on the other end, and measurements can be conducted at any position along the core length. The eight access ports make the IPTC a versatile chamber for conducting well-monitored production studies in view of reservoir calibration models.

6.3.4 Effective Stress Chamber (ESC)

Pressure cores are recovered and stored at fluid pressure and temperature P-T conditions needed to preserve hydrate. However, physical properties such as stiffness and shear strength are a function of both hydrate saturation and effective stress (Note: the relative relevance of effective stress increases as hydrate saturation decreases).

The effective stress chamber ESC maintains P-T stability conditions and restores the effective stress σ' that the sediment sustains in situ (Figure 6.2b). It was designed and laboratory-tested at Georgia Tech in 2006 under Joint *Oceanographic* Institutions JOI sponsorship, and it was first deployed in the field by the Korean Institute of Geoscience & Mineral Resource KIGAM in collaboration with Geotek during the UBGH1 expedition (Lee et al., 2009).

The original design was based on a zero-lateral strain boundary condition. We have updated this chamber to accommodate a stress-controlled boundary condition using a jacket (Figure 6.3). The resulting triaxial stress configuration consists of σ_3' applied with the jacket and σ_1' applied by a piston that is advanced through the ball valve and acts directly onto the pressure core. The piston and the base pedestal house the sensors needed for the measurements of physical properties, including stiffness (wave velocities), thermal conductivity, and electrical resistivity.

A salient advantage of the flexible wall configuration is the ability to conduct precise fluid conductivity measurements by preventing the preferential flow along the sediment-steel boundaries in rigid-wall chambers. This chamber is particularly well suited to monitor production studies under in situ effective stress conditions, including the assessment of sediment volume change upon dissociation.

6.3.5 Direct Shear Chamber (DSC)

The shear strength of hydrate-bearing sediments under in situ pressure, temperature and effective stress conditions is a necessary parameter for constitutive models.

Two constraints guided the design of the DSC tool. First, the imperfect boundaries that result when cutting heterogeneous cores under pressure cause stress concentration during vertical loading; thus, we selected a "double direct shear" geometry to cut across the specimen away from end effects. Second, overcutting during coring leaves a gap and the core tends to tilt during shear; then, we adopted a double shear plane configuration to avoid bending action. Consequently, the direct shear chamber consists of a thick wall stainless steel ring that is pushed to shear the central third of the specimen (Figure 6.2c).

The DSC includes the piston to restore effective stress (self-reacting vertical frame - similar to the ESC), a liner trap to capture the plastic liner before the specimen enters the shear chamber, and a small lateral built-in frame to push the side piston that displaces the ring (Figure 6.2c). The maximum shear displacement is δ_{max} = 15mm so that both peak and residual shear strengths can be determined.

The test sequence includes: (1) shear under in situ vertical effective stress and P-T conditions, (2) push the ring back to its original position, (3) monitor hydrate dissociation and gas production at constant vertical effective stress and zero-lateral strain boundary conditions, and (4) shear the specimen again to determine the hydrate-free residual shear strength. The complete data set provides strength and volume change data under in situ conditions that are necessary for model calibration, production design and stability analyses.

6.3.6 Sub-Sampling Tool for Bio-Studies (BIO)

The study of bioactivity in deep-water sediments without incurring in de-pressurization cycles is crucial to the survival of some barophilic microorganisms. The BIO chamber is loaded with a core segment using the manipulator; afterwards, it is detached from the manipulator for all successive procedures (Figure 6.2d). Its operation involves (1) nitrogen-liquid replacement, (2) core face cleaning and chamber fluid-based sterilization, (3) sub-sampling using a rotary sampling head, and (4) sample release into the bio-reactor that is pre-filled with nurturing solutions (volume = 10 cc). All operations can be observed through a sapphire window. Bio-reactors are readily replaced by closing a system of two ball valves and decoupling the quick connect fitting in between. This device allows the

collection of a large number of specimens from a single core segment under in situ hydrostatic pressure.

6.3.7 Controlled Depressurization Chamber (CDC)

Successful pressure coring operations may produce more pressure cores than the available storage. In this case, recovered cores are selectively de-pressurized to conduct further studies under atmospheric pressure. The controlled depressurization chamber is designed to help preserve the core lithology and to gain valuable information during depressurization, with minimal demand on personnel resources. This stand-alone device has a built-in drilling station to perforate the liner at selected locations in order to reduce the specimen longitudinal expansion. A pressure transducer and a thermocouple monitor the gas P&T conditions inside the chamber. In addition, three self-drilling thermocouples are built-in along the CDC; these are driven into the core to monitor the internal sediment temperature during depressurization. Finally, a 2L water trap and a 55L gas trap are attached in series to the needle valve that controls the rate of depressurization; these traps sit on scales to monitor produced water and gas (Figure 6.2e).

6.4 Measurement of Physical Properties: Sensors and Gadgets

Multiple sensing systems have been developed to characterize the sediment and to determine hydro, thermo, chemo, bio, and mechanical parameters within the chambers, under controlled pressure, temperature, and effective stress conditions as described above. Not all sensors or gadgets are available for all chambers, yet, their deployment in various

devices support the comprehensive characterization of natural hydrate-bearing sediments under in situ pressure, temperature, and/or stress conditions, and permit detailed monitoring of gas production tests.

6.4.1 Tool Position Control

All contact instruments, sensors and drills are mounted on polished rods (diameter d=7.9mm) which are advanced into the specimen using externally controlled screw-based positioning systems to overcome the 1.7 kN force at the maximum working fluid pressure of 35 MPa (Figure 6.4). The hand-operated driver advances along the threaded guide while pushing the tool rod. The ball valve between the threaded guide and the chamber permits replacing tools under pressure (Figure 6.4).

6.4.2 Sensors

Transducers are mounted at the tip of tool rods and wired through the central bore. Available instruments are shown in Figure 6.5 Small-strain wave velocity measurements employ bender elements for S-waves and pinducers for P-waves (Figures 6.5a&6.5b – peripheral electronics and test procedures as described in Lee and Santamarina, 2005a; Lee and Santamarina, 2005b).

While large-strain strength data can be gathered using the direct shear chamber (DSC – Figure 6.2c), we have developed a strength-penetration probe as well (Figure 6.5c). This device determines the sediment strength using a cone-shaped stud equipped with a full-bridge strain gauge inside. The measured tip resistance during probe penetration reflects the sediment undrained shear strength (details in Yun et al., 2006).

Fluid conductivity can be determined using the flexible wall system built within the effective stress chamber ESC (Figure 6.2b & 6.3), and inferred using the fluid sampling tool (Figure 6.5d). This is a self-drilling drainage port with a pressure or volume control flow condition to drive the interstitial fluids out of hydrate-bearing sediment. The pressure difference can be selected to preserve hydrates within stability conditions.

Electrical resistivity is measured using an electrical needle probe that is gradually inserted into the specimen to determine a radial resistivity profile with millimeter-scale spatial resolution (Figure 6.5e – details and measurement procedure in Cho et al., 2004). We have also developed a multiple electrode system at the base of the effective stress cell that allows us to conduct a surface-based electrical resistivity tomography within a specimen.

The thermal probe consists of a thermocouple deployed at the tip of a tool rod. When pushed into the sediment, the thermal probe monitors the temperature inside the core (Figure 6.5f). The self-drilling version of this probe, deployed in the controlled depressurization chamber CDC, places the thermocouple inside a hollow drill tip at the end of a tool rod. Internal temperature measurements can be used to monitor phase transitions during controlled gas production studies and to determine thermal conductivity (by inversion for given imposed boundary conditions). In addition, the TPS sensor for thermal conductivity measurements developed at NETL (Figure 6.5g, Rosenbaum et al., 2007) can be installed at the tip of tools or on the pedestal of the effective stress and direct shear chambers.

6.5 Monitoring Dissociation – Gas Production

All PCCTs chambers allow core-scale gas production tests by either de-pressurization, heating, or chemical injection (e.g., inhibitors or carbon dioxide). Monitoring data include pressure, temperature, produced gas and water, stiffness (seismic wave velocities), fluid conductivity, and electrical resistivity. Figure 6.6 shows examples of data gathered during the depressurization of natural hydrate-bearing sediments.

6.6 Discussion: Comprehensive Characterization Approach

Pressure coring, recovery, and testing prevent hydrate dissociation and its catastrophic consequences on sediment structure. However, inherent sampling effects caused by unavoidable changes in effective stress remain. These changes are quite prominent and include: stress relaxation from lithostatic confinement to virtually no effective stress, the potential for internal fluid pressure drop and local dissociation even when chamber P-T conditions are within the stability field (i.e., a form of poro-elastic Mandel-Cryer effect coupled with phase transition), side friction along the liner, skeleton expansion and the potential for stain-induced decementation.

Clearly, in-situ testing can play an important role in the characterization of hydrate bearing sediments. However, in situ tests face their own technical challenges and interpretation difficulties, including the effect of tool insertion on measured properties.

Based on these observations and field experiences (Gulf of Mexico, Krishna-Godavari Basin, Ulleung Basin, and Mount Elbert), the comprehensive characterization of

hydrate-bearing sediments should include: (1) detailed analysis of available logging data, (2) pressure core characterization and monitored de-pressurization, (3) index properties (with emphasis on grain size distribution and fines content, specific surface, SEM microphotographs, mineralogy and plasticity, pH and pore fluid ionic concentration), and (4) laboratory tests on reconstituted specimens with synthetic hydrate saturation to determine the behavior of sediments as a function of effective stress and hydrate saturation (including: stiffness, strength, and hydraulic conductivity).

Index properties -analyzed within the framework of accumulated field and laboratory data- provide exceptional information related to hydrate pore habit and morphology, potential sediment properties and production-related information including the possibility of fines migration (Refer to Waite et al., 2009 for a comprehensive review of hydrate-free sediment properties).

The reconstitution of hydrate bearing sediments is hindered by inherent difficulties in forming methane hydrate from dissolved phase methane. Tetrahydrofuran THF presents important advantages as a proxy hydrate former (Lee et al., 2007). First, its complete miscibility in water enables accurate hydrate saturation control and fast hydrate formation from dissolved phase (i.e., no preferential formation at interparticle contacts). Second, THF hydrate forms at atmospheric pressure and standard geotechnical devices can be used to characterize hydrate bearing sediments.

6.7 Conclusions

Pressure core technology is needed for the proper evaluation of natural hydrate-bearing sediments.

The set of pressure core characterization tools PCCTs described in this chapter allow the manipulation, sub-sampling, and the extensive assessment of natural gas hydrate-bearing sediments under in situ pressure, temperature, and effective stress conditions.

In addition to pressure core testing, comprehensive characterization programs should include sediment index properties analyzed within the framework of available data for natural hydrate bearing sediments, and tests with remolded specimens with synthetic hydrate.

Pressure core technology can also be deployed to study other gas rich hydrocarbon formations such as deep sea sediments, coal bed methane, and gas shales.

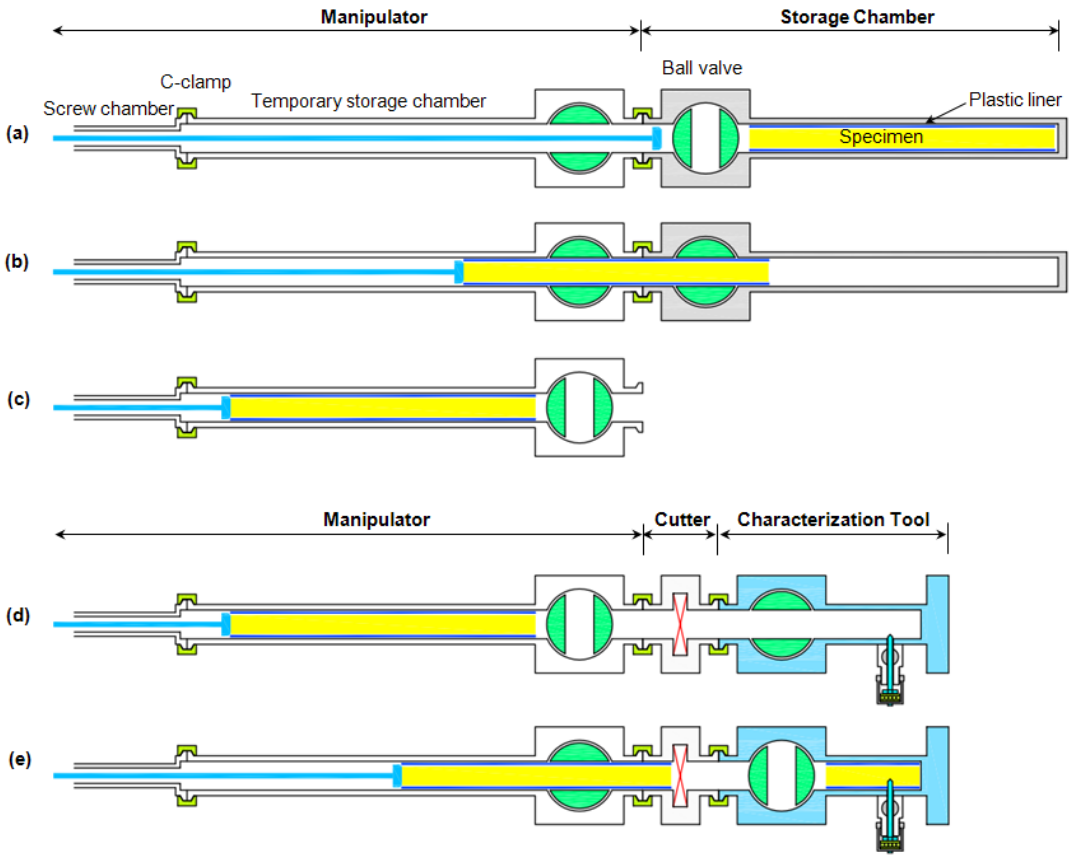

Figure 6.1 Pressure core manipulation. (a) The manipulator MAN couples with the storage chamber and fluid pressures are equalized at the target pressure p_0 before opening the ball valve. (b) The manipulator captures the core and transfers it into the temporary storage chamber. (c) Ball valves are closed and the depressurized storage chamber is separated. (d) The selected characterization tool is coupled to the manipulator and is pressurized to p_0. (e) Ball valves are opened and the core is pushed into the characterization tool; stand-alone characterization tools may be detached after retrieving the rest of the core and closing valves. Note: the cutter tool CUT is shown in panes d&e; it is attached in series to cut core to any desired length to meet tool requirements (for stand-alone ESC, DSC, CDP, and Bio tools).

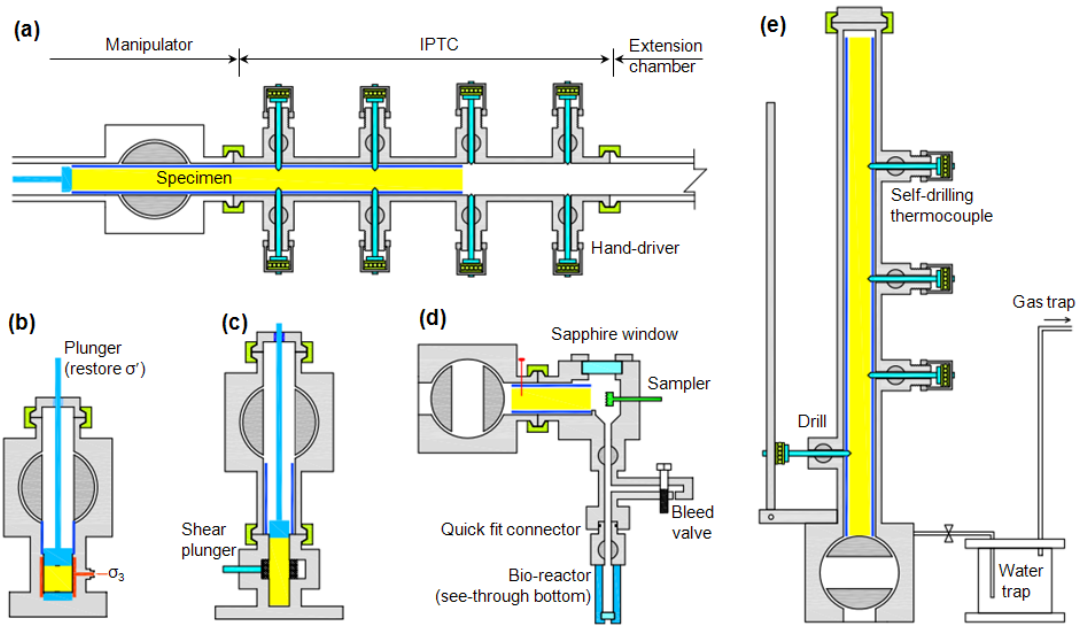

Figure 6.2 Schematic diagrams of characterization chambers. (a) IPTC instrumented pressure testing chamber with P-T control. (b) ESC effective stress chamber with σ'-P-T control. (c) DSC direct shear chamber with σ'-τ-P-T control. (d) CDP controlled depressurization chamber for sediment preservation and gas production. (e) BIO sampler for multiple bio-reactor chambers. Scale: the outside diameter of the large ball valve shown in all devices is OD = 220 mm.

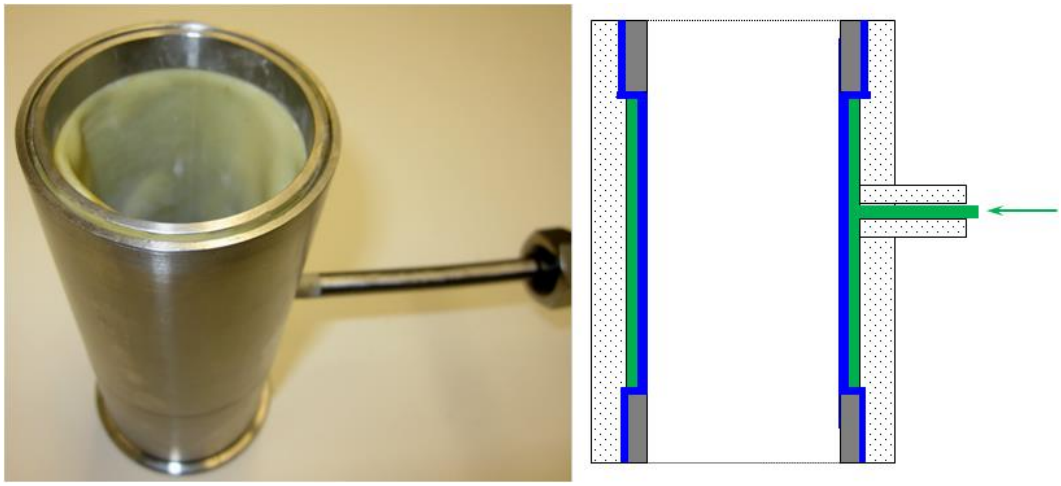

Figure 6.3 Flexible wall boundary condition. Lateral effective stress can be independently applied through a flexible wall membrane gadget (ID = 63.5mm, H = 150mm). This device allows the implementation of triaxial test conditions, and prevents preferential flow paths along the interface for fluid conductivity studies.

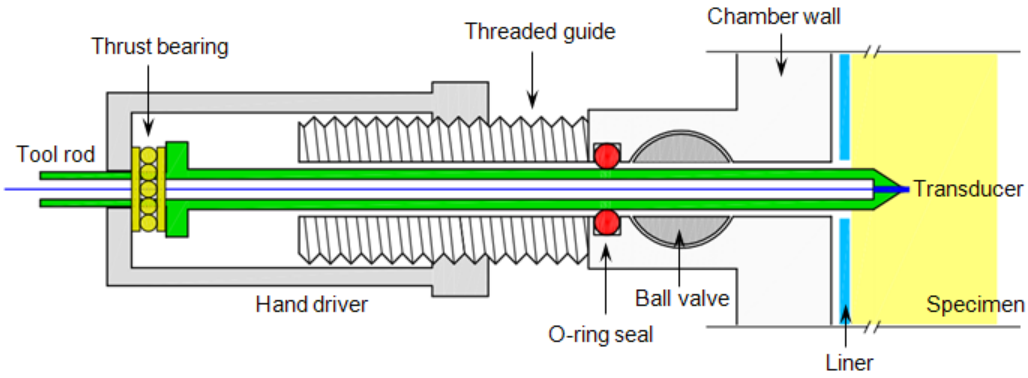

Figure 6.4 Tool Control. The displacement of sensors, subsampling tools and drills are controlled under pressure using a screw-based positioning system where the driver advances along the threaded guide while pushing the tool rod (shown in green). Transducers at the tip of the rod are wired through the central hole in the tool rod.

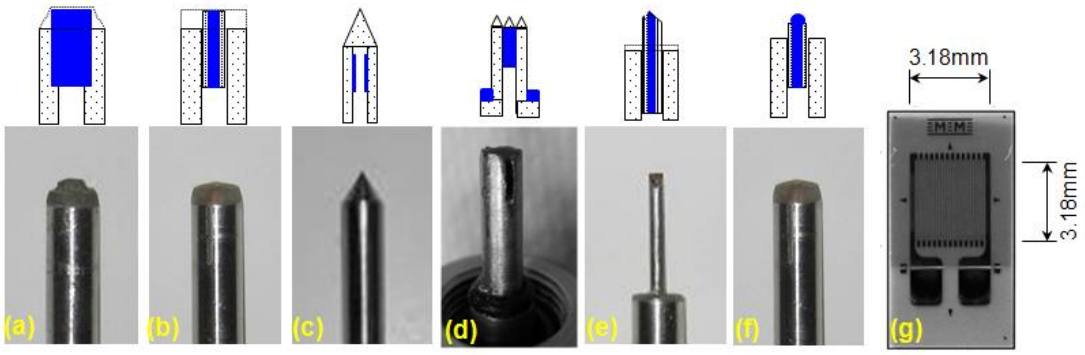

Figure 6.5 Measurement tools and sensors. (a) Bender elements for *S*-wave generation and detection. (b) Piezocrystals for *P*-waves. (c) Penetrometer for strength measurement. (d) Pore fluid sampler. (e) Electrical needle probe for resistivity profiling. (f) Thermocouple instrumented tip. (g) Strain gauge for thermal conductivity determination (TPS – NETL; Rosenbaum, et al., 2007).

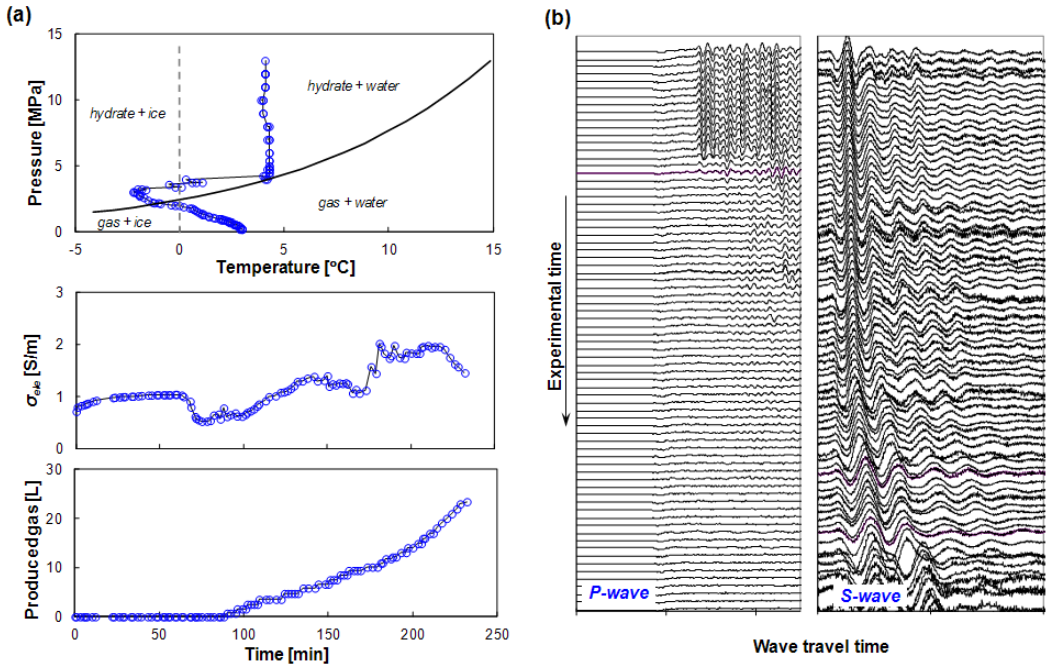

Figure 6.6 Monitored gas production tests using IPTC: (a) Evolutions of pressure, temperature, electrical resistivity, and produced gas (Krishna-Godavari Basin, Yun, et al., 2010); (b) Typical wave signatures during gas production: P-wave signatures eventually fade out after gas production; S-waves detect the evolution of the skeleton shear stiffness during hydrate dissociation and gas production (Ulleung Basin, Yun, et al., 2011).

CHAPTER 7

NANKAI TROUGH PRESSURE CORE STUDY – BIO-CHAMBER

7.1 Introduction

Methane gas trapped in hydrates is either biogenic or thermogenic. Biogenic gas accounts for 99% of the methane found in hydrate-bearing sediments [Kvenvolden, 1993]. Biological studies are necessary to elucidate the origin of hydrate-bearing sediments and to understand the complex hydro-chemo-bio-thermo-mechanical coupling in the sub-surface.

Sub-sampling chambers for pressure cores have been designed to provide specimens for biological testing while maintaining hydrate in the stability field and anaerobic conditions [Parkes et al., 2009; Santamarina et al., 2012]. The bio-sub-sampling BIO chamber, which is a part of the pressure core characterization tools PCCTs described in Chapter 6, was deployed for the first time to study Nankai Trough sediments. This chapter documents the operation of the BIO-chamber for stand-alone multi-bio-samplings. It describes fundamental biological experiments and reports on measured hydrate saturation as a byproduct of these tests.

7.2 Previous Biological Studies on Hydrate-Bearing Sediments

Quantification and Gene Analyses. Several studies have been conducted to quantify and analyze genes of microorganisms in hydrate-bearing sediments; these include:

- Cell counting with direct counting methods (color: acridine orange, SYBR green, and others), catalyzed reporter deposition-fluorescence in-situ hybridization (CARD-FISH), and quantitative, real-time polymerase chain reaction (Q-PCR) [Reed et al., 2002; Schippers et al., 2005; Sakamoto et al., 2005]
- Genetic study with PCR for 16s rRNA [Parkes et al., 2000; Reed et al., 2002; Nunoura et al., 2008; Parkes et al., 2009]
- The metagenomics of the microbial community [Biddle et al., 2011].

Limiting Factor: Pore Size. Related studies have shown that the growth of microorganism in soils is limited by environmental factors such as nutrients and pore space [Mitchell and Santamarina, 2005; Rebata-Landa and Santamarina, 2006; Phadnis and Santamarina, 2011; Eilers et al., 2012].

Biological Metabolism and Hydrocarbon Source. Consumed isotopes is used as a measure to estimate biological metabolism. Because microorganisms prefer stable carbon molecules, biogenic gas has low carbon-isotopic composition [Kvenvolden, 1995; Sassen et al., 1999]. Methanogenesis is the biomediated reaction between CO_2 and H_2 to produce methane; conversely, the anaerobic oxidation of methane is the reverse reaction [Reeburgh, 2007; Colwell et al., 2008; Bowles et al., 2011]:

$$CO_2 + 4H_2 \leftrightarrow CH_4 + 2H_2O \qquad [7.1]$$

Contamination Control. Drilling fluids can contaminate recovered soil samples. Florescent tracers or microspheres can be injected into the drilling fluid to assess the extent of contamination [Smith et al., 2000a; Smith et al., 2000b; House et al., 2003], so that biological studies are conducted on indigenous microorganisms.

7.3 Experimental Study

7.3.1 Case History – Pressure Core

Hydrate-bearing sediments in the Nankai Trough have been studied to understand geological processes, to assess their mechanical properties, chemical compositions, and biological activity [Colwell et al., 2004; Masui et al., 2008; Fujii et al., 2009; Kida et al., 2009; Uchida et al., 2009; Conin et al., 2011; Raimbourg et al., 2011]. Microorganism cell counts in methane hydrate-bearing sediments from the Nankai Trough decreased with depth [Reed et al., 2002]. Isotopic analyses on carbon and hydrogen have shown that methane from the Nankai Trough is mainly biogenic [Uchida et al., 2009].

The hybrid pressure coring system was used to retrieve hydrate bearing sediments (July, 2012). Pressure cores were analyzed on-board (X-ray, ultrasonic and γ-density), and were stored in a cold room at 4 °C under 20 MPa for future testing [Yamamoto et al., 2012].

The core selected for biological testing was recovered at a depth of 1276.6 mbsl and an overburden of 278 mbsf. The in-situ temperature was 12°C. The specimen was recovered from the middle of the core (Figure 7.1). The sediment is a silt with porosity n=0.475, specific surface S_s=19.42m^2/g, particle density ρ=2.621g/cm^3, and mean grain size d_{50}=8.8μm (Figure 7.1).

7.3.2 Operation for Bio-Sampling

A 17cm long specimen was cut from the core by using the SAW tool and transferred into the BIO-chamber using the manipulation system MAN (Chapter 6). Once loaded in BIO-chamber, the system was pressurized to 9MPa using argon gas to preserve anaerobic conditions. The temperature and pressure sensor were connected and the specimen was fixed using the locking nails (Figure 7.2a). Then the fluid filling the chamber was gradually flushed out and replaced with argon gas while maintaining the pressure. The cut specimen surface was grinded away as the surface was presumed to be contaminated during coring and cutting (contamination tracers were not injected during the core recovery). Finally, soil subsamples were collected for biological tests. The high pressure syringe built-in the scraper was used to inject nutrients and distilled water to force the recovery of sediments into the bioreactors. The weight of the six recovered samples are summarized in Table 7.1a. Once loaded, bioreactors were coupled to the manifold without pressure loss, and the fluid pressure was preserved throughout the test (Figure 7.2b).

7.3.3 Microbial Growth Test

Preparation – Equipment and Nutrient Sterilization. Equipment, nutrients, and solutions for biological tests were autoclaved for 40 minutes at 100 kPa and 120 °C [Madigan et al., 2009]. Large devices could not be autoclaved and were washed with alcohol and rinsed with sterilized distilled water.

The concentration of the NaCl buffer solution was 8 g/L, and the nutrient was Lysogeny Broth (LB-Miller formula: 10g of tryptone, 5g of yeast extract, and 10g of NaCl in one liter of distilled water). This selected nutrient is a complex medium that prompts the

growth of a broad range of microorganisms. Agar plates used for culture growth were 60-mm diameter Petri-dishes filled with the solid nutrient prepared by mixing 15 g/L of agar into the LB-Miller formula. All tests were conducted following strict protocols to avoid contamination.

Growth Tests – Procedure. Tests were conducted to confirm the existence of active microorganisms in these sediments to estimate bacterial counts, to study the effects of depressurization rate on living microorganisms, and to assess the effect of temperature on microbial growth. Bio-reactors were depressurized from 7 MPa to atmospheric pressure in: (a) 1~2 seconds, i.e., a fast depressurization rate, (b) 1 minute, i.e., an intermediate depressurization rate, and (c) 30 minutes, i.e., a slow depressurization rate. After depressurization, bio-reactors were shaken to separate microorganisms from soil grain surfaces [Lindahl and Bakken, 1995; Riis et al., 1998]. The supernatant fluid was diluted with buffer solution to attain 10^{-1} and 10^{-3} concentration by volume. Then, the diluted supernatant fluid was used for the spread-plate cell count method on the LB-agar plate in order to count active microorganisms [Madigan et al., 2009]. Plates were covered with parafilm to prevent contamination and maintained at culturing temperatures 4, 10 and 30°C at atmospheric pressure. Table 7.1b summarizes the scope of the study. As plates were exposed to the atmosphere, only aerobes survive during incubation. Cell growth was photographically recorded.

7.3.4 Dissociation Test

The specimen that remained in the BIO-chamber was subjected to a mini-production test. First, water was pumped into the BIO-chamber to displace the argon gas in order to measure the volume of CH_4 produced. Stiffness tests were conducted via pressure-controlled volume changes to calculate the volume fraction of residual gas in the system. Depressurization was controlled using a needle valve, and a graduated cylinder was used to collect and measure the produced fluids (Figure 7.2a). Sensors in the chamber monitored the evolution of pressure and temperature inside the chamber; the thermocouple was 20 mm away from the specimen.

7.3.5 Results

Biological Test. Typical colony-forming units CFUs observed on agar plates are shown in Figure 7.3 at different incubation times. Counted CFUs are summarized in Table 7.2 for all tests. The colony forming time is defined by the appearance of a colony on each plate. Clearly visible CFUs few millimeters in diameters appeared on plates after 43 hours of incubation at 30 ºC. The morphology of most colonies was white and circular with convex top and smooth edge. Cell counts were based on identifiable CFUs, dilation and soil weight (Tables 7.2). Results summarized in Table 7.2 show viable cell counts ranging from 287 to 52084 cells/g. No consistent trend is observed as a result of different depressurization rates. Most CFUs were white color and some were orange; but CFUs cultures after fast depressurization conducted at 30ºC were red.

Dissociation Test. P-T path during depressurization is shown in Figure 7.4. The system was filled with 99.88% water based on stiffness tests. Although pressure decreased, temperature remained relatively constant, i.e., limited free gases in the system. The P-T diagram did not clearly capture the transition across the hydrate stability phase boundary: The temperature drop during the dissociation test was only $\Delta T = -0.13$ ºC. The produced gas was ~ 6 liters which corresponds to a hydrate volume of V_{hyd}= 34 mL. For a specimen size 310 mL and porosity n=0.475, the estimated hydrate saturation is S_{hyd}=23%.

7.4 Analyses and Discussion

Justification. Barophiles live at high pressure and their metabolism may stop at atmospheric pressure. Furthermore, the radical pressure drop from high pressure to atmospheric pressure experienced in marine sediments during conventional sampling may physically damage and biochemically disturb microorganisms [Fraser, 1951; Nakamura et al., 1994; Patterson, 2005]. For example, gas vacuolate bacteria may burst due to gas expansion during fast pressure drop [Hemmingsen and Hemmingsen, 1980]. In contrast, bacteria without a gas vacuolate such as Escherichia coli can readily sustain a 30 MPa pressure drop even as gas bubbles instantaneously come out of solution [Hemmingsen and Hemmingsen, 1980]. In addition, depressurization and exposure to oxygen in the atmosphere is lethal to obligate anaerobes such as methanogens, so viable, culturable microorganisms are limited during biological tests conducted with exposed specimens. Note that tests could have been conducted under the anaerobic condition by conducting all

operations within an anaerobic incubator such as a glove box filled with argon gas at atmospheric pressure.

Counts. Results from this study show that the number of culturable cells measured using the spread-plate method is lower than observed in previous studies (Figure 7.5). The lower number can reflect:

- Culturable microorganisms in the laboratory can be as low as 1% of the total number of microorganisms [Madigan et al., 2009], because of lethal changes to some species of microorganisms, such as the methanogens exposed to atmospheric condition.
- Dead or inactive microorganisms cannot be detected by the spread-plate method. Previous studies typically used staining methods, and counts include dead and alive microorganisms (Figure 7.5a).
- Analytical upper bound estimates of cell count based on pore-size restriction do not take into consideration other limiting factors such as nutrients (Figure 7.5b).

Temperature. The temperature during culturing had a clear effect on growth rate. Bacterial growth in 30°C was fastest (in-situ temperature ~12°C) such as mesophiles that prefer 10 and 30°C [Madigan et al., 2009]. Observable red colonies occurred at 10 and 30°C.

Pressure. No obvious pattern with depressurization rate could be observed based on CFUs. Yet, the various colors of the colonies indicate that different microorganisms survived the various depressurization rates.

Hydrate Saturation. The dissociation test showed a hydrate saturation S_{hyd}=23 %; this value is considered high value for fine grained sediments [Waite et al., 2009].

Phase Transition. Lack of collocation between the thermocouple and the sediment where dissociation takes place did not allow a clear detection of the P-T phase boundary during dissociation. The temperature drop can be calculated using geometrical and physical properties of the system consisting of quartz (soil), stainless steel (BIO-chamber), hydrate and water (Table 7.3). The endothermic heat required to dissociate hydrate in the sediment is H_{Diss}:

$$H_{Diss} = L_h \rho_h V_h = 7.3 kJ \qquad [7.2]$$

where L [kJ/kg] is the latent heat, ρ [kg/m^3] density, V [m^3] volume, and subscript h is used to denote hydrate. The endothermic heat of dissociation causes a volume-average temperature drop ΔT equal to:

$$\Delta T = \frac{H_{Diss}}{\sum c_i \rho_i V_i} = \frac{H_{Diss}}{c_w \rho_w V_w + c_h \rho_h V_h + c_{ss} \rho_{ss} V_{ss} + c_q \rho_q V} \qquad [7.3]$$

where c is specific heat and subscripts w=water, q=quartz, and ss=stainless steel. The computed temperature drop ΔT=−0.2°C is in agreement with the temperature drop ΔT=−0.13 °C, measured ~20 mm away from the cooling specimen.

7.5 Conclusions

The BIO-chamber was deployed to conduct biological studies in the context of hydrate-bearing sediments. The chamber was first deployed as part of the pressure-core characterization studies for the Nankai Trough. Salient conclusions from this experience follow:

- The BIO-chamber allowed for the successful collection of uncontaminated bio-samples at in-situ pressure and temperature while preserving anaerobic conditions.
- The spread method for cell counts detects viable cells. However, the aerobic implementation in this first study was lethal to anaerobes such as methanogens; previous studies based on staining methods identified both alive and dead cells. Consequently, cell counts in this study were lower.
- Surviving microorganisms showed clear temperature-dependent growth rate.
- Evidence of depressurization rate effects on survivability is limited to changes in colony color.
- The measured hydrate saturation is S_{hyd}=23%. The measured global temperature drop inside the BIO-chamber is compatible with this hydrate saturation.

Table 7.1 Experimental study – parameters: (a) weight of samples obtained for different depressurization tests and (b) experimental matrix – number of agar plates used for cell counts

(a)

	Sample Number*	Depressurization Rate		
		$\frac{7MPa}{30\,\text{min}}$	$\frac{7MPa}{1\,\text{min}}$	$\frac{7MPa}{2s}$
Collected Soil Weight [g]	1 to 3	0.21	0.4	1.34
	4 to 6	0.13	0.16	0.17

*The total number of samples is six.

(b)

Depressurization rate	Number of Agar Plates (1 atm)					
	T=4 ºC		T=10 ºC		T=30 ºC	
	Dilution 10^{-1}	Dilution 10^{-3}	Dilution 10^{-1}	Dilution 10^{-3}	Dilution 10^{-1}	Dilution 10^{-3}
$\frac{7MPa}{30\,\text{min}}$	3	3	6	6	3	3
$\frac{7MPa}{1\,\text{min}}$	3	3	6	6	3	3
$\frac{7MPa}{2s}$	3	3	6	6	3	3

Table 7.2 Colony-forming units

Temperature [ºC]		4			10			30		
Depressurization Rate		$\frac{7\,MPa}{30\,\text{min}}$	$\frac{7\,MPa}{1\,\text{min}}$	$\frac{7\,MPa}{2\,\text{sec}}$	$\frac{7\,MPa}{30\,\text{min}}$	$\frac{7\,MPa}{1\,\text{min}}$	$\frac{7\,MPa}{2\,\text{sec}}$	$\frac{7\,MPa}{30\,\text{min}}$	$\frac{7\,MPa}{1\,\text{min}}$	$\frac{7\,MPa}{2\,\text{sec}}$
Colony Forming Time [days]		N/A	11	11	18	11	11	11	2	2
Total Cell Count [cells/g]	10^{-1} dilution	N/A	287	891	356	469	1154	2018	495	1538
	10^{-3} dilution	N/A	N/A	2473	N/A	7813	4534	N/A	52084	3297

Table 7.3 Gravimetric and thermal properties of materials in the BIO-chamber

	CH_4-Hydrate	Water	SS316	Quartz
Latent heat [kJ/kg]	435[1)]			
Density [kg/m3]	929[2)]	1000[3)]	8000[4)]	2650[5)]
Specific Heat [kJ/kg·°C]	2.031[2)]	4.2[3)]	0.5[4)]	0.73[5)]
Volume [ml]	18.1	1018.7	8592.2	160.0

[1)] Handa (1986)

[2)] Waite et al. (2007)

[3)] Weast (1987)

[4)] ASM Internaltional Materials Properties Database Committee (2002)

[5)] Kaye and Laby (Tables of physical and chemical constants, National Physical Laboratory, 2008, http://www.kayelaby.npl.co.uk/)

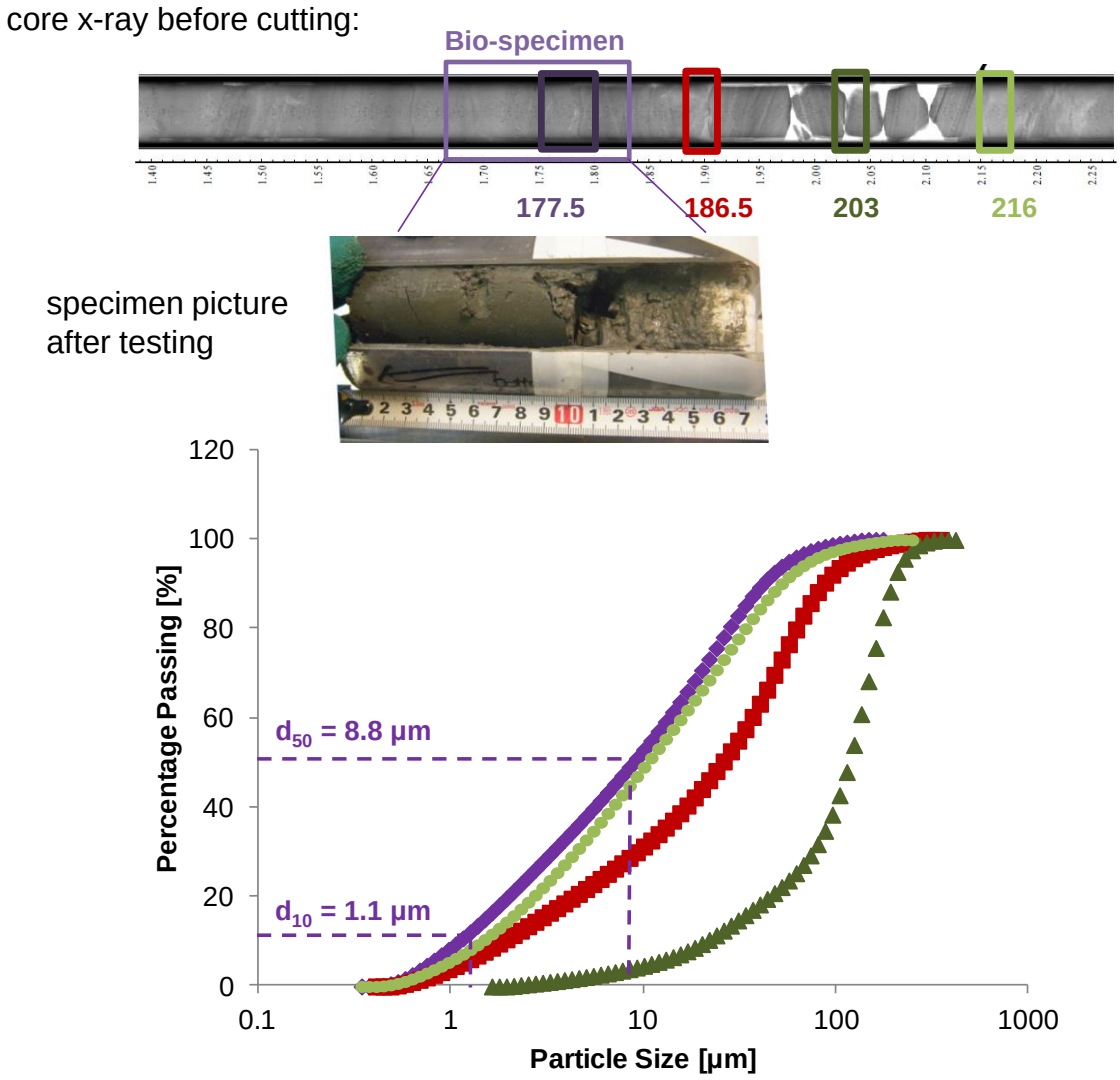

Figure 7.1 Core, sample cut for bio-studies and its grain size distribution (from AIST and JOGMEC, 2012).

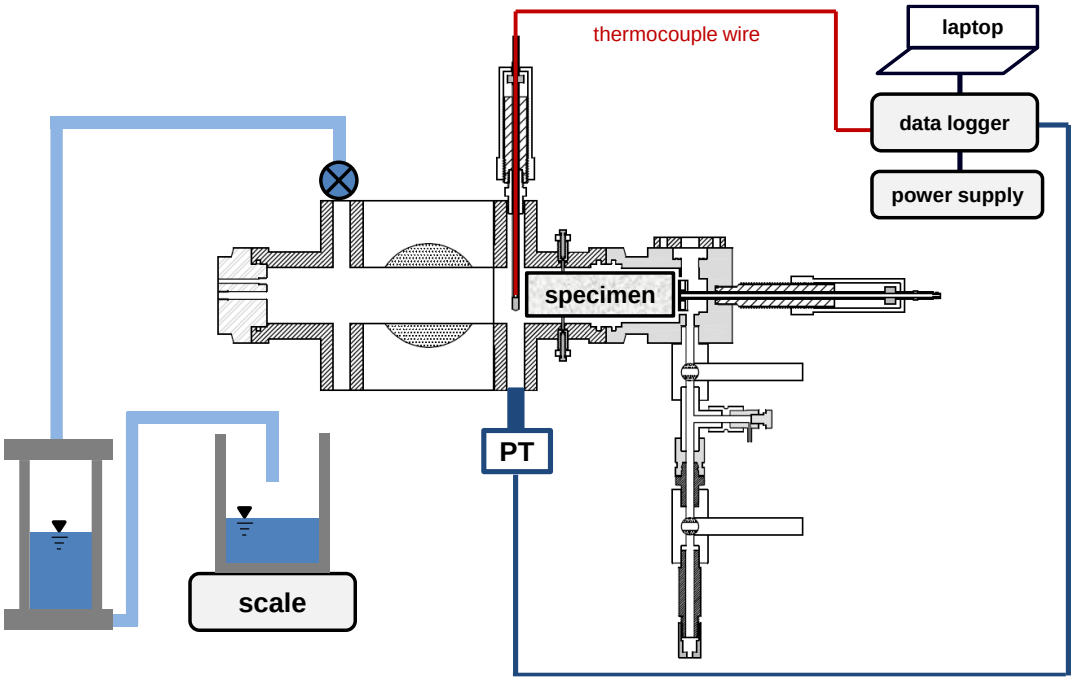

(a)

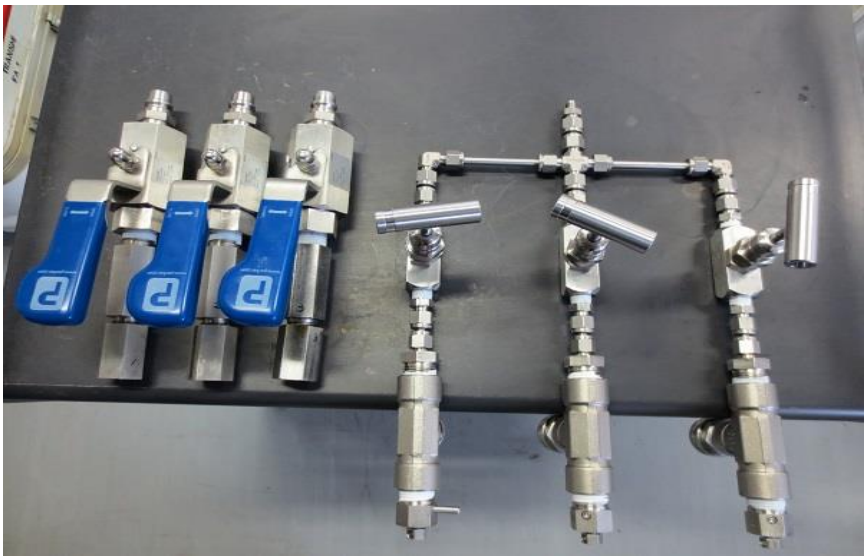

(b)

Figure 7.2 Experimental configurations with the BIO-chamber: (a) operations in the cold room and (b) manifold and three bio-reactors.

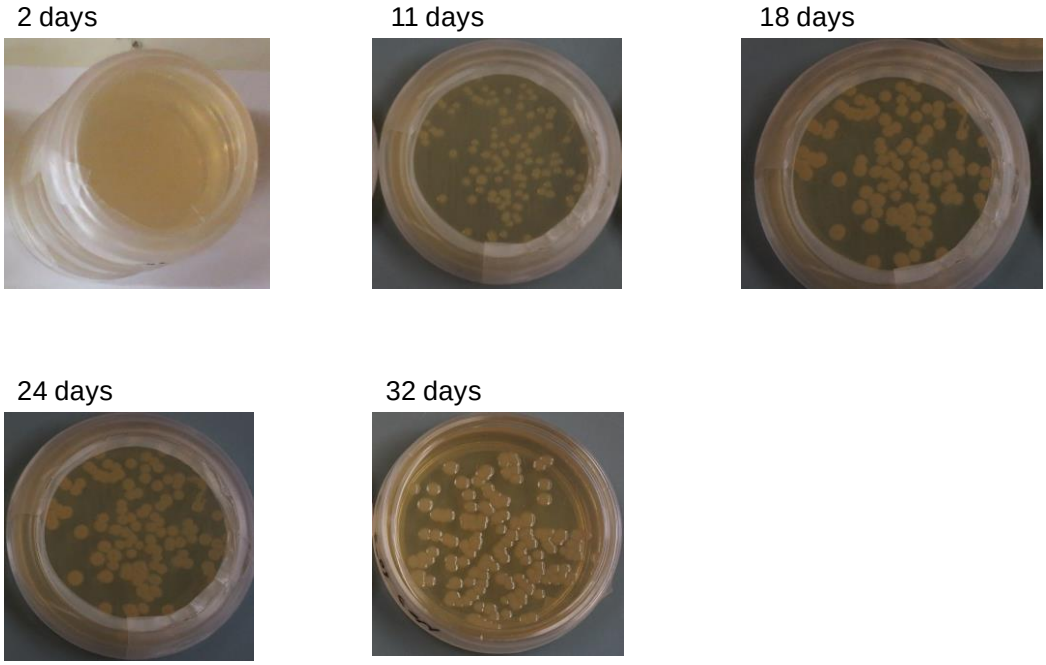

Figure 7.3 Culture at different times. Depressurization rate=7MPa/2s, 4ºC and 10^{-1} dilution.

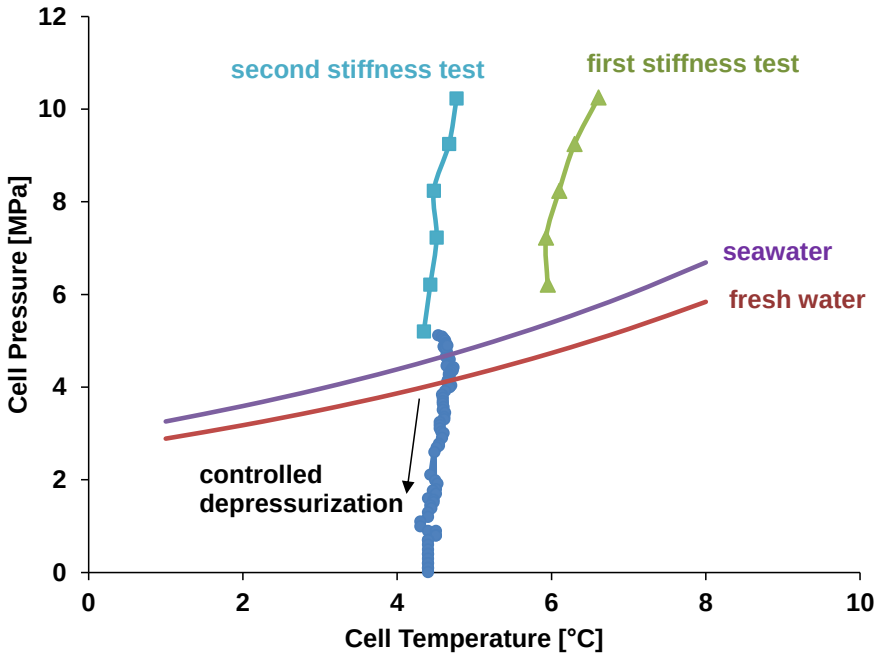

Note: The CH_4-hydrate stability boundary of pure water and seawater are presented below [Tishchenko et al., 2005]:

$$\ln\left(P_{diss}^{sw}\right) = -1.6444866\cdot 10^{3} - 0.1374178\cdot T + \frac{5.4979866\cdot 10^{4}}{T} + 2.64118188\cdot 10^{2}\ln(T) + S\cdot\left[1.1178266\cdot 10^{4} + 7.67420344\cdot T - 4.515213\cdot 10^{-3}\cdot T^{2} - \frac{2.04872879\cdot 10^{5}}{T} - 2.17246046\cdot 10^{3}\ln(T)\right] + S^{2}\cdot\left[1.70484431\cdot 10^{2} + 0.118594073\cdot T - 7.0581304\cdot 10^{-5}\cdot T^{2} - \frac{3.09796169\cdot 10^{3}}{T} - 33.2031996\cdot\ln(T)\right]$$

where T [K] is temperature, P^{sw}_{dis} [Pa] the dissociation pressure in seawater, and S [‰] salinity.

Figure 7.4 Pressure and temperature during the controlled depressurization.

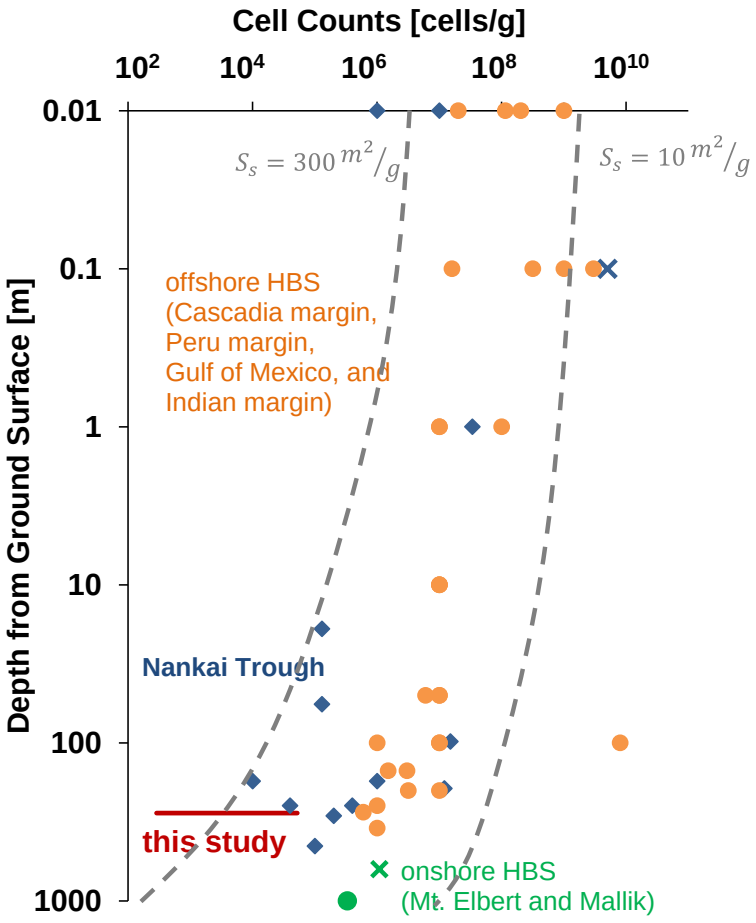

Figure 7.5 Cell counts in hydrate-bearing sediments [Cragg et al., 1996; Li et al., 1999; Reed et al., 2002; Knittel, et al., 2003; Kormas et al., 2003; Mills et al., 2003; Newberry et al., 2004; Colwell et al., 2005; Inagaki et al., 2006; Webster et al., 2006; Colwell et al., 2011; Mills et al., 2012] and theoretical limits (gray lines) to cell numbers due to pore size restriction [Phadnis and Santamarina, 2011].

CHAPTER 8

CONCLUSIONS

This study focused on hydrate-bearing sediments with emphasis on fine-grained sediments in view of gas production. Experiments and analyses addressed the classification of fines, volume changes in sediments resulting from hydrate dissociation, capillarity in multi-phase systems, gas propagation mechanisms, high-pressure chambers for characterization and fundamental biological experiments. Salient conclusions from this study follow.

Fine and Fine-Grained Sediments

- A new procedure is recommended for fine-grained soil classification. It highlights sensitivity to electrical forces and specific surface.
- The fall cone test can be used to assess the electrical sensitivity of fines due to change in van der Waals attraction and the double-layer repulsion.

Volume Contraction during Hydrate Dissociation

- Volume changes in sediments during thaw consolidation depend on the initial void ratio, ice or hydrate saturation and vertical effective stress.
- Terminal void ratios during thaw consolidation are between e_{min} and e_{max}.
- A new approach is proposed to estimate the possible vertical strain that sandy or silty sediments can experience during hydrate dissociation. It takes into account the initial relative density, the state of stress and the compression index.

The Effect of Surfactants on Capillarity during Mixed-Fluid Flow

- Capillary pressure in multi-phase systems depends on flow channel geometry and interfacial tension.
- Surfactants reduce interfacial tension and can be used to modify contact angles and lower capillary pressure.
- Surfactant self-regulation and adsorption at pore throats alters the capillary pressure response as the gas-liquid interface passes through pore throats.

Gas Recovery from Fine-Grained Sediments

- Gas propagation in hydrate-bearing sediments depends on gas flow rates and sediment types.
- Either capillary or drag forces can cause gas-driven fractures in fine-grained sediments during hydrate dissociation, particularly at stratigraphic boundaries.
- Gas-driven fractures facilitate gas recovery from fine-grained hydrate-bearing sediments. This gas recovery mechanism expands the potential for gas-recovery to fine-grained hydrate bearing sediments.

Pressure Core Characterization Tools

- A set of unprecedented pressure core characterization tools PCCTs was designed, built and deployed to manipulate sub-sample and conduct extensive assessment of natural gas hydrate-bearing sediments under in-situ pressure, temperature, and effective stress conditions.

- PCCTs can also be deployed to study other gas rich hydrocarbon formations such as deep-sea sediments, coal bead methane and gas shales.

Nankai Trough Pressure Core Study – Biological Studies

- A BIO-chamber was designed and built to gather bio-samples for biological tests without hydrate dissociation or contamination and under anaerobic conditions.
- Viable cells were identified at the Nankai Trough.
- Microorganism growth tests confirmed temperature effects.
- The measured hydrate saturation for the tested fine-grained sediments at the Nankai Trough was S_{hyd}=23%.

REFERENCES

Abegg, F., Hohnberg, H. J., Pape, T., Bohrmann, G., and Freitag, J. (2008). "Development and application of pressure-core-sampling systems for the investigation of gas- and gas-hydrate bearing sediments." *Deep Sea Res. Part I Oceanogr. Res. Pap.*, 1590-1599.

Andersland, O. B., Sayles, F. H., and Ladanyi, B. L. (1978). "Mechanical properties of frozen ground." *Geotechnical Engineering for Cold Regions*, Andersland, O. B. and Anderson, D. M., eds., McGraw-Hill Book Company.

Anderson, D. M., Pusch, R., and Penner, E. (1978). "Physical and thermal properties of frozen ground." *Geotechnical Engineering for Cold Regions*, Andersland, O. B. and Anderson, D. M., eds., McGraw-Hill Book Company, 37-102.

Arenson, L. U. and Springman, S. M. (2005). "Triaxial constant stress and constant strain rate tests on ice-rich permafrost samples." *Canadian Geotechnical Journal*, 42, 412-430.

ASM International Materials Properties Database Committee (2002). *ASM Ready Reference: Thermal Properties of Metals*, Cverna, F. (ed), 560 pp, ASM International.

ASTM-D422 (2007). *Standard Test Method for Particle-Size analysis of Soils*, ASTM International.

ASTM-D2487 (2011). *Standard Practice for Classification of Soils for Engineering Purposes (Unifined Soil Classification System)*, ASTM International.

ASTM-D2488 (2009). *Standard Practice for Description and Identification of Soils (Visual-Manual Procedure)*, ASTM International.

Aubertin, M., Richard, J., and Chapuis, R. P. (1998). "A predictive model for the water retention curve: application to tailings from hard-rock mines." *Canidian Geotechnical Journal*, 35, 55-69.

Baver, L. D., Gardner, W. H., and Gardner, W. R. (1972). *Soil Physics*, John Wiley & Sons, New York.

Bear, J. (1972). *Dynamics of Fluids in Porous Media*, American Elsevier Publishing Company, Inc.

Been, K. and Jefferies, M. G. (1985). "A state parameter for sands." *Geotechnique*, 35(2), 99-112.

Biddle, J. F., White, J. R., Teske, A., and House, C. H. (2011). "Metagenomics of the subsurface Brazos-Trinity Basin (IODP site 1320): comparison with other sediment and pyrosequenced metagenomes." *Multidisciplinary Journal of Microbial Ecology*, 5, 1038-1047.

Boron, W. F. and Boulpaep, E. L. (2009). *Medical Physiology: A Cellular and Molecular Approach*, Elsevier.

Boswell, R. and Collett, T. S. (2011). "Current perspectives on gas hydrate resources." *Energy & Environmental Science*, 4, 1206-1215.

Bowles, M. W., Samarkin, V. A., and Joye, S. B. (2011). "Improved measurement of microbial activity in deep-sea sediments at in situ pressure and methane concentration." *Limnology and Oceanography: Methods*, 9, 499-506.

Brooks, R. H. and Corey, A. T. (1964). "Hydraulic properties of porous media." *Colorado State University (Fort Collins), Hydrology Paper No. 3*.

BS1377 (1990). *Methods of Test for Soils for Civil Engineering Purpose*.

Calvello, M., Lasco, M., Vassallo, R., and Di Maio, C. (2005). "Compressibility and residual shear strength of smectitic clays: influence of pore aqueous solutions and organic solvents." *Rivista Italiana Di Geotecnica*, 39(1), 34-46.

Casagrande, A. (1938). *Notes on soil mechanics - first semester*, Harvard University.

Casagrande, A. (1948). "Classification and identification of soils." *Transactions, American Society of Civil Engineers*, 113, 901-930.

Casagrande, A. (1958). "Notes on the design of the liquid limit device." *Geotechnique*, 8(2), 84-91.

Cerato, A. B. and Lutenegger, A. J. (2002). "Determination of surface area of fine-grained soils by the ethylene glycol monoethyl ether (EGME) method." *Geotechnical Testing Journal*, 25(3), GTJ11087J.

Chamberlain, E. J. and Gow, A. J. (1979). "Effect of freezing and thawing on the permeability and structure of soils." *Engineering Geology*, 13, 73-92.

Cho, G. C., Dodds, J., and Santamarina, J. C. (2006). "Particle shape effects on packing density, stiffness, and strength: natural and crushed sands." *Journal of Geotechnical and Geoenvironmental Engineering*, 132(5), 591-602.

Cho, G. C., Lee, J. S., and Santamarina, J. C. (2004). "Spatial variability in soils." *Journal of Geotechnical and Geoenvironmental Engineering*, 130(8), 843-850.

Cho, G. C. and Santamarina, J. C. (2001). "Unsaturated particulate materials: Particle-level studies." *Journal of Geotechnical and Geoenvironmental Engineering*, 127(1), 84 - 96.

Clements, J. A., Brown, E. S., and Johnson, R. P. (1958). "Pulmonary surface tension and the mucus lining of the lungs: some theoretical considerations." *Journal of Applied Physiology*, 12, 262-268.

Clennell, M. B., Hovland, M., Booth, J., Henry, P., and Winters, W. J. (1999). "Formation of natural gas hydrates in marine sediments: 1. Conceptual model of gas hydrate growth conditioned by host sediment properties." *Journal of Geophysical Research*, 104, 22985-23003.

Collett, T. S. (2002). "Energy resource potential of natural gas hydrates." *American Association of Petroleum Geologists Bulletin*, 86(11), 1971-1992.

Colwell, F., Matsumoto, R., and Reed, D. (2004). "A review of the gas hydrates, geology, and biology of Nankai Trough." *Chemical Geology*, 205, 391-404.

Colwell, F., Schwartz, A., and Briggs, B. (2011). "Microbial community distribution in sediments from the Mount Elbert gas hydrate stratigraphic test well, Alaska North slope." *Marine and Petroleum Geology*, 28, 404-410.

Colwell, F. S., Boyd, S., Delwiche, M. E., Reed, D. W., Phelps, T. J., and Newby, D. T. (2008). "Estimates of biogenic methane production rates in deep marine sediments at hydrate ridge, Cascadia Margin." *Applied and Environmental Microbiolgy*, 74(11), 3444-3452.

Colwell, F. S., Nunoura, T., Delwiche, M. E., Boyd, S., Bolton, R., Reed, D. W., Takai, K., Lehman, R. M., Horikoshi, K., Elias, D. A., and Phelps, T. J. (2005). "Evidence of minimal methanogenic numbers and activity in sediments collected from the JAPEX/JNOC/GSC et al. Mallik 5L-38 gas hydrate production research well." *Geological Survey of Canada*, 585, 1-11.

Conin, M., Henry, P., Bourlange, S., Raimbourg, H., and Reuschle, T. (2011). "Interpretation of porosity and LWD resistivity from the Nankai accretionary wedge in light of clay physicochemical properties: Evidence for erosion and local overpressuring." *Geochemistry Geophysics Geosystems*, 12, Q0AD07.

Cragg, B. A., Parkes, R. J., Fry, J. C., Weightman, A. J., Rochelle, P. A., and Maxwell, J. R. (1996). "Bacterial populations and processes in sediments containing gas hydrates (ODP Leg 146: Cascadia Margin)." *Earth and Planetary Science Letters*, 139, 497-507.

Creuwels, L. A. J. M., van Golde, L. M. G., and Haagsman, H. P. (1997). "The pulmonary surfactant system: Biochemical and clinical aspects." *Lung*, 175, 1-39.

Dai, S., Lee, C., and Santamarina, J. C. (2011). "Formation history and physical properties of sediments from the Mount Elbert Gas Hydrate Stratigraphic Test Well, Alaska North Slope." *Marine and Petroleum Geology*, 28, 427-438.

Dai, S., Santamarina, J. C., Waite, W. F., and Kneafsey, T. J. (2012). "Hydrate morphology: Physical properties of sands with patchy hydrate saturation." *Journal of Geophysical Research*, 117, B11205.

Danzl, D. F. (1992). "Flatology." *The Journal of Emergency Medicine*, 10, 79 - 88.

de Gennes, P. G. (1985). "Wetting: static and dynamics." *Reviews of Modern Physics*, 57(3), 827-863.

Defay, R. and Prigogine, I. (1949). "Surface tension of regular solutions." *Transactions of the Faraday Society*, 46, 199-204.

Delahaye, C. H. and Alonso, E. E. (2002). "Soil heterogeneity and preferentical paths for gas migration." *Engineering Geology*, 64, 251-271.

Deresiewicz, H. (1958). "Mechanics of Granular Matter." *Advances in Applied Mechanics*, 5, 233-306.

Di Maio, C. and Fenelli, G. B. (1994). "Residual strength of kaolin and bentonite: the influence of their constituent pore fluid." *Geotechnique*, 44(4), 217-226.

Dickens, G. R., Schroeder, D. K., Hinrichs, U., and Party, t. L. S. (2003). "The pressure core sampler (PCS) on ODP Leg201: General operations and gas release." *Proc. ODP, Init. Repts., 201*, College Station, TX (Ocean Drilling Program), 1-22.

Dolinar, B. and Trauner, L. (2005). "Impact of soil composition on fall cone test results." *Journal of Geotechnical and Geoenvironmental Engineering*, 131(1), 126-130.

Donohew, A. T., Horseman, S. T., and Harrington, J. F. (2000). "Gas entry into unconfined clay pastes at water contents between the liquid and plastic limits." *Environmental Mineralogy: Microbial Interactions, Anthropogenic Influences, Contaminated Land and Waste Management*, Cotter-Howells, J. D., Campbell, L. S., Valsami-Jones, E., and Batchelder, M., eds., Mineralogical Society, London, 369-394.

Dumbleton, M. and West, G. (1966). "Some factors affecting the relation between the clay minerals in soils and their plasticity." *Clay Minerals*, 6, 179-193.

Eastoe, J. and Dalton, J. S. (2000). "Dynamic surface tension and adsorption mechanisms of surfactants at the air-water interface." *Advances in Colloid and Interface Science*, 85, 103-144.

Eilers, K. G., Debenport, S., Anderson, S., and Fierer, N. (2012). "Digging deeper to finde unique microbial communities: The strong effect of dept on the structure of bacterial and archaeal communities in soil." *Soil Biology and Biochemistry*, 50, 58-65.

Espinoza, D. N. and Santamarina, J. C. (2010). "Water-CO_2-mineral systems: interfacial tension, contact angle, and diffusion-implications to CO2 geological storage." *Water Resources Research*, 46, W07537.

Espinoza, D. N. and Santamarina, J. C. (2012). "Clay interaction with liquid and supercritical CO_2: The relevance of electrical and capillary forces." *International Journal of Greenhouse Gas Control*, 10, 351-362.

Farrar, D. M. and Coleman, J. D. (1967). "The correlation of surface area with other properties of nineteen British clay soils." *Journal of Soil Science*, 18(1), 118-124.

Feng, T.-W. (2000). "Fall-cone penetration and water content relationship of clays." *Geotechnique*, 50(2), 181-187.

Folmer, B. M. and Kronberg, B. (2000). "Effect of surfactant-polymer association on the stabilities of foams and thin films: Sodium dodecyl sulfate and poly (vinyl pyrrolidone)." *Langmuir*, 16, 5987-5992.

Fraser, D. (1951). "Bursting bacteria by release of gas pressure." *Nature*, 167, 33-34.

Fujii, T., Nakamizu, M., Tsuji, Y., Namikawa, T., Okui, T., Kawasaki, M., Ochiai, K., Nishimura, M., and Takano, O. (2009). "Methane-hydrate occurance and saturation confirmed from core samples, eastern Nankai Trough, Japan." *Natural Gas Hydrate - Energy Resource Potential and Associated Geologic Hazards*, Collett, T., Johnson, A., Knapp, C., and Boswell, R., eds., AAPG Memoir, 385-400.

Fukue, M., Okusa, S., and Nakamura, T. (1986). "Consolidation of sand-clay mixtures." *Consolidation of Soils: Testing and Evaluation. ASTM STP 892*, Yong, R. N. and Townsend, F. C., eds., American Society for Testing and Materials, Philadelphia, 627-641.

Germann, W. J. and Stanfield, C. L. (2002). *Principles of Human Physiology*, Benjamin Cummings.

Ghadiali, S. N. and Gaver, D. P. (2008). "Biomechanics of liquid-epithelium interactions in pulmonary airways." *Respiratory Physiology & Neurobiology*, 163, 232-243.

Ghadiali, S. N. and Gaver III, D. P. (2000). "An investigation of pulmonary surfactant physicochemical behavior under airway reopening conditions." *Journal of Applied Physiology*, 88, 493-506.

Goerke, J. (1998). "Pulmonary surfactant: functions and molecular composition." *Biochimica et Biophysica Acta*, 1408, 79-89.

Göktepe, A. B. and Sezer, A. (2010). "Effect of particle shape on density and permeability of sands." *Proceeding of the Institution of Civil Engineering, Geotechnical Engineering*, 163(GE6), 307-320.

Graton, L. C. and Fraser, H. J. (1935). "Systematic packing of spheres: With particular relation to porosity and permeability." *The Journal of Geology*, 43(8), 785-909.

Gregersen, H. (2002). *Biomechanics of the Gastrointestinal Tract: New Perspectives in Motility Research and Diagnostic*, Spinger.

Gregersen, H. and Christensen, J. (2000). "Gastrointestinal tone." *Neurogastroenterology & Motility*, 12, 501-508.

Grim, R. E. (1962). *Applied Clay Mineralogy*, McGraw-Hill Book Company, Inc.

Haines, W. B. (1930). "Studies in the physical properties of soil: V. The hysteresis effect in capillary properties, and the modes of moisture distribution associated therewith." *The Journal of Agricultural Science*, 20, 97-116.

Handa, Y. P. (1986). "Compositions, enthalpies of dissociation, and heat capacities in the range 85 to 270 K for clathrate hydrates of methane, ethane, and propane, and enthalpy of dissociation of isobutane hydrate, as determined by a heat-flow calorimeter." *Journal of Chemical Thermodynamics*, 18, 915-921.

Hansbo, S. (1957). "A new approach to the determination of the shear strength of clay by the fall-cone test." *Proceedings of the Royal Swedish Geotechnical Institute*, 14, 7-48.

Hansen, M. B. (2003). "Neurohumoral control of gastronitestinal motility." *Physiological Reviews*, 52, 1-30.

Harrington, J. F. and Horseman, S. T. (1999). "Gas transport properties of clays and mudrocks." *Muds and Mudstones: Physical and Fluid Flow Properties*, Aplin, A. C., Fleet, A. J., and Macquaker, J. H. S., eds., Geolotical Society, London, Special Publicaion, 158, 107-124.

Hawgood, S. and Clements, J. A. (1990). "Pulmonary surfactant and its apoproteins." *The Journal of Clinical Investigation*, 86, 1-6.

Hemmingsen, B. B. and Hemmingsen, E. A. (1980). "Rupture of the cell envelope by induced intracellular gas phase expansion in gas vacuolate bacteria." *Journal of Bacteriology*, 143(2), 841-846.

Hildenbrand, A., Schlomer, S., and Krooss, B. M. (2002). "Gas breakthrough experiments on fine-grained sedimentary rocks." *Geofluids*, 2, 3-23.

Hildenbrand, A., Schlömer, S., Krooss, B. M., and Littke, R. (2004). "Gas breakthrough experiments on pelitic rocks: comparative study with N_2, CO_2 and CH_4." *Geofluids*, 4, 61-80.

Hoffman, R. L. (1975). "A study of the advancing interface." *Journal of Colloid and Interface Science*, 50(2), 228-241.

Holder, G. D., Kamath, V. A., and Godbole, S. P. (1984). "The potential of natural gas hydrates as an energy resource." *Annual Review of Energy*, 9, 427-445.

Holmberg, K., Josson, B., Kronberg, B., and Lindman, B. (2003). *Surfactants and Polymers in Aqueous Solution*, John Wiley & Sons, Ltd.

Holtz, R. D. and Kovacs, W. D. (1981). *An Introduction to Geotechnical Engineering*, Prentice Hall.

Horseman, S. T., Harrington, J. F., and Sellin, P. (1999). "Gas migration in clay barriers." *Engineering Geology*, 54, 139-149.

House, C. H., Cragg, B. A., Teske, A., and party, L. s. (2003). "Drilling contamination tests during ODP leg 201 using chemical and particulate tracers." *Proceedings of the Ocean Drilling Program, Initial Reports*, D'Hondt, S. L., Jorgensen, B. B., and Miller, D. J., eds., 1-19.

Huang, Z., Yan, Z., and Gu, T. (1989). "Mixed adsorption of cationic and anionic surfactants from aqueous solution on silica gel." *Colloids and surfaces*, 36, 353-358.

Iglauer, S., Wu, Y., Shuler, P., Tang, Y., and Goddar III, W. A. (2010). "New surfactant classes for enhanced oil recovery and their tertiary oil recovery potential." *Journal of Petroleum Science and Engineering*, 71, 23-29.

Inagaki, F., Nunoura, T., Nakagawa, S., Teske, A., Lever, M., Lauer, A., Suzuki, M., Takai, K., Delwich, M., Colwell, F. S., Nealson, K. H., Horlkoshi, K., D'Hondt, S. L., and Jørgensen, B. B. (2006). "Biogeographical distributin and diversity of microbes in methane hydrate-bearing deep marine sediments on the Pacific Ocean Margin." *Proceedings of the National Academy of Science of the United States of America*, 103(8), 2815-2820.

Israelachvili, J. N. (2011). *Intermolecular and Surface Forces*, Academic Press.

Jamiolkowski, M., Ladd, C. C., Germain, J. T., and Lancellotta, R. (1985). "New developments in field and laboratory testing of soils." *Proceedings of the Eleventh International Conference on Soil Mechanics and Foundation Engineering, San Francisco*, 1(57-153).

Jang, J. W. and Santamarina, J. C. (2011). "Recoverable gas from hydrate-bearing sediments: Pore network model simulation and macroscale analyses." *Journal of Geophysical Research - Solid Earth*, 116, B08202.

Johannessen, A. M. and Spildo, K. (2013). "Enhanced oil recovery (EOR) by combining surfactant with low salinity injection." *Energy and Fuels*, 27, 5738-5749.

Jung, J. W., Jang, J., Santamarina, J. C., Tsouris, C., Phelps, T. J., and Rawn, C. J. (2012). "Gas production from hydrate-bearing sediments: the role of fine particles." *Energy Fuels*, 26, 480-487.

Jung, J. W. and Santamarina, J. C. (2011). "Hydrate adhesive and tensile strengths." *Geochemistry Geophysics Geosystems*, 12(8), Q08003.

Jung, J. W. and Santamarina, J. C. (2012). "Hydrate formation and growth in pores." *Journal of Crystal Growth*, 345, 61-68.

Jung, J. W., Santamarina, J. C., and Soga, K. (2012). "Stress-strain response of hydrate-bearing sands: numerical study using discrete element method simulations." *Journal of Geophysical Research*, 117, B04202.

Kalliadasis, S. and Chang, H. (1994). "Apparent dynamic contact angle of an advancing gas-liquid meniscus." *Physics of Fluids*, 6(1), 12-23.

Kampel, G., Goldsztein, G. H., and Santamarina, J. C. (2008). "Plugging of porous media and filters: Maximum clogged porosity." *Applied Physics Letters*, 92, 804101.

Kawasaki, M., Umezu, S., and Yasuda, M. (2006). "Pressure temperature core sampler (PTCS)." *Journal of the Japanese Association for Petroleum Technology*, 71(1), 139-147.

Kenney, T. C. (1967). "The influence of mineral composition on the residual strength of natural soils." *Proceedings of the Geotechnical Conference on Shear Strength Properties of Natural Soils and Rocks*, I, 123-129.

Kida, M., Suzuki, K., Kawamura, T., Oyama, H., Nagao, J., Ebinuma, T., and Narita, H. (2009). "Characteristics of natural gas hydrates occuring in pore-spaces of marine sediments collected from the eastern Nankai Trough, off Japan." *Energy Fuels*, 23, 5580-5586.

Kim, S. and Santamarina, J. C. (2014). "Engineered CO_2 injection: the use of surfactant for enhanced sweep efficiency." *International Journal of Greenhouse Gas Control*, 20, 324-332.

Knittel, K., Boetius, A., Lemke, A., Eilers, H., Lochte, K., Pfannkuche, O., and Linke, P. (2003). "Activity, distribution, and diversity of sulfate reducers and other bacteria in sediments above gas hydrate (Cascadia Margin, Oregon)." *Geomicrobiology Journal*, 20, 269-294.

Konrad, J. M. and Samson, M. (2000). "Hydraulic conductivity of kaolinite-silt mixtures subjected to closed-system freezing and thaw consolidation." *Canadian Geotechnical Journal*, 37, 857-869.

Konrad, J. M. and Duquennoi, C. (1993). "A model for water transport and ice lensing in freezing soils." *Water Resources Research*, 29(9), 3109-3124.

Konrad, J. M. and Morgenstern, N. R. (1980). "A mechanistic theory of ice lens formatin in fine-grained soils." *Canadian Geotechnical Journal*, 17, 473-486.

Kormas, K., Smith, D. C., Edgcomb, V., and Teske, A. (2003). "Molecular analysis of deep subsurface microbial communities in Nankai Trough sediments (ODP Leg 190, Sitg 1176)." *FEMS Microbiology Ecology*, 45, 115-125.

Koumoto, T. and Houlsby, G. T. (2001). "Theory and practice of the fall cone test." *Geotechnique*, 51(8), 701-712.

Kurihara, M., Sato, A., Funatsu, K., Ouchi, H., Yamamoto, K., Numasawa, M., Ebinuma, T., Narita, H., Masuda, Y., Dallimore, S. R., Wright, F., and Ashford, D. (2010). "Analysis of production data for 2007/2008 Mallik gas hydrate production tests in Canada." *The Society of Petroleum Engineering*, SPE 132155.

Kvenvolden, K. (1993). "Gas hydrates - geological perspective and global change." *Reviews of Geophysics*, 31(2), 173-187.

Kvenvolden, K. (1995). "A review of the geochemistry of methane in natural gas hydrate." *Organic Geochemistry*, 23(11), 997-1008.

Kvenvolden, K. A. (1988). "Methane hydrate - a major reservoir of carbon in the shallow geosphere?" *Chemical Geology*, 71, 41-51.

Kvenvolden, K. A., Barnard, L. A., and Cameron, D. H. (1983). "Pressure core barrel: application to the study of gas hydrate, Deep Sea Drilling Project Site 533, Leg 76." *Init. Repts. DSDP, 76*, Sheridan, R .E., Gradstein, F. M., et al., eds, Washington, D.C., 367-375.

Kwok, D. Y. and Neumann, A. W. (2000). "Contact angle interpretation in terms of solid surface tension." *Colloids and surfaces*, 161, 31-48.

Kyriakides, S. and Chang, Y.-C. (1990). "On the inflation of a long elastic tube in the presence of axial load." *International Journal of Solids and Structures*, 26, 975 - 991.

Kyriakides, S. and Chang, Y.-C. (1991). "The initiation and propagation of alocalized instability in an inflated elastic tube." *International Journal of Solids and Structures*, 27(9), 1085-1111.

Lambe, T. W. and Whitman, R. V. (1969). *Soil Mechanics*, John Wiley & Sons.

Lange, M. A. and Ahrens, T. J. (1983). "The dynamic tensile strength of ice and ice-silicate mixtures." *Journal of Geophysical Research: Soild Earth*, 88(B2), 1197-1208.

Lee, J. S. and Santamarina, J. C. (2005a). "Bender elements: Performance and signal interpretation." *Journal of Geotechnical and Geoenvironmental Engineering*, 131(9), 1063-1070.

Lee, J. S. and Santamarina, J. C. (2005b). "P-wave reflection imaging." *Geotechnical Testing Journal*, 28, 197-206.

Lee, J. Y., Santamarina, J. C., and Ruppel, C. (2010). "Volume change associated with formation and dissociation of hydrate in sediment." *Geochemistry Geophysics Geosystems*, 11(3), Q03007.

Lee, J. Y., Schultheiss, P. J., Druce, M., and Lee, J. (2009). "Pressure core sub sampling for GH production tests at *in situ* effective stress." *Fire in the Ice*, 9(4), 16-17.

Lee, J. Y., Yun, T. S., Santamarina, J. C., and Ruppel, C. (2007). "Observations related to tetrahydrofuran and methan hydrates for laboratory studies of hydrate-bearing sediments." *Geochemistry Geophysics Geosystems*, 8, Q06003.

Levitt, M. D. and Bond, J. H. (1980). "Flatulence." *Annual Review of Medicine*, 31, 127-137.

Li, L., Guenzennec, J., Nichols, P., Henry, P., Yanagibayashi, M., and Kato, C. (1999). "Microbial diversity in Nankai Trough sediments at a depth of 3,843 m." *Journal of Oceanography*, 55, 635-642.

Lindahl, V. and Bakken, L. R. (1995). "Evaluation of methods for extraction of bacteria from soil." *FEMS Microbiology Ecology*, 16, 135-142.

Liu, S., Cool, P., Collart, O., Van Der Voort, P., Vansant, E., Lebedev, O. I., Van Tendeloo, G., and Jiang, M. (2003). "The influence of the alcohol concentration on the structural ordering of mesoporous silica: cosurfactant versus cosolvent." *The Journal of Physical Chemistry B*, 107, 10405-10411.

Liu, X. Y. (2000). "Heterogeneous nucleation or homogeneous nucleation?" *Journal of Chemical Physics*, 112(22), 9949-9955.

Lupini, J. F., Skinner, A. E., and Vaughan, P. R. (1981). "The drained residual strength of cohesive soils." *Geotechnique*, 31(2), 181-213.

Madigan, M. T., Martinko, J. M., Dunlap, P. V., and Clark, D. P. (2009). *Brock Biology of Microorganisms*, Pearson Education, Inc.

Masui, A., Miyazaki, K., Haneda, H., Ogata, Y., and Aoki, K. (2008). "Mechanical properties of natural gas hydrate bearing sediments retrived from eastern Nankai Trough." *Offshore Technology Conference*, OTC19277.

Mayne, P. W. (2006). "In-situ test calibrations for evaluating soil parameter." *Characterisation and Engineering Properties of Natural Soils*, Phoon, K. K., Hight, D. W., Leroueil, S., and Tan, T. S., eds., Taylor & Francis.

Mesri, G. and Cepeda-Diaz, A. F. (1986). "Residual shear strength of clays and shales." *Geotechnique*, 36(2), 269-274.

Milkov, A. V. (2004). "Global estimates of hydrate-bound gas in marine sediments: how much is really out there?" *Earth-Science Reviews*, 66, 183-197.

Miller, R., Joos, P., and Fainerman, V. B. (1994). "Dynamic surface and interfacial tensions of surfactant and polymer solutions." *Advances in Colloid and Interface Science*, 49, 249-302.

Mills, H. J., Hodges, C., Wilson, K., MacDonald, I. R., and Sobecky, P. A. (2003). "Microbial diversity in sediments associated with surface-breaching gas hydrate mounds in the Golf of Mexico." *FEMS Microbiology Ecology*, 46, 39-52.

Mills, H. J., Reese, B. K., Shepard, A. K., Riedinger, N., Dowd, S. E., Morono, Y., and Inagaki, F. (2012). "Characterization of metabolically active bacterial populations in subseafloor Nankai Trough sediments above, within, and below the sulfate-methane transition zone." *Frontiers in Microbiology*, 3, 1-12.

Mitchell, J. K. and Santamarina, J. C. (2005). "Biological considerations in geotechnical engineering." *Journal of Geotechnical and Geoenvironmental Engineering*, 131(10), 1222-1233.

Mitchell, J. K. and Soga, K. (2005). *Fundamentals of Soil Behavior*, John Wiley & Sons, Inc.

Miwa, M., Nakjima, A., Fujishima, A., Hashimoto, K., and Watanabe, T. (2000). "Effects of the surface roughness on sliding angles of water droplets on superhydrophobic surfaces." *Langmuir*, 16, 5754-5760.

Morgenstern, N. R. and Nixon, J. F. (1971). "One-dimensional consoidation of thawing soils." *Canadian Geotechnical Journal*, 8, 558-565.

Morgenstern, N. R. and Smith, L. B. (1973). "Thaw-consolidation tests on remould clays." *Canadian Geotechnical Journal*, 10(1), 25-40.

Moridis, G. J. and Collett, T. S. (2003). "Strategies for gas production from hydrate accumulations under various geological and reservoir conditions." *Proceedings, TOUGH Symposium*, 1-8.

Moridis, G. J., Collett, T. S., Pooladi-Darvish, M., Hancock, S., Santamarina, C., Kowalsky, M. B., Reagan, M. T., Sloan, E. D., Sum, A. K., and Koh, C. A. (2011). "Challenges, uncertainties, and issues facing gas productin from gas-hydrate deposits." *SPE Reservoir Evaluation and Engineering*, SPE 131792, 76-112.

Moridis, G. J. and Sloan, E. D. (2007). "Gas production potential of disperse low-saturation hydrate accumulations in oceanic sediments." *Energy Conversion and Management*, 48, 1834-1849.

Morrow, N. R. (1970). "Physics and thermodynamics of capillary." *Industrial and Engineering Chemistry*, 62(6), 32-56.

Nakamura, K., Enomoto, A., Fukushma, H., Nagai, K., and Hakoda, M. (1994). "Distruption of microbial cells by the flash discharge of high-pressure carbon dioxide." *Bioscience, Biotechnology and Biochemistry*, 58(7), 1297-1301.

Nesse, W. D. (2000). *Introduction to Mineralogy*, Oxford University Press.

Newberry, C. J., Webster, G., Cragg, B. A., Parkes, R. J., Weightman, A. J., and Fry, J. C. (2004). "Diversity of prokaryotes and methanogenesis in deep subsurface sediments from the Nankai Trough, Ocean Drilling Program Leg 190." *Environmental Microbiology*, 6(3), 274-284.

Nickling, W. G. and Bennett, L. (1984). "The shear strength characteristics of frozen coarse granular debris." *Journal of Glaciology*, 30(106), 384-357.

Nixon, J. F. (1991). "Thaw-subsidence effects on offshore pipelines." *Journal of Cold Regions Engineering*, 5(1), 28-39.

Nixon, J. F. and Ladanyi, B. L. (1978). "Thaw consolidation." *Geotechnical Engineering for Cold Regions*, Andersland, O. B. and Anderson, D. M., eds., McGraw-Hill Book Company.

Nixon, M. F. and Grozic, J. L. H. (2007). "Submarine slope failure due to gas hydrate dissociation: a preliminary quantification." *Canadian Geotechnical Journal*, 44, 314-325.

Nunoura, T., Inagaki, F., Delwiche, M. E., Colwell, F. S., and Takai, K. (2008). "Subseafloor microbial communities in methane hydrate-beaing sediment at two distinct locations (ODP Leg204) in the Cascadia Margin." *Microbes and Environments*, 23(4), 317-325.

Oda, M. (1972). "Deformation mechanism of sand in triaxial compression tests." *Soils and Foundations*, 12(4), 45-63.

Olivella, S. and Alonso, E. E. (2008). "Gas flow through clay barriers." *Geotechnique*, 58(3), 157-176.

Palomino, A. M. and Santamarina, J. C. (2005). "Fabric map for kaolinite: Effects of pH and ionic concentration on behavior." *Clays and Clay Minerals*, 53(3), 209-222.

Parkes, R. J., Cragg, B. A., and Wellsbury, P. (2000). "Recent studies on bacterial poplations and processes in subseafloor sediments: A review." *Hydrogeology Journal*, 8, 11-28.

Parkes, R. J., Sellek, G., Webster, G., Martin, D., Anders, E., Weightman, A. J., and Sass, H. (2009). "Culturable prokaryotic diversity of deep, gas hydrate sediments: first use of a contiunous high-pressure, anaerobic, enrichment and isolation system for subseafloor sediments (DeepIsoBUG)." *Environmental Microbiology*, 11(12), 3140-3153.

Patterson, M. F. (2005). "Microbiology of pressure-treated foods." *Journal of Applied Microbiology*, 98, 1400-1409.

Pattle, R. E. (1955). "Properties, function and origin of the alveolar lining layer." *Nature*, 175, 1125-1127.

Penner, E. (1986). "Aspects of ice lens growth in soils." *Cold Regions Science and Technology*, 13, 91-100.

Pettigrew, T. L. (1992). "The design and operation of a wireline pressure core sampler (PCS)." *ODP Technical Note*, 17.

Phadnis, H. S. and Santamarina, J. C. (2011). "Bacteria in sediments: pore size effects." *Geotechnique Letters*, 1, 91-93.

Polidori, E. (2003). "Proposal for a new plasticity chart." *Geotechnique*, 53(4), 397-406.

Qin, H., Gu, L., Zhu, L., and Chen, Y. (2005). "Pressure tight piston corer - A new approach on gas hydrate investigation." *China Ocean Engineering*, 19(1), 121-128.

Raimbourg, H., Hamano, Y., Saito, S., Kinoshita, M., and Kopf, A. (2011). "Acoustic and mechanical properties of Nankai accretionary prism core samples." *Geochemistry Geophysics Geosystems*, 12, Q0AD10.

Rebata-Landa, V. and Santamarina, J. C. (2006). "Mechanical limits to microbial activity in deep sediments." *Geochemistry Geophysics Geosystems*, 7, Q11006.

Reeburgh, W. S. (2007). "Oceanic methane biogeochemistry." *Chemical Reviews*, 107(2), 486-513.

Reed, D. W., Fujita, Y., Delwiche, M. E., Blackwelder, B., Sheridan, P. P., Uchida, T., and Cowell, F. S. (2002). "Microbial communities from methane hydrate-bearing deep marine sediments in a Forearc Basin." *Applied and Environmental Microbiolgy*, 68(8), 3759-3770.

Rempel, A. W. (2007). "Formation of ice lenses and frost heave." *Journal of Geophysical Research*, 112, F02S21.

Riis, V., Lorbeer, H., and Babel, W. (1998). "Extraction of microorganisms from soil: evaluation of the efficiency by counting methods and activity measurements." *Soil Biology & Biochemistry*, 30(12), 1573-1581.

Rose, W. R. and Heins, R. W. (1962). "Moving interfaces and contact angle rate-dependency." *Journal of Colloid Science*, 17, 39-48.

Rosen, M. J. (2004). *Surfactants and Interfacial Phenomena*, John Wiley & Sons, Inc.

Rosenbaum, E. J., English, N. J., Johnson, J. K., Shaw, D. W., and Warzinski, R. P. (2007). "Thermal conductivity of methane hydrate from experiment and molecular simulation." *Journal of Physical Chemistry B*, 111(46), 13194-13205.

Rutqvist, J. and Moridis, G. J. (2007). "Numerical studies of geomechanical stability of hydrate-bearing sediments." *Offshore Technology Conference*, OTC 18860.

Rutqvist, J., Moridis, G. J., Grover, T., and Collett, T. (2009). "Geomechanical response of permafrost-associated hydrate deposits to depressurization-induced gas production." *Journal of Petroleum Science and Engineering*, 67, 1-12.

Sakamoto, C., Yamaguchi, N., and Nasu, M. (2005). "Rapid and simple quantification of bacterial cells by using a microfluidic device." *Applied and Environmental Microbiolgy*, 71(2), 1117-1121.

Santamarina, J. C., Dai, S., Jang, J., and Terzariol, M. (2012). "Pressure core characterization tools for hydrate-bearing sediments." *Scientific Drilling Journal*, 14, 44-48.

Santamarina, J. C., Klein, K. A., and Fam, M. A. (2001). *Soils and Waves*, John Wiley & Sons, LTD.

Santamarina, J. C., Klein, K. A., Palomino, A., and Guimaraes, M. S. (2002). "Micro-scale aspects of chemical-mechanical coupling - interparticle forces and fabric." *Maratea, Balkema, Rotterdam*, 47-64.

Santamarina, J. C., Klein, K. A., Wang, Y. H., and Prencke, E. (2002). "Specifice surface: determination and relevance." *Canadian Geotechnical Journal*, 39, 233-241.

Santamarina, J. C. and Shin, H. (2010). "Frictional phenomena in granular media." *Meso-Scale Shear Physics in Earthquake and Landslide Mechanics*, Hatzor, Y. H., Sulem, J., and Vardoulakis, I., eds., CRC Press, 159-190.

Sassen, R., Joye, S., Sweet, S. T., DeFreitas, D. A., Milkov, A. V., and MacDonald, I. R. (1999). "Thermogenic gas hydrates and hydrocarbon gases in complex chemosysntheic communities, Gulf of Mexico continental slope." *Organic Geochemistry*, 30, 485-497.

Schauf, C. L., Moffett, D. F., and Moffett, S. B. (1990). *Human Physiology: Foundations and Frontiers*, Times Mirror/Mosby College Publishing, St. Louis.

Schippers, A., Neretin, L. N., Kallmeyer, J., Ferdelman, T. G., Cragg, B. A., Parkes, R. J., and Jorgensen, B. B. (2005). "Prokaryotic cells of the deep sub-seafloor biosphere identified as living bacteria." *Nature*, 433, 861-864.

Schultheiss, P. J., Francis, T. J. G., Holland, M., J.A., R., Amann, H., Thjunjoto, and Parke, R. J. (2006). "Pressure coring, logging and subsampling with the HYCINTH system." *New Techniques in Sediment Core Analysis*, Rothwell, G., ed., Geol. Soc. London, Spec. Pub., 151-163.

Schultheiss, P. J., Holland, M., and Humphrey, G. (2009). "Wireline coring and analysis under pressure: Rescent use and future developments of the HYACINTH system." *Scientific Drilling Journal*, 7, 44-50.

Schulz, J. C. and Warr, G. G. (2002). "Adsorbed layer structure of cationic and anionic surfactants on mineral oxide surfaces." *Langmuir*, 18, 3191-3197.

Schurch, S., Gerke, J., and Clements, J. A. (1976). "Direct determination of surface tension in the lung." *Proceedings of the National Academy of Science of the United States of America*, 73(12), 4698-4702.

Schurch, S., Lee, M., and Gehr, P. (1992). "Pulmonary surfactant: Surface properties and function of alveolar and airway surfactant." *Pure and Applied Chemistry*, 64(11), 1745-1750.

Seed, H. B., Woodward, R. J., and Lundgren, R. (1964). "Clay mineralogical aspects of the Atterberg limits." *Journal of the Soil Mechanics and foundations Division*, 90(SM4), 107-131.

Serra, J., Azpiroz, F., and Malagelada, J. R. (1998). "Intestinal gas dynamics and tolerance in humans." *Gastroenterology*, 115, 542-550.

Sharma, R. and Ross, D. S. (1991). "Kinetics of liquid penetration into periodically constricted capillaries." *Journal of the Chemical Society, Farady Transactions*, 87(4), 619-624.

Sherman, I. W. and Sherman, V. G. (1979). *Biology: A human approach*, Oxford University Press, New York.

Sherwood, P. T. and Ryley, M. D. (1970). "An investigation of a cone-penetrometer method for the determination of the liquid limit." *Geotechnique*, 20(2), 203-208.

Shin, H. and Santamarina, J. C. (2010). "Fluid-driven fractures in uncemented sediments: Underlying particle-level processes." *Earth and Planetary Science Letters*, 299, 180-189.

Siebold, A., Nardin, M., Schultz, J., Walliser, A., and Oppliger, M. (2000). "Effect of dynamic contact angle on capillary rise phenomena." *Colloids and surfaces*, 161, 81-87.

Skempton, A. W. and Northey, R. D. (1953). "The sensitivity of clays." *Geotechnique*, 3(1), 30-53.

Sloan, E. D. and Koh, C. A. (2008). *Clathrate Hydrates of Natural Gases*, CRC Press, Taylor & Francis Group, LLC.

Smith, D. C., Spivack, A. J., Fisk, M. R., Haveman, S. A., and Staudigel, H. (2000a). "Tracer-based estimates of drilling-induced microbial contamination of deep sea crust." *Geomicrobiology Journal*, 17(3), 207-219.

Smith, D. C., Spivack, A. J., Fisk, M. R., Haveman, S. A., Staudigel, H., and party, L. s. s. (2000b). "Methods for quantifying potential microbial contamination during deep ocean coring." *ODP Technical Note*, 28.

Spagnoli, G., Stanjek, H., and Sridharan, A. (2012). "Influence of ethanol/water mixture on the undrained shear strength of pure clays." *Bulletin of Engineering Geology and the Environment*, 71, 389-398.

Sridharan, A. and Nagaraj, H. B. (1999). "Absorption water content and liquid limit of soils." *Geotechnical Testing Journal*, 22(2), 121-127.

Sridharan, A. and Nagaraj, H. B. (2000). "Compressibility behaviour of remoulded, fine-grained soils and correlation with index properties." *Canadian Geotechnical Journal*, 37, 712-722.

Sridharan, A. and Nagaraj, H. B. (2004). "Coefficient of consolidation and its correlation with index properties of remolded soils." *Geotechnical Testing Journal*, 27(5), GTJ10784.

Stephen, A. M. and Cummings, J. H. (1980). "The microbial contribution to human faecal." *Journal of Medical Microbiology*, 13, 45 - 56.

Sultan, N., Cochonat, P., Foucher, J. P., and Mienert, J. (2004). "Effect of gas hydrates melting on seafloor slope instability." *Marine Geology*, 213, 379-401.

Taber, S. (1929). "Frost heaving." *The Journal of Geology*, 37(5), 428-461.

Tanaka, M., Tanaka, H., Kamei, T., and Hayashi, S. (2003). "Effects of diatom microfossil contents on engineering properties of soils." *Proceedings of the Thirteenth (2003) International Offshore and Polar Engineering Conference, Honolulu, Hawaii, USA*, 372-377.

Tanner, L. H. (1979). "The spreading of silicone oil drops on horizontal surfaces." *Journal of Physics D: Applied Physics*, 12, 1479-1484.

Thomson, W. (1886). "Capillary attraction." *Nature*, 34, 270-272.

Tishchenko, P., Hensen, C., Wallmann, K., and Wong, C. S. (2005). "Calculation of the stability and solubility of methane hydrate in seawater." *Chemical Geology*, 219, 37-52.

Tortora, G. J. and Grabowski, S. R. (2000). *Principles of anatomay and physiology*, John Wiley & Sons, Inc.

Tremolaterra, F., Villoria, A., Serra, J., Azpiroz, F., and Malagelada, J. R. (2006). "Intestinal tone and gas motion." *Neurogastroenterology & Motility*, 18, 905-910.

Uchida, S., Soga, K., J-Kvalstad, T., and Yamamoto, K. (2011). "Geomechanical impact of soil layering in hydrate bearing sediments during gas production." *Proceedings of the 7th International Conference on Gas Hydrate (ICGH)*, Edinburgh, Scotland, United Kingdom, July.

Uchida, T., Waseda, A., and Namikawa, T. (2009). "Methane accumulation and high concentration of gas hydrate in marine and terrestrial sandy sediments." *Natural Gas Hydrates - Energy Resource Potential and Associated Geologic Hazard*, Collett, T., Johnson, A., Knapp, C., and Boswell, R., eds., AAPG Memoir, 401-413.

Valdes, J. R. and Santamarina, J. C. (2008). "Clogging: bridge formation and vibration-based destabilization." *Canidian Geotechnical Journal*, 45, 177-184.

Veldhuizen, R., Nag, K., Orgeig, S., and Possmayer, F. (1998). "The role of lipids in pulmonary surfactant." *Biochimica et Biophysica Acta*, 1408, 90-108.

Waite, W. F., Santamarina, J. C., Cortes, D. D., Espinoza, D. N., Germaine, J., Jang, J., Jung, J. W., Kneafsey, T. J., Shin, H., Soga, K., Winters, W. J., and Yun, T. S. (2009). "Physical properties of hydrate-bearing sediments." *Reviews of Geophysics*, 47, RG4003.

Waite, W. F., Stern, L. A., Kirby, S. H., Winters, W. J., and Mason, D. H. (2007). "Simultaneous determination of thermal conductivity, thermal diffusivity and specific heat in sI methane hydrate." *Geophysical Journal International*, 169, 767-774.

Waite, W. F., Winters, W. J., and Mason, D. H. (2004). "Methan hydrate formation in partially water-saturated Ottawa sand." *American Mineralogist*, 89, 1202-1207.

Warkentin, B. P. (1972). "Use of liquid limit in characterizaing clay soils." *Canadian Journal of Soil Science*, 52, 457-464.

Wasti, Y. and Bezirci, M. H. (1986). "Determination of the consistency limits of soils by the fall cone test." *Canadian Geotechnical Journal*, 23, 241-246.

Watson, G. H., Rowley, R. K., and Slusarchuk, W. A. (1973). "Performance of a warm-oil pipeline buried in permafrost." *Permafrost: The North American Contribution to the Second Internaltional Conference*, 759-766.

Weast, R. C. (1987). *CRC Handbook of Chemistry and Physics*, CRC Press.

Webster, G., Parkes, R. J., Cragg, B. A., Newberry, C. J., Weightman, A. J., and Fry, J. C. (2006). "Prokaryotic community composition and biogeochemical processes in deep subseafloor sediments from the Peru Margin." *FEMS Microbiology Ecology*, 58, 65-85.

Wetzel, A. (1990). "Interrelationship between porosity and other geotechnical properties of slowly deposited, fine-grained marine surface sediments." *Marine Geology*, 92, 105-113.

White, W. A. (1949). "Atterberg plastic limits of clay minerals." *American Mineralogist*, 34, 508-512.

Wintermayer, A. M. (1926). "Adaptation of Atterberg plasticity tests for subgrade soils." *Public Roads*, 7(6), 119-122.

Winters, W., Walker, M., Hunter, R., Collett, T., Boswell, R., Rose, K., Waite, W., Torres, M., Patil, S., and Dandekar, A. (2011). "Physical properties of sediment from the Mount Elbert gas hydrate stratigraphic test well, Alask North Slope." *Marine and Petroleum Geology*, 28, 361-380.

Wood, D. M. (1982). "Cone penetrometer and liquid limit." *Geotechnique*, 32(2), 152-157.

Xu, W. and Ruppel, C. (1999). "Predicting the occurrence, distribution, and evolution of methane gas hydrate in porous marine sediments." *Journal of Geophysical Research*, 104(B3), 5081-5095.

Yamamoto, K. (2013). "Japan completes first offshore methane hydrate production test - methane successfully produced from deepwater hydrate layers." *Fire in the Ice*, 13(2), 1-2.

Yamamoto, K., Inada, N., Kubo, S., Fujii, T., Suzuki, K., and Konno, Y. (2012). "Pressure core sampling the eastern Nankai Trough." *Fire in the Ice*, 12(2), 1-6.

Youd, T. (1973). "Factors controlling maximum and minimum density on relative density." *Evaluation of relative density and its role in geotechnical projects involving cohesionless soils*, Seling, E. T. and Ladd, R. S., eds., ASTM STP523, 98-112.

Young, T. (1804). "An essay on the cohesion of fluids." *Philosophical Transactions of the Royal Society of London*, 95, 65-87.

Yun, T. S., Fratta, D., and Santamarina, J. C. (2010). "Hydrate-bearing sediments from the Krishna-Godavari basin: Physical characterization, pressure core testing, and scaled production monitoring." *Energy Fuels*, 24, 5972-5983.

Yun, T. S., Lee, C., Lee, J. S., Bahk, J. J., and Santamarina, J. C. (2011). "A pressure core based characterization of hydrate-bearing sediments in the Ulleung Basin, Sea of Japan (East Sea)." *Journal of Geophysical Research*, 116, B02204.

Yun, T. S., Narsilio, G. A., Santamarina, J. C., and Ruppel, C. (2006). "Instrumented pressure testing chamber for characterizing sediment cores recovered at in situ hydrostatic pressure." *Marine Geology*, 229, 285-293.

Yun, T. S., Santamarina, J. C., and Ruppel, C. (2007). "Mechanical properties of sand, silt, and clay containing tetrahydrofuran hydrate." *Journal of Geophysical Research*, 112, B04106.

Zhang, R. and Somasundaran, P. (2006). "Advances in adsorption of surfactants and their mixtures at solid/solution interfaces." *Advances in Colloid and Interface Science*, 123-126, 213-229.

VITA

JUNBONG JANG

Junbong Jang was born in Danyang, South Korea. He received both a bachelor's degree and a master's degree in Civil and Environmental Engineering from the Sungkyunkwan University, Seoul, South Korea in 2005 and 2007, respectively. He began his doctoral study in Civil and Environmental Engineering (Geosystems Engineering) at the Georgia Institute of Technology on August 2008. He will earn his Ph.D. degree in 2014.